ANALYSIS OF THE CHARMED SEMILEPTONIC DECAY $D^+ \to \rho^0 \mu^+ \nu$

By

Eduardo E. Luiggi

Dissertation

Submitted to the Faculty of the

Graduate School of Vanderbilt University

in partial fulfillment of the requirements

for the degree of

DOCTOR OF PHILOSOPHY

in

Physics

December 2008

Nashville, Tennessee

Approved:

Will E. Johns

Franz Baudenbacher

Thomas Kephart

Paul D. Sheldon

Thomas Weiler

To Carol and Eduardo André

ACKNOWLEDGEMENTS

TABLE OF CONTENTS

LIST OF FIGURES

CHAPTER I

INTRODUCTION

The search for the fundamental constituents of matter has been pursued and studied since the dawn of civilization. As early as the fourth century BCE, Democritus, expanding the teachings of Leucippus, proposed small, indivisible entities called atoms, interacting with each other to form the Universe. Democritus was convinced of this by observing the environment around him. He observed, for example, how a collection of tiny grains of sand can make out smooth beaches. Today, following the lead set by Democritus more than 2500 years ago, at the heart of particle physics is the hypothesis that everything we can observe in the Universe is made of a small number of fundamental particles interacting with each other. In contrast to Democritus, for the last hundred years we have been able to perform experiments that probe deeper and deeper into matter in the search for the fundamental particles of nature.

Today's knowledge is encapsulated in the Standard Model of particle physics, a model describing the fundamental particles and their interactions. It is within this model that the work in this thesis is presented. This work attempts to add to the understanding of the Standard Model by measuring the relative branching fraction of the charmed semileptonic decay $D^+ \to \rho^0 \mu^+ \nu$ with respect to $D^+ \to \overline{K}^{*0} \mu^+ \nu$. Many theoretical models that describe hadronic interactions predict the value of this relative branching fraction, but only a handful of experiments have been able to measure it with any precision. By making a precise measurement of this relative branching fraction theorists can distinguish between viable models as well as refine existing ones.

In this chapter, a general introduction to the Standard Model is given. Along with it, an introduction to heavy quark physics with emphasis on the charm sector and semileptonic processes will be presented.

I.1 The Standard Model

The Standard Model (SM) of particle physics is a very successful phenomenological model that describes the elementary particles of matter and their interactions. By elementary we mean particles that are structureless and indivisible (at least at the scale of 10^{-16} cm). In the Standard Model fundamental particles are classified in two groups: matter particles called *fermions* and the force carriers called *bosons*. The model includes three of the four fundamental forces in nature. These forces are:

- The Electromagnetic Force

- The Weak Nuclear Force

- The Strong Nuclear Force

There is a great deal of effort to extend the Standard Model by incorporating the gravitational force into it, but so far, these efforts have been unsuccessful. Fortunately, the mass scales involved in particle physics are so small that gravity has a negligible effect on particle reactions seen in the laboratory.

I.1.1 Fermions

Particles with half integer spin obey Fermi–Dirac statistics and are called *fermions*. The electron and the quarks arranged in the familiar protons and neutrons, the building blocks of matter, are examples of charged fermions. Fundamental fermions have spin of 1/2 and can be classified as *leptons* and *quarks*. There are three charged leptons in nature, the electron, the muon, and the tau. Three neutrinos, one of each flavor, correspond to each charged lepton. Neutrinos have zero charge and because of the non-observation of right handed neutrinos, they are assumed to be massless within the Standard Model. The recent discovery of neutrino oscillations has shown that neutrinos do have a small but non-zero mass providing a small but important departure from the predictions made by the Standard Model.

The leptons are organized in three generations, each charged lepton with its corresponding neutrino.

$$\begin{pmatrix} e \\ \nu_e \end{pmatrix}, \quad \begin{pmatrix} \mu \\ \nu_\mu \end{pmatrix}, \quad \begin{pmatrix} \tau \\ \nu_\tau \end{pmatrix} \tag{I.1}$$

The masses of the charged leptons increase as we move from the electron generation to the tau generation. One member of a generation can be transformed to the other member of the same generation via the weak interaction. Leptons do not feel the strong force.

Quarks carry fractional charge of $+2/3|e|$ (up-type quark) and $-1/3|e|$ (down-type quark). There are three up-type quarks (up, charm, top) and three down-type quarks (down, strange, bottom) arranged in three generations according to their masses. Each generation has an up-type quark and a down-type quark.

$$\begin{pmatrix} u \\ d \end{pmatrix}, \quad \begin{pmatrix} c \\ s \end{pmatrix}, \quad \begin{pmatrix} t \\ b \end{pmatrix} \tag{I.2}$$

Currently we do not know why there are three generations of quarks and leptons or why the masses differ so much from generation to generation. The values for the fermion masses are input parameters of the SM that are determined experimentally.

The weak interaction can transform one quark into another but, whereas the leptons can only be transformed to the other member of the generation, quarks can cross between generations as long as this is energetically possible and the reaction has $|\Delta Q| = 1$.

Some of the properties of the fermions are summarized in Table I.1 and Table I.2. Each fermion has its own anti-particle which has the same mass as the particle but with opposite quantum numbers, such as the charge.

Quarks bind together to form *hadrons*. Hadrons can be classified as *mesons*, bound states of a quark and an anti-quark ($q\overline{q}$), and *baryons*, bound states of three quarks (qqq) or three anti-quarks ($\overline{qqq}$).

Quarks not only carry electrical charge, but they also carry *color* charge. The color

charge can be either *red*, *green* or *blue*. Only *colorless* combinations of baryons and mesons are allowed. This new degree of freedom was first introduced in order to account for the Δ^{++} (uuu) baryon, a bound state with three quarks in the same state. Baryons, as spin 1/2 particles, obey Pauli's exclusion principle: two identical particles cannot be in the same state with the same quantum numbers. This contradiction is resolved if a new quantum number, color, is introduced. The seemingly arbitrary addition of a new quantum number is validated by the measurement of the ratio

$$R = \frac{\sigma(e^+e^- \to \text{Hadrons})}{\sigma(e^+e^- \to \mu^+\mu^-)}.$$

This ratio depends on the sum of the squares of the quark electric charges, $\sum_i (e_i)^2$, where e_i is $2/3e$ for up-type quarks and $-1/3e$ for down-type quarks. For a model with five quarks and no color charge the ratio is

$$R = (2/3)^2 + (-1/3)^2 + (2/3)^2 + (-1/3)^2 + (-1/3)^2 = 11/9.$$

This prediction is off by about a factor of three as shown in Figure I.1 suggesting that each quark comes in three different kinds that we call colors.

Table I.1: Summary of the charged lepton properties [1].

Lepton	Charge $|e|$	Mass (MeV)
e	-1	0.511
μ	-1	105.658
τ	-1	1776.99

A very important property of the quarks is that they have never been found in isolation. This property, known as confinement, is responsible for the fact that quarks only exist in bound states such as mesons and baryons. Because quarks interact with the gluons that keep the hadrons together, determination of the individual masses of the quarks is not trivial. The
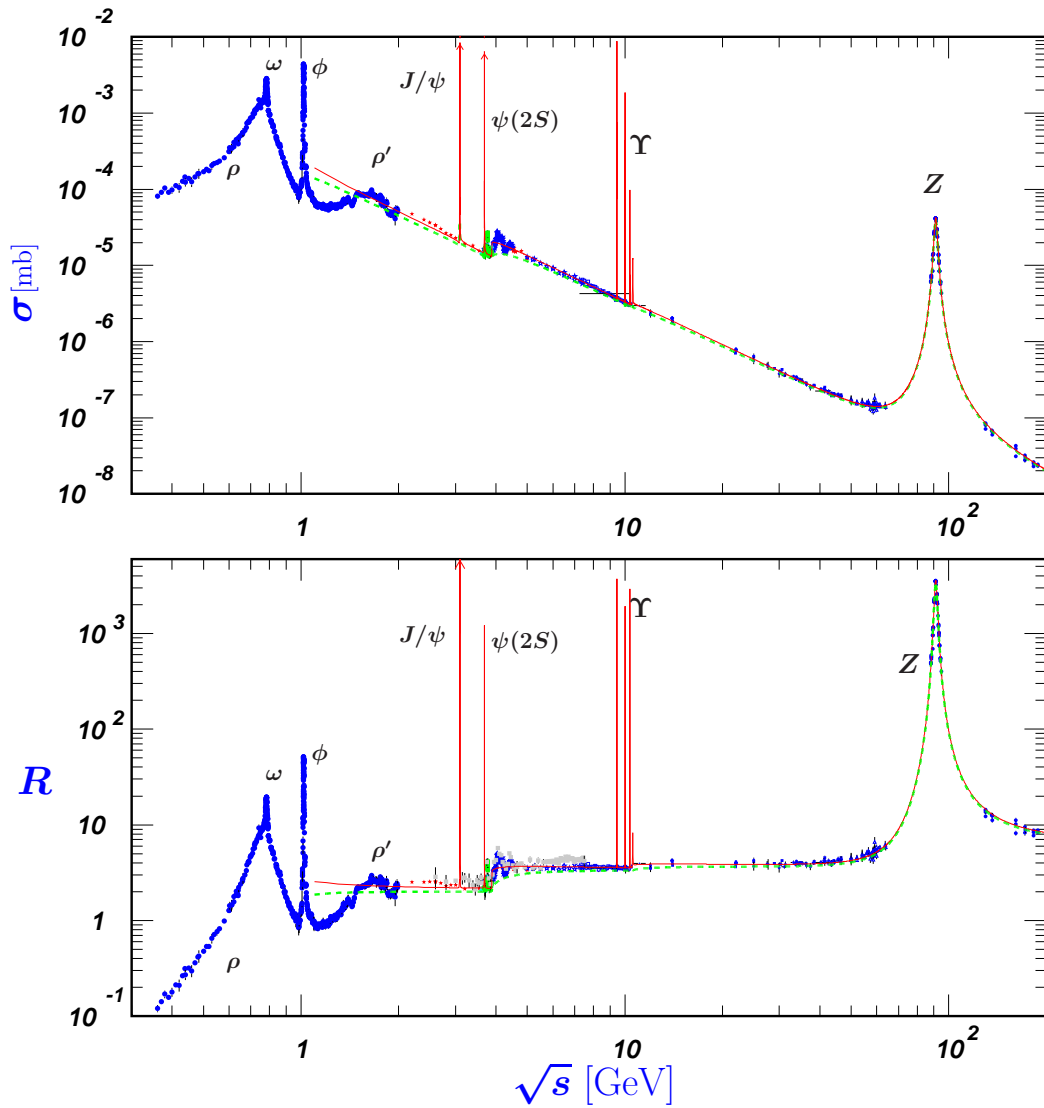
Figure I.1: World data on the cross section of $e^+e^- \rightarrow$ Hadrons (top) and the ratio $R = \frac{\sigma(e^+e^- \rightarrow \text{Hadrons})}{\sigma(e^+e^- \rightarrow \mu^+\mu^-)}$ up to the Z^0 mass (bottom). This ratio is predicted to be 11/9 for a model with 5 quarks with no color charge. The value from the experimental data is about a factor of 3 higher than predicted. This is evidence for the color charge of the quarks. Reprinted from [1] with permission from Elsevier.

Table I.2: Summary of quark properties [1].

Quark	Charge $|e|$	Mass
up (u)	+2/3	$2.55^{+0.75}_{-1.05}$ MeV
down (d)	-1/3	$5.04^{+0.96}_{-1.54}$ MeV
charm (c)	+2/3	$1.27^{+0.07}_{-0.11}$ GeV
strange (s)	-1/3	104^{+26}_{-34} MeV
top (t)	+2/3	171.2 ± 2.1 GeV
bottom (b)	-1/3	$4.2^{+0.17}_{-0.07}$ GeV

gluons contribute a sizable fraction of the energy of the system and therefore also contribute to the total mass of the system.

I.1.2 **Bosons**

Particles with integer spin obey Bose–Einstein statistics and are called *bosons*. The SM describes the interaction between particles (i.e., forces) as an exchange of gauge bosons between such particles. The range of the interaction and the characteristic lifetime for a given interaction is determined by the mass of the gauge boson mediating the interaction and the strength of the interaction, respectively. In the case of the interaction range, the more massive the gauge boson, the shorter its interaction range. For the case of the lifetime, stronger coupling constants mean decays occur more rapidly than for weaker coupling constants.

As mentioned before, gravity is not part of the SM and its corresponding boson, the graviton, has never been observed. Some properties of the SM gauge bosons are summarized in Table I.3.

The *strong* force, mediated by eight massless bosons called *gluons*, is responsible for keeping the quarks in bound states forming baryons and mesons. The gluons carry color-anti-color charge (e.g., red-anti-green) leading to the possibility of quarks changing color by absorbing or emitting gluons. Since the gluons are colored objects, they can interact among themselves forming triple and quartic gluon vertexes. Colored gluons leads to the

Table I.3: Summary of the SM forces and their intermediaries. The relative strength of the forces is measured as the force experienced by two up quarks at a distance of $10^{-18}m$ relative to the electromagnetic force. The graviton, which is yet to be observed, is included for completeness.

Force	Boson	Spin/parity	Relative Strength	Mass (GeV)
Strong	gluon (g)	1^-	25	~ 0
Electromagnetic	photon (γ)	1^-	1	~ 0
Weak	$W^\pm$, Z^0	1^-	0.8	80.42, 91.19
Gravity	graviton	2^+	10^{-41}	~ 0

possibility of forming exotic bound states called glueballs which consist only of gluons[1]. The fundamental QCD vertices describing a quark changing its color by emitting a colored gluon, and the gluon bound states are shown in Figure I.2 and Figure I.3, respectively.
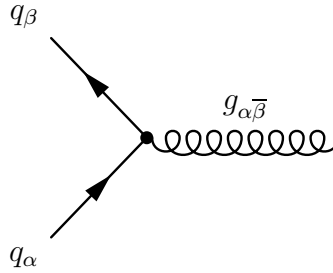
Figure I.2: Fundamental QCD vertex. A quark with color charge α radiates a gluon with color charge $\alpha\bar{\beta}$ resulting in a quark with new color charge β.

A commonly used phenomenological potential describing the interaction between quarks can be written as [5]

$$\mathbf{V_s} = -\frac{4}{3}\frac{\alpha_s(\mathbf{r})}{\mathbf{r}} + \mathbf{Kr}. \tag{I.3}$$

The different behaviors of the strong interaction can be seen in (I.3). At close range, the potential is dominated by the first term where the coupling constant, α_s, becomes smaller at high energy (i.e., short range) leading to asymptotic freedom of the quarks. Asymptotic freedom allows us to treat the quarks inside the hadrons as if they were quasi-free particles,

---

[1]Although some gluon candidates have been identified (see for example [2–4]) there is no solid evidence of their observation yet.
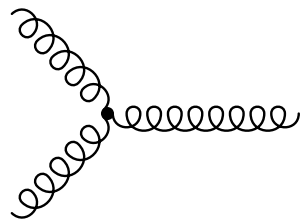
(a) Trilinear Gluon Vertex   (b) Quartic Gluon Vertex
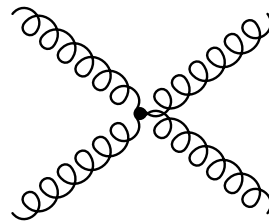
Figure I.3: Trilinear and quartic gluon vertices. The colored nature of the gluons allows the formation of gluon bound states, known as glueballs.

barely interacting between themselves. The second term dominates at large distances and is responsible for the confinement effect. This term can be seen as describing the force between quarks as we try to increase the distance between them. Since the energy needed to separate the bound state is greater than the energy needed to produce a $q\overline{q}$ pair from the vacuum, separation leads to the production of new hadrons, mostly in the form of light mesons like the pion. It is for this reason that free quarks have never been observed in nature.

At the nuclear scale, the strong force counteracts the electromagnetic repulsion among protons to keep atomic nuclei stable. This can be seen as the consequence of a residual strong interaction between the the quarks inside each nucleon. Spontaneous fission occurs when this balancing act can no longer be sustained.

Complications in the study of the strong interaction arise because the strength of the strong coupling constant is large enough that perturbation theory is no longer easily applicable. The strength of α_s makes the characteristic lifetime for a strong decay of the order of 10^{-23} sec.

The *electromagnetic* force is responsible for keeping the electrons and protons in atoms bound and along with the gravitational force dominates our everyday lives. It is mediated

by the massless photon making the range of the interaction infinite. The fundamental electromagnetic vertex, shown in Figure I.4, describes the interaction between to oppositely charged particles. Since the photon carries no electric charge, interactions between photons are not allowed at the tree level. The strength of the electromagnetic coupling constant, α is $\sim 1/137$. The characteristic lifetimes for electromagnetic decays are of the order of 10^{-21} sec.
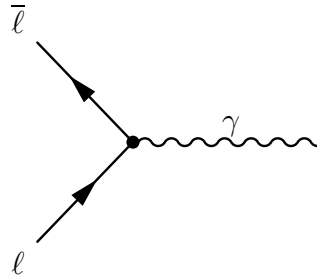
Figure I.4: Fundamental electromagnetic vertex.

The *weak* force is mediated by the massive $W^{\pm}$ and Z^0. The $W^{\pm}$ is responsible for the decay of quarks within and across generations (flavor changing), and decays of leptons within the same generation. The Z^0 contributes to the scattering between like–charge fermions (e.g., e^+e^-). Since the mass of the gauge boson is so heavy, the weak interaction has a range of about 10^{-16} cm. The typical lifetime for a weak decay is of the order of 10^{-10} sec. The fundamental vertex for the weak interactions of fermions is shown in Figure I.5. Like the strong interaction, the weak interaction allows the interaction between the gauge bosons.

The first known weak interaction was nuclear β-decay. In this process a neutron, composed of one down quark and two up quarks (udd) decays into a proton (uud), electron, and an electron neutrino.

$$\mathbf{n} \rightarrow \mathbf{p} + \mathbf{e}^- + \overline{\nu}_{\mathbf{e}} \qquad (I.4)$$

(a) $\ell\nu_\ell W$

(b) $Qq'W$

(c) $f\bar{f}Z^0$
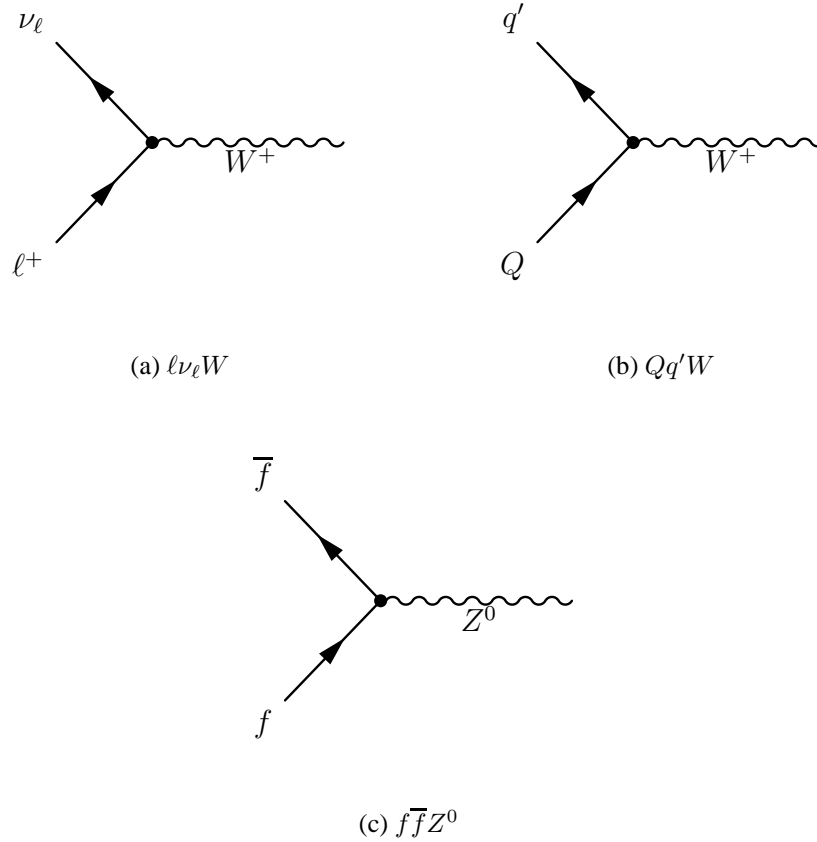
Figure I.5: Fundamental weak vertices.

In terms of quarks, one of the *d* quarks of the neutron decays into a *u* quark through a virtual W^- which then decays into an electron and electron neutrino (See Figure I.6).

The study of the weak interaction dates back to to the end of the 19th century when in 1899 beta (electron) emission was first observed by Rutherford. The continuum energy spectrum of the emitted electrons was a puzzle that lead some to speculate the non-conservation of energy. In 1930, Wolfgang Pauli proposed the existence of a ghost particle in order to explain the continuum energy spectrum of the emitted electrons, the neutrino. Later, in 1933, Enrico Fermi proposed a theory of beta decay that incorporated the weak interaction, although with no gauge boson intermediary and was able to calculate the energy distribution of the electron for these kind of processes. By the end of the 1960's a complete theory of weak interaction was put forward by Sheldon Glashow, Abdus Salam,
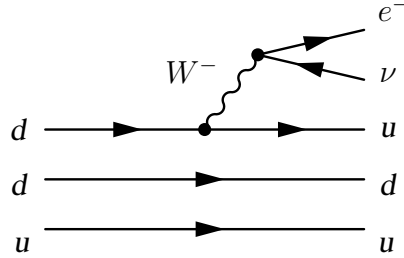
Figure I.6: Feynman Diagram for Beta decay

and Stephen Weinberg [6, 7]. The experimental observation of the weak gauge bosons had to wait until 1983, when they were discovered at CERN.

In addition to the gauge bosons the SM contains one more boson, the Higgs boson. The Higgs boson is yet to be observed experimentally and is of great importance to electroweak theory. The quantum field theory of electro-weak interactions predicts that all the gauge bosons are massless in order to conserve local gauge invariance. This is a significant problem since we know that of the three gauge bosons included in the theory only the photon is massless. By introducing a new scalar field into the theory, the Higgs field, masses for the $W^{\pm}$ and Z^0 are generated leaving the photon massless. The Higgs boson is also responsible for the mass of the quarks. The observation of the Higgs boson is one of the main goals of future experiments like CMS and ATLAS at the Large Hadron Collider (LHC). These experiments are expected to start collecting physics data in 2009.

Unification

One long sought paradigm in physics is the concept of unification of fundamental forces. The idea is that the forces that we think are fundamental today are just different manifestations of one truly fundamental force. The differentiation, known as symmetry breaking, occurs at different energy scales (i.e., the value of the coupling constants evolve

with the Universe). It is expected that the forces are equal in strength at the grand unification theory (GUT) energy scale, around 10^{16} GeV.

The first great unification occurred during the 1860's when Maxwell introduced the famous Maxwell's equations unifying the electric and magnetic phenomena into electromagnetism. The second grand unification is the Glashow–Salam–Weinberg theory mentioned above. This theory does not just explain the weak interaction as one mediated by vector bosons, but unifies the weak interaction with the electromagnetic interaction into the electro-weak force predicting in the process the masses of the gauge bosons.

Precision measurement of the electro–weak and strong coupling constants at LEP excludes the possibility of unification within the Standard Model by more than seven standard deviations [8]. If unification of the coupling constants is to be achieved, the Standard Model needs to be extended. The minimal supersymmetric extension to the Standard Model (MSSM) achieves the desired unification (see Figure I.7) at the expense of introducing a whole new set of unseen particles called super-partners. In MSSM every Standard Model fermion has a bosonic super-partner, while every Standard Model boson has fermionic super-partner. The fact that no super-partner has ever been observed indicates that Supersymmetry (SUSY) is badly broken. Observation of one or more super-partners at the LHC would validate SUSY and the idea of unification of the coupling constants at the GUT scale.

I.1.3 Quark Mixing Matrix (CKM)

The transitions of quarks between generations and the probabilities for those events to occur is more easily understood with the Cabibbo-Kobayashi-Maskawa (CKM) matrix. The three quark generations are grouped in separate doublets

$$\begin{pmatrix} u \\ d' \end{pmatrix}, \quad \begin{pmatrix} c \\ s' \end{pmatrix}, \quad \begin{pmatrix} t \\ b' \end{pmatrix}, \tag{I.5}$$
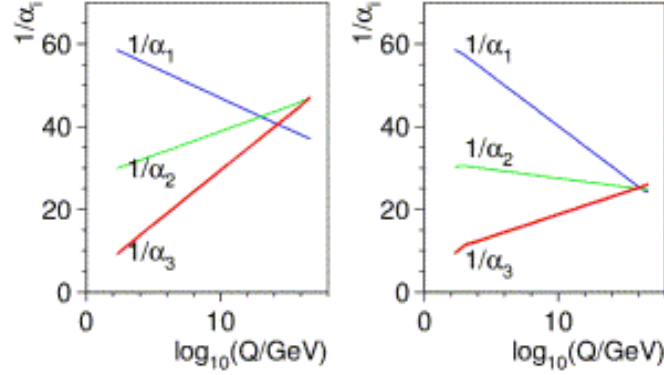
Figure I.7: The running of the gauge coupling constants in the SM (left) and MSSM (right). Supersymmetric corrections to the gauge coupling constants make the unification possible. Reprinted from [9] with permission from Elsevier.

where d', s', and b', the weak eigenstates of the down-type quarks, are linear combinations of the mass eigenstates d, s, and b. The CKM matrix is a 3×3 unitary matrix that relates the weak eigenstates to the mass eigenstates.

$$
\begin{pmatrix} d' \\ s' \\ b' \end{pmatrix} = \begin{pmatrix} V_{ud} & V_{us} & V_{ub} \\ V_{cd} & V_{cs} & V_{cb} \\ V_{td} & V_{ts} & V_{tb} \end{pmatrix} \begin{pmatrix} d \\ s \\ b \end{pmatrix}
\tag{I.6}
$$

Within this framework, the probability for the transition $Q \rightarrow qW^*$, where W^* is a virtual $W^\pm$ gauge boson (only for top decays is the W real), is proportional to $|V_{Qq}|^2$. The diagonal elements are very close to unity and represent transitions within the same generation. These transitions are very likely and are called Cabibbo favored transitions. The unitary condition of the CKM matrix constrains the sum of the squares of the elements of any row or any column to be 1. For example

$$
|V_{ud}|^2 + |V_{us}|^2 + |V_{ub}|^2 = 1.
\tag{I.7}
$$

13

The CKM matrix can be parametrized in different ways. One such parametrization, advocated by the Particle Data Group [10] is

$$
V = \begin{pmatrix}
c_{12}c_{13} & s_{12}c_{13} & s_{13}e^{-i\delta} \\
-s_{12}c_{23} - c_{12}s_{23}s_{13}e^{i\delta} & c_{12}c_{23} - s_{12}s_{23}s_{13}e^{i\delta} & s_{23}c_{13} \\
s_{12}s_{23} - c_{12}c_{23}s_{13}e^{i\delta} & -c_{12}s_{23} - s_{12}c_{23}s_{13}e^{i\delta} & c_{23}c_{13}
\end{pmatrix},
\tag{I.8}
$$

where $c_{ij} = \cos\theta_{ij}$ and $s_{ij} = \sin\theta_{ij}$ for $i, j = 1, 2, 3$. In this case, the CKM matrix is parametrized by three angles, θ_{12}, θ_{13} and θ_{23}, representing the mixing of two generations, and a phase δ. A non-zero value for this phase indicates a violation of the charged-parity (CP) combined symmetry in the weak sector.

In the limit of two quark generations, $\theta_{13} = \theta_{23} = 0$, the CKM matrix reduces to the 2×2 matrix mixing the first two generations.

$$
\begin{pmatrix}
\cos\theta_{12} & -\sin\theta_{12} \\
\sin\theta_{12} & \cos\theta_{12}
\end{pmatrix}
\tag{I.9}
$$

This matrix contains only one parameter, $\theta_{12} = \theta_c \sim 12°$, the Cabibbo angle [11]. In this limit, the decay width of the transitions within the same generations (e.g., $c \to s$) are proportional to $\cos^2\theta_c \approx 0.95$. These are the Cabibbo favored decays mentioned above. The probability for transitions across generations (e.g., $c \to d$) are proportional to $\sin^2\theta_c \approx 0.04$. It is for this reason that these decays are called Cabibbo suppressed decays.

I.2 Semileptonic Decays

Decays that include both hadrons and leptons in the final state are called semileptonic decays. These decays proceed through the weak interaction and provide an ideal environment for the study of the hadronic current. Since the leptons carry no color charge, no strong interaction between the leptons and quarks in the final state is possible. This

allows us to factorize the semileptonic matrix element as the product of the well understood leptonic current and the hadronic current simplifying the process.

An example of a semileptonic decay is the decay of a parent meson $M_{Q\overline{q}}$, with quark content $Q\overline{q}$, into a lighter meson $m_{q'\overline{q}}$, with quark content $q'\overline{q}$, via the emission of a virtual W^+, $Q \rightarrow q'W^*$. The leptonic current (i.e., W^+) decays into an anti-lepton and its corresponding neutrino, $W^+ \rightarrow \ell^+\nu_\ell$. The final decay products have the form $M_{Q\overline{q}} \rightarrow m_{q'\overline{q}}\ell^+\nu_\ell$. The Feynman diagram for this semileptonic decay is shown in Figure I.8. This diagram is known as a *spectator* diagram since only one quark of the parent meson is part of the interaction. The second quark ($\overline{q}$) remains as a spectator and hadronizes with either the daughter quark or with quarks that can materialize from the vacuum. The naïve spectator model provides a very good description of semileptonic decays.
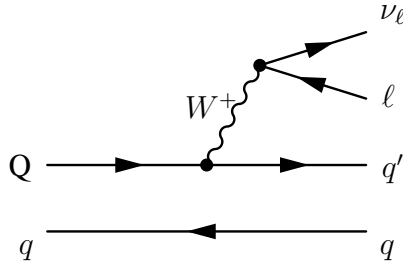
Figure I.8: Spectator diagram for semileptonic decay $M_{Q\overline{q}} \rightarrow m_{q'\overline{q}}\ell^+\nu_\ell$

The differential decay rate for the process $M_{Q\overline{q}} \rightarrow m_{q'\overline{q}}\ell^+\nu_\ell$ in the parent rest mass system is given by

$$d\Gamma(M_{Q\overline{q}} \rightarrow m_{q'\overline{q}}\ell^+\nu_\ell) = \frac{1}{2M_P}|\mathcal{M}(M_{Q\overline{q}} \rightarrow m_{q'\overline{q}}\ell^+\nu_\ell)|^2 d\Pi_3 \qquad (\text{I.10})$$

where

$$d\Pi_3 = (2\pi)^4\delta^{(4)}(P - k - p - p')\frac{d^3k}{(2\pi)^3 2E_m}\frac{d^3p}{(2\pi)^3 2E_\ell}\frac{d^3p'}{(2\pi)^3 2E_{\nu_\ell}}. \qquad (\text{I.11})$$

In this equation P, k, p, p' are the four–momentum of the parent, daughter, lepton, and neutrino, respectively. Conservation of four–momentum requires that $P - k - p - p' = 0$.

The matrix element for this process can be written as

$$\mathcal{M}(M_{Q\bar{q}} \rightarrow m_{q'\bar{q}}\ell^+\nu_\ell) = -i\frac{g^2}{8}V_{Qq'}L^\alpha\frac{g_{\alpha\beta} - q_\alpha q_\beta}{q^2 - M_W^2}H^\beta \tag{I.12}$$

where L^α and H^β are the leptonic and hadronic currents to be defined later and q^2 is the mass squared of the virtual W. The factorization of the matrix element is evident in the above equation.

$$q^2 = (P - k)^2 = (p + p')^2 = M_{W^*}^2 = M^2 + m^2 - 2ME_m \tag{I.13}$$

In most of the cases we are interested in $M_W^2 \gg q^2$ and it is safe to approximate the propagator factor as $\frac{g_{\alpha\beta}}{M_W^2}$. With this approximation and using $\frac{g^2}{8M_W^2} = \frac{G_F}{\sqrt{2}}$ the matrix element becomes

$$\mathcal{M}(P_{Q\bar{q}} \rightarrow X_{q'\bar{q}}\ell\nu) = \frac{G_F}{\sqrt{2}}V_{Qq'}L^\mu H_\mu \tag{I.14}$$

where the G_F is the Fermi coupling constant and $V_{Qq'}$ is the CKM matrix element for the weak transformation $Q \rightarrow q'$. The leptonic and hadronic currents are given by

$$L^\mu = \overline{u}_\nu\gamma^\mu(1 - \gamma_5)v_\ell, \tag{I.15}$$

and

$$H^\mu = \langle k|J_{had}^\mu(0)|P\rangle \tag{I.16}$$

where $J_{had}^\mu = V^\mu - A^\mu$.

The hadronic matrix element can be expressed in terms of one or more form factors and the available four-vectors in the given decay. The form factors are Lorentz invariant

16

functions of q^2 that describe the modifications to the weak current transforming the heavy quark into a lighter quark due to the hadronization process. Different theoretical approaches exist to calculate these form factors (e.g., Lattice QCD, QCD Sum Rules, Quark Model). Predictions made with these methods can then be confirmed or rejected using experimental results.

The kinematic point $q^2 = q^2_{\mathrm{max}}$ is known as the zero-recoil configuration because the daughter meson is nearly at rest in the parent meson rest frame, while the lepton and neutrino are produced nearly back-to-back. Since the daughter quark receives very little momentum kick, it will continue to move mostly unperturbed relative to the spectator quark and gluons. At this point E_m in (I.13) is equal to the mass of the daughter meson and

$$q^2_{\mathrm{max}} = M^2 + m^2 - 2Mm = (M - m)^2. \tag{I.17}$$

At the other end of the kinematic spectrum, q^2_{min} can be approximated to zero except for the case of tau leptons. At this kinematic point the daughter quark receives a large momentum kick relative to the spectator quark resulting in a highly perturbed system.

As we will see in Section I.4.3 the partial decay width for the decay of a pseudo-scalar into a pseudo-scalar (vector) meson + lepton + neutrino is proportional to $|\mathbf{p_m}|^3 \left(|\mathbf{p_m}| \right)$, the momentum of the daughter meson. This factor will go to zero as $q^2 \to q^2_{\mathrm{max}}$ suppressing the rate at high q^2. So, experimentally it is easiest to gather data near q^2_{min}. On the other hand, most calculations are evaluated at specific q^2 kinematic points. For example, calculations using Sum Rules are generally performed at $q^2 = 0$, while in LQCD the form factors are evaluated near $q^2 = q^2_{\mathrm{max}}$.

The functional shape of the form factors are *a priori* undetermined [12]. Nonetheless, dispersion relations can be used to constrain the shape of these form factors and suggest parametrizations than can be used to bridge the gap between where the data is collected and where the calculations are evaluated. The simplest parametrization takes the form given by

17

$$f(q^2) = \frac{f(0)}{1 - q^2/m_{\text{pole}}^2}. \tag{I.18}$$

In (I.18) m_{pole} is the mass of the lowest lying meson composed of the two quarks involved in the weak decay with the same spin and parity quantum numbers.

I.3 Fully Leptonic Decays

Fully leptonic decays are simpler than their semileptonic counterparts. The matrix element for a leptonic process can be written as

$$\mathcal{M}(M_{Q\bar{q}} \to \ell^+ \nu) = -i \frac{G_F}{\sqrt{2}} V_{Q\bar{q}} f_m L^\mu q_\mu \tag{I.19}$$

where f_m is the decay constant. The decay constant represents the amplitude for the two quarks to have zero separation, a necessary condition for the quarks to annihilate. These constants can be calculated using different theoretical approaches, therefore, precision measurements of them is extremely important in refining the theoretical models.

I.4 Charmed Weak Decays

I.4.1 A Brief History of Charm

In early 1960's, before the introduction of the quarks, particles were ordered by their isospin and strangeness quantum numbers. It was observed that transitions with $|\Delta S| = 1$ (e.g., $K^+ \to \mu^+ \nu$) were suppressed with respect to transitions with $|\Delta S| = 0$ (e.g., $\pi^+ \to \mu^+ \nu$). In 1963, Cabibbo introduced the Cabibbo angle [11], $\theta_c \sim 12°$, as a way to relate processes with $|\Delta S| = 0$ and those with $|\Delta S| = 1$. In Cabibbo's model, transitions involving strange conservation were proportional to $\cos \theta_c$ while transitions with strange non-conservation were proportional to $\sin \theta_c$. Soon after, in 1964, Gell-Mann proposed that baryons and mesons were composed of quarks with fractional charge, namely up,

down, and strange, forming an isotopic doublet (up, down) and a singlet (strange) [13].
He speculated that if the quarks were real physical particles with mass, one of the quarks
would be stable while the other two could decay via weak interactions following the rules
set out by Cabibbo a year earlier.

The hadronic current for a three quark model can be written as

$$J^\mu = \bar{D}\gamma^\mu(1 - \gamma_5)U \tag{I.20}$$

where $\bar{D}$ is the linear combination $\bar{D} = \bar{d}\cos\theta_c + \bar{s}\sin\theta_c$. This current has one major flaw,
a term proportional to

$$(d\bar{s} + s\bar{d})\cos\theta_c\sin\theta_c \tag{I.21}$$

appears when we multiply by its adjoint. This term indicates strangeness changing neutral
currents (SCNC), a process that has never been observed. In 1970 Glashow, Iliopoulus, and
Maini (GIM) proposed a fourth quark, the charm quark [14]. With the introduction of the
new quark (I.20) becomes

$$J^\mu = \bar{D}\gamma^\mu(1 - \gamma_5)U + \bar{S}\gamma^\mu(1 - \gamma_5)C \tag{I.22}$$

where the first term is the same as with three quarks, and the second term is the new linear
combination $\bar{S} = \bar{d}\sin\theta_c - \bar{s}\cos\theta_c$. With this current the SCNC term cancels leaving only
terms of the form $u\bar{u} + d\bar{d} + s\bar{s} + c\bar{c}$. This cancellation, known as the GIM mechanism, can
be generalized to six quarks leading to the cancellation of flavor changing neutral currents
(FCNC) processes.

The discovery of the J/Ψ, a $c\bar{c}$ meson, simultaneously by two experiments, one in
Brookhaven [15] and the other in SLAC [16] in November 1974 confirmed the existence
of the charm quark and played a crucial role in validating the predictions of a fourth quark.

I.4.2 Charmed Mesons

The charm quark, with its mass ranging from 1.15 to $1.35\,\mathrm{GeV}/c^2$, is the lightest of the heavy quarks. The lightest charmed mesons are $D^0(c\bar{u})$, $D^+(c\bar{d})$, and $D_s^+(c\bar{s})$ with their respective anti-particles. These charmed mesons can decay only via the weak interaction. In these decays the charm quark is transformed into either a strange quark (Cabibbo favored decay) or a down quark (Cabibbo suppressed decay). There are several diagrams that contribute to the decay rate of the charmed mesons. The most important contributions come from spectator diagrams, annihilation diagrams, and exchange diagrams. Contributions from the more exotic penguin diagrams, and mixing diagrams are highly suppressed in the charm sector.

Two kinds of spectator diagrams are possible, namely the external spectator diagram and internal spectator diagram. The external spectator diagram can give rise to both fully hadronic and semileptonic final states depending on whether the virtual W decays into a lepton or a quark pair, while the internal spectator diagram results in fully hadronic decays as a consequence of the virtual W decaying into a pair of quarks. One of the quarks from the W decay can couple to the daughter quark while the other quark can couple with the spectator quark to form mesons. Since the mesons are color neutral the quarks from the virtual W must have the anti-color of the decayed and spectator quarks. For this reason the internal spectator process is color suppressed.

The annihilation diagram can lead to fully leptonic decays or to fully hadronic decays. In the absence of flavor changing neutral currents this process is only available for the $D^\pm$ and the $D_s^\pm$ mesons since in order for the annihilation to occur the charm quark must decay into the anti-particle of the light quark forming the D meson. For fully leptonic decays the final state consists of only the lepton pair produced from the decay of the virtual W. If the virtual W decays into a quark pair then another quark pair must materialize from the vacuum in order to conserve energy and momentum.

In the exchange diagram the two quarks composing the D meson exchange a W

resulting in a transition of both quarks. As in the case of the hadronic annihilation process, a quark pair must materialize from the vacuum in order to conserve energy and momentum.

I.4.3 Semileptonic Charm Decays

As mentioned in Section I.2, semileptonic decays can give us information on the CKM matrix elements and on the hadronic current via the form factors. Determination of the CKM matrix elements V_{cs} and V_{cd} can be obtained independently of charmed semileptonic decays via charm–tagged W decays and neutrino scattering off valance d quarks [10], therefore the study of charmed semileptonic decays has traditionally concentrated on the understanding and determination of the form factors.

Light charmed mesons are pseudo-scalar (i.e., $J^P = 0^-$) particles. As such, they can decay semileptonically into either another pseudo-scalar or a vector (i.e., $J^P = 1^-$) meson. Examples of decays into pseudo-scalar are $D^0 \to K^- \ell^+ \nu$ (Cabibbo favored) and $D^0 \to \pi^- \ell^+ \nu$ (Cabibbo suppressed). Decays into a vector particle include $D^+ \to \overline{K}^{*0} \ell^+ \nu$ (Cabibbo favored) and $D^+ \to \rho^0 \ell^+ \nu$ (Cabibbo suppressed) shown in Figure I.10.

$D \to P' \ell \nu$

The simplest charmed semileptonic process is that of the decay of the D into a pseudo-scalar meson like a Kaon or a pion. The hadronic current for these processes must be constructed from the available four-vectors of the decay. In these cases, since the daughter meson has no spin, the only available four-vectors are the four-momentum $(p - p')^\mu = q^\mu$ and $(p + p')^\mu$, where p and p' are the four-momentum of the D and pseudo-scalar daughter meson, respectively.

The hadronic current can be written as [17]

$$< P' |V^\mu| D >= f_+(q^2)(p + p')^\mu + f_-(q^2)(p - p')^\mu. \tag{I.23}$$
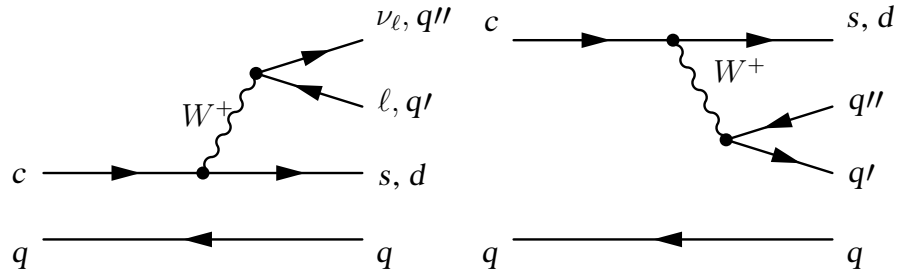
(a) External Spectator Diagram

(b) Internal Spectator Diagram
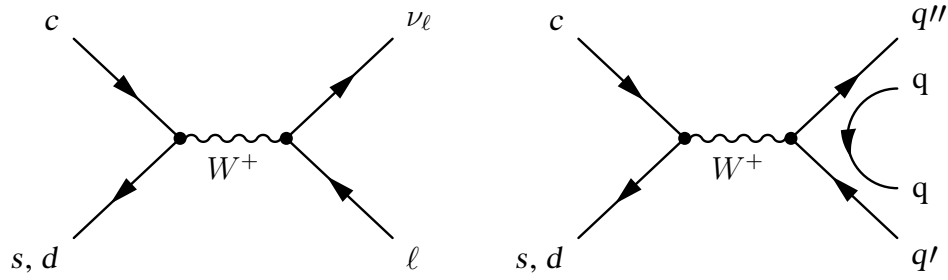
(c) Leptonic Annihilation Diagram

(d) Hadronic Annihilation Diagram
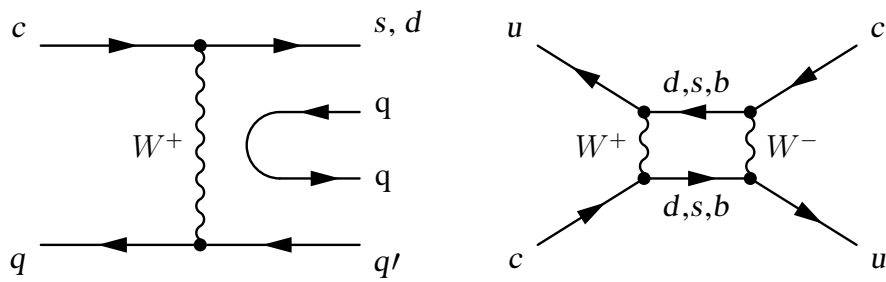
(e) Exchange Diagram

(f) Mixing Diagram

Figure I.9: D Meson decay Diagrams
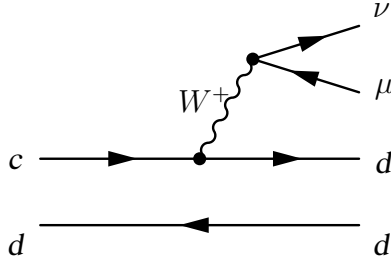
Figure I.10: Spectator diagram for semileptonic decay $D^+ \to \rho^0 \mu^+ \nu$

This can be further simplified and written in terms of only one form factor, $f_+(q^2)$, since in the limit of zero lepton mass $q^\mu L_\mu = 0$. With this simplification to the hadronic matrix element the partial differential decay rate becomes [18]

$$\frac{d\Gamma}{dq^2} = \frac{G_F^2 |V_{q'Q}|^2 p_{p'}^3}{24\pi^3} |f_+(q^2)|^2. \tag{I.24}$$

The $p_{p'}^3$ factor is responsible for the suppression of the rate at $q^2_{\max}$ as mentioned in Section I.2. By integrating the above equation over the available q^2 range and using the pole equation (I.18), it is possible to determine the form factor $f_+(0)$. Generally, experiments measure the relative branching ratio between two similar decay process like $\frac{\Gamma(D^0 \to \pi^- \mu^+ \nu)}{\Gamma(D^0 \to K^- \mu^+ \nu)}$ and then extract the ratio of form factors $\frac{f_+^{D \to \pi}(0)}{f_+^{D \to K}(0)}$.

Using high statistics data it is now possible to use a non–parametric approach to study the q^2 dependence of these decays. The non–parametric approach tests not only the validity of using (I.18) to extrapolate the form factors, but also tests other proposed parametrizations such as

$$f_+(q^2) = \frac{f_+(0)}{(1 - q^2/m_{\text{pole}}^2)(1 - \alpha q^2/m_{\text{pole}}^2)}. \tag{I.25}$$

FOCUS has measured the q^2 dependence of the $D^+ \to K^- \mu^+ \nu$ [19] and was the first to compare the experimental results to those obtained using unquenched lattice QCD methods.

In this theoretical calculation the parametrization (I.25) was used as a way to interpolate and extrapolate between the lattice data points [20]. In addition to the measurement of the q^2 dependence of the decay, it is also possible to measure m_{pole} by fitting the shape of the form factor with either of the parametrization (I.18) or (I.25). This measurement has revealed a significant deviation from the spectroscopic pole confirming the need to include more than one state in the description of the form factors.

$D \rightarrow V'\ell\nu$

The case where a D meson decays semileptonically into a vector meson like a $\overline{K}^*$ or a ρ is more complicated since the hadronic matrix element must include both parts of the current, the vector and the axial components. In this case we have the four–momentum available for the construction of the hadronic current as well as the polarization vector, ε^μ, of the vector meson. The general form for the current is [18]

$$
\begin{aligned}
< V(p',\varepsilon)|V^\mu - A^\mu|D(p) > = & \frac{2i\epsilon^{\mu\nu\alpha\beta}}{M_D + m_V}\varepsilon^*_\nu p'_\alpha p_\beta V(q^2) - (M_D + m_V)\varepsilon^{*\mu}A_1(q^2) \\
& + \frac{\varepsilon^* \cdot q}{M_D + m_V}(p + p')^\mu A_2(q^2) + 2m_V\frac{\varepsilon^* \cdot q}{q^2}q^\mu A_3(q^2) \\
& - 2m_V\frac{\varepsilon^* \cdot q}{q^2}q^\mu A_0(q^2)
\end{aligned}
$$

(I.26)

where

$$
A_3(q^2) = \frac{M_D + m_V}{2m_V}A_1(q^2) - \frac{M_D - m_V}{2m_V}A_2(q^2).
$$

(I.27)

As in the case of the D decaying into a pseudo-scalar, the terms proportional to q^μ are negligible except for the case where $\ell = \tau$. In this limit, the hadronic current written in

24
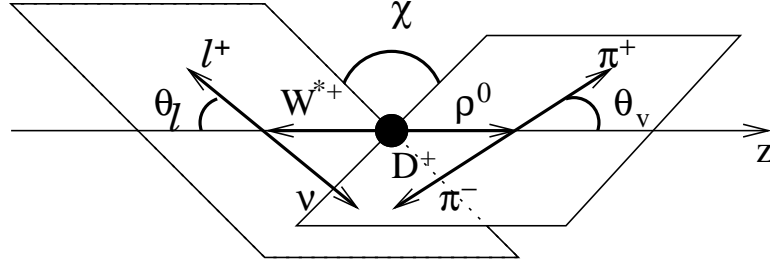
Figure I.11: Angles for the semileptonic decay $D^+ \to \rho^0 \mu^+ \nu$. This is an example of the semileptonic decay $D \to V' \ell \nu$ where the daughter vector meson decays into two pseudo-scalars mesons.

terms of three form factors, $V(q^2)$, $A_1(q^2)$, and $A_2(q^2)$ becomes:

$$
\begin{aligned}
< V(p', \varepsilon) | V^\mu - A^\mu | D(p) > = & \frac{2i\epsilon^{\mu\nu\alpha\beta}}{M_D + m_V} \varepsilon^*_\nu p'_\alpha p_\beta V(q^2) - (M_D + m_V)\varepsilon^{*\mu} A_1(q^2) \\
& + \frac{\varepsilon^* \cdot q}{M_D + m_V}(p + p')^\mu A_2(q^2).
\end{aligned}
\tag{I.28}
$$

For decays in which the vector meson decays strongly into two pseudo-scalar mesons four kinematic variables describe the decay completely, three angles, $\theta_\ell, \theta_v,$ and $\chi,$ and q^2. θ_ℓ is the polar angle between the lepton and the direction opposite to the D in the W^* rest frame where the lepton and neutrino are back to back. θ_v is the polar angle between one of the pseudo-scalar mesons and the direction of the D in the vector rest frame where both pseudo-scalar mesons are back to back. Finally, χ is the angle between the two decay planes. With these definitions the differential decay rate can be written in terms of helicity

amplitudes as [18]

$$\frac{d\Gamma(D \to V\ell\nu, V \to P_1P_2)}{dq^2 d\cos\theta_\ell d\cos\theta_V d\chi} = \frac{3G_F|V_{q'Q}|^2}{8(4\pi)^4} \frac{p_V q^2}{M_D^2} \Gamma(V \to P_1P_2)\times$$

$$\Big[(1 + \cos\theta_\ell)^2 \sin^2\theta_V|H_+(q^2)|^2$$

$$+ (1 - \cos\theta_\ell)^2 \sin^2\theta_V|H_-(q^2)|^2$$

$$+ 4\sin^2\theta_\ell \cos^2\theta_V|H_0(q^2)|^2$$

$$+ 4\sin\theta_\ell(1 + \cos\theta_\ell)\sin\theta_V\cos\theta_V\cos\chi H_+(q^2)H_0(q^2)$$

$$- 4\sin\theta_\ell(1 - \cos\theta_\ell)\sin\theta_V\cos\theta_V\cos\chi H_-(q^2)H_0(q^2)$$

$$- 2\sin\theta_\ell^2 \sin^2\theta_V\cos 2\chi H_+(q^2)H_-(q^2)\Big],$$

$$(I.29)$$

where $H_\pm$, H_0 correspond to the helicity states with $m = \pm 1,\ 0$, and p_V is the magnitude of the three-momentum of the vector in the rest frame of the D. The helicity amplitudes are related to the form factors in (I.28) via

$$H_0 = \frac{1}{2m_V\sqrt{q^2}}\left[(M_D^2 - m_V^2 - q^2)(M_D + m_V)A_1(q^2) - 4\frac{M_D^2 p_V^2}{M_D + m_V}A_2(q^2)\right] \quad (I.30)$$

and

$$H_\pm = (M_D + m_V)A_1(q^2) \mp \frac{2M_D p_V}{M_D + m_V}V(q^2). \quad (I.31)$$

The vector and axial form factor are generally parametrized using a pole dominance form:

$$V(q^2) = \frac{V(0)}{1 - q^2/m_V^2} \quad (I.32)$$

and

$$A_i(q^2) = \frac{A_i(0)}{1 - q^2/m_A^2}, \quad (I.33)$$

respectively.

The Cabibbo favored decay $D^+ \to \overline{K}^{*0}\mu^+\nu$ is the cleanest example of a semileptonic

decay of pseudo–scalar into a vector. In this case $m_V = m_{D_s^*}$ and m_A is set to 2.5 GeV. Using the simple pole parametrization, many experiments have reported the form factor ratios $R_v \equiv V(0)/A_1(0)$ and $R_2 \equiv A_2(0)/A_1(0)$. The results from these experiments are fairly consistent with each other.

The study of the angular distributions of $D^+ \to \overline{K}^{*0} \mu^+ \nu$ revealed a forward–backward asymmetry in $\cos\theta_v$ for events with $M(K^-\pi^+)$ below the $\overline{K}^{*0}$ mass. This is caused by the presence of a non–resonant $D^+ \to K^-\pi^+\mu^+\nu$ s–wave interference [21]. This s–wave component, contributing $\sim 5\%$ to the $D^+ \to K^-\pi^+\mu^+\nu$ spectrum, was also needed in the determination of the $D^+ \to K^-\pi^+\mu^+\nu$ line shape [22]. This result have been confirmed by the CLEO collaboration [23].

The form factors for $D^+ \to \rho^0 \mu^+ \nu$ have never been measured due to lack of statistics but they are expected to have similar values to those of $D^+ \to \overline{K}^{*0} \mu^+ \nu$. For example, the ratio $\frac{V^\rho(0)}{V^{\overline{K}^{*0}}(0)}$ is expected to be between 0.85 to 0.97 for different theoretical models (See for example [24] and references therein).

<center>**CHAPTER II**</center>

<center>**THE FOCUS EXPERIMENT**</center>

FOCUS (Fotoproduction Of Charm with an Upgraded Spectrometer) also known as E831, was a fixed target experiment designed to study charmed particles. The data were collected during the 1996–1997 fixed target run at Fermilab. More than 1 million charmed *Golden Mode* decays (i.e., $D^0 \to K^- \pi^+$, $D^0 \to K^- \pi^+ \pi^- \pi^+$, and $D^+ \to K^- \pi^+ \pi^-$) were fully reconstructed. In this chapter I will describe the beam used to create the charmed particles and the spectrometer used to collect the data. The simulation and reconstruction techniques used for this analysis will be described in subsequent chapters.

II.1 Photon Beam

FOCUS used a photon beam to create charmed particles (hence photoproduction) via photon-gluon fusion. This photon beam was created from protons accelerated at the Tevatron in a multi-step process. In this section this multi-step process is described.

II.1.1 The Fermilab Accelerator Complex

During fixed target data taking the Tevatron was used to accelerate protons to $800 \, \mathrm{GeV}$. In collider mode, the Tevatron reaches 1 TeV. In both cases the final proton energy is reached using a series of five accelerators. After the proton beam has reached the maximum energy in a given accelerator it is transported to the next accelerator until the final energy has been achieved.

The Cockcroft-Walton

The first stage in the proton acceleration is the Cockcroft-Walton accelerator. Here hydrogen gas is ionized by the injection of electrons. The H^- ions are then electrostatically

<center>28</center>

accelerated to an energy of 750 keV as they pass through a series of constant voltage drops. As the beam leaves the the accelerator it passes through an electrostatic chopper. The resulting pulses are then passed through a buncher. The buncher takes the beam pulse and groups the ions in bunches with a frequency of 201.24 MHz. This is the same frequency at which the LINAC, described below, operates.

LINAC

The second stage in the accelerator process is the LINAC (LINear ACcelerator). During this step the H^- ions are accelerated to an energy of 400 MeV. The Fermilab LINAC is about 130 meters long and is composed of drift tubes and side-coupled cavities. Drift tubes accelerate the ions from 750 keV of energy to 116 MeV, while the side-coupled cavities accelerate the ions up to 400 MeV of energy.

Drift tube linacs are composed of hollow, electrically resonant, cylindrical conductors (drift tubes) separated by gaps. An electric field oscillating at high frequency (radio frequencies) provides the acceleration. The phase of the electric field is arranged so that the longitudinal component of the electric field is maximum as the particles are leaving the drift tubes. In order for the particles to keep gaining energy, the particles must be inside the drift tubes before the field changes direction. Because the particles are going faster as they move from one drift tube to the other, every drift tube is longer than the previous to ensure that the particles are inside the drift tube when the field switches.

The Fermilab LINAC contains seven side-coupled cavities. Each module is composed of 4 sections, each section with 16 accelerating cells and 15 coupling cells. Particles in side-coupled cavities are accelerated with high frequency electric fields as is the case with drift tubes. One main difference between the two methods is that particles are not shielded from the electric field when its direction is in the opposite direction. Instead, the shape of the cells concentrates the electric field lines near the center of the cavity creating a stronger acceleration. When the beam enters one accelerating cell the direction of the field is such

that particles are accelerated while the direction of the field is in the opposite direction in the adjacent cells (see Figure II.1).

(a) Field Lines   (b) Accelerating Fields
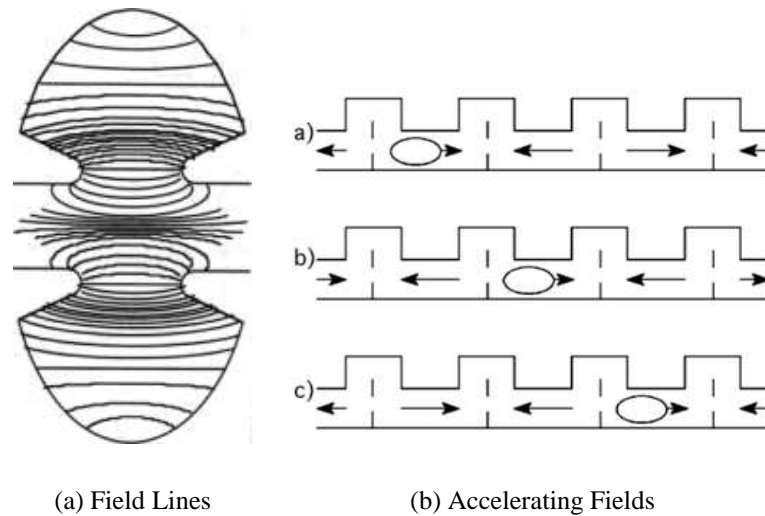
Figure II.1: Schematic diagram of the field lines inside a side–coupled cavity (a) and beam traveling through a series of cavities (b). The shape of the cavity creates a stronger field near the center of the cavity where the beam is traveling.

Booster

The Booster is the third component in the Fermilab accelerator complex. The Booster is a 151-meter diameter proton synchrotron capable of accelerating protons from 400 MeV to 8 GeV of energy. In a synchrotron a series of RF cavities arranged in a ring are used to accelerate charged particles, while a series of magnets steer the particles around the ring. Since the radius of curvature is proportional to the momentum of the particle being accelerated the magnitude of the magnetic field needs to change in order to keep the particles inside the ring. The Booster at Fermilab accelerates the beam with 18 acceleration cavities and the bending is achieved with 96 conventional magnets.

H^- ions coming out of the LINAC are injected into the Booster and striped of the electrons as they pass through a thin carbon foil. The electron catcher captures the stripped electrons while the unstripped ions are swept away leaving only protons circulating the

synchrotron. The protons circulate the Booster 16,000 times and are accelerated from 400 MeV to 8 GeV in 0.033 seconds. Figure II.2 is a schematic diagram of the LINAC and Booster section of the Fermilab Accelerator Complex.
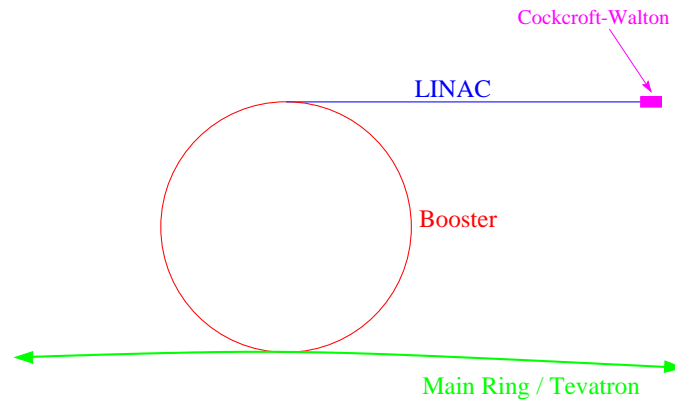
Figure II.2: Schematic diagram of Cockcroft-Walton, LINAC, and Booster at the Fermilab Acceleration Complex.

Main Ring

For FOCUS, the Main Ring, a 1000-meter radius synchrotron accelerator, was the fourth step in the acceleration of protons used in the creation of photons to be delivered to the experimental target. The Main Ring accelerated protons up to 150 GeV and served as an injector for the Tevatron.

The Main Ring, the original particle accelerator at Fermilab was decommissioned shortly after the data taking process to give way to the Main Injector.

Tevatron

The Tevatron is the main accelerator at Fermilab. It is a 1000-meter radius superconducting synchrotron occupying the same ring as the Main Ring. In the Tevatron protons were accelerated up to 800 GeV before being sent to the Fixed Target beamlines. A schematic

diagram the Tevatron and its relation with the Fixed Target beamlines is shown in Figure II.3.
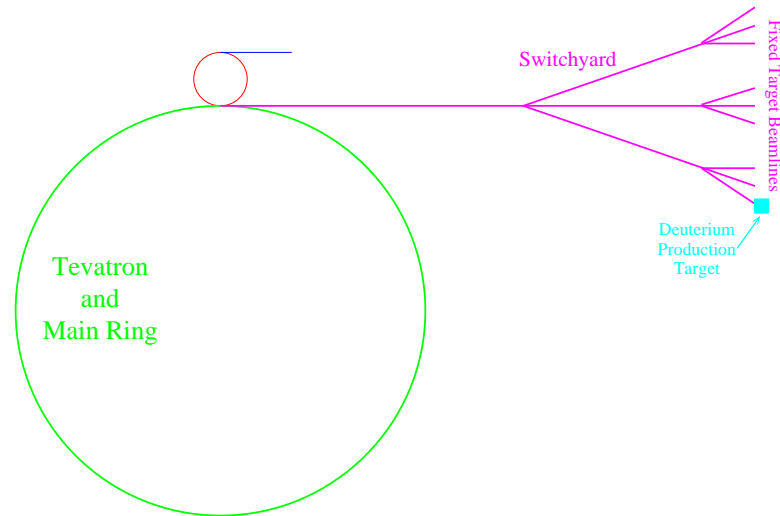
Figure II.3: diagram of Tevatron/Main Ring and fixed target area at the Fermilab Acceleration Complex.

From Protons to Photons

The conversion of the protons delivered by the Tevatron into photons striking the experimental target was done in three steps. In the first step 800 GeV protons interacted with 1.6 meter liquid deuterium production target. Deuterium, with its large A/Z^2, maximizes the hadronic interactions (proportional to A) while suppressing the electromagnetic interactions (proportional to Z^2). High energy particles produced in this target were mainly neutrons, charged and neutral pions, and charged and neutral Kaons. The neutral pions decay rapidly into two photons while downstream of the production target the charged particles were swept away from the beam with the use of magnets. This left only the photons from the decay of the neutral pions and other neutral particles in the beam.

In the second step the photons and neutral hadrons struck a lead radiator of 60% radiation length thickness. Lead has a large ratio of hadronic absorption length to radiation length enhancing the production of electron-positron pairs relative to the hadronic

interactions. The electrons and positrons were then bent around a neutral beam dump that absorbed the non-interacting photons and hadronic neutral components that were produced during the first step. Collimators in combination with the magnets were used to select the momentum of the electrons and positrons that continue in the beam. There were five major periods defined by the energy of these beams in FOCUS as shown in Table II.1. For most of the data taking period FOCUS ran with beam energies of 250 GeV or 300 GeV.

Table II.1: The five different running periods defined by the beam energy used in this analysis. Periods 2–4 correspond to an energy scan.

Period	Energy (GeV)	Run Number	Percentage
1	250	6054–9289	21
2	275	9290–9325	~ 0.4
3	300	9326–9443	~ 1.9
4	325	9444–9511	~ 1.7
5	300	9512–14547	75

In the last step the positrons and electrons were recombined to strike a lead radiator of 20% radiation length thickness producing photons via bremsstrahlung. There was an additional 7% radiation length due to beam monitoring counters (described below) and titanium vacuum windows, for a total effective radiation length of 27%. A diagram depicting the photon beam creation is shown in Figure II.4.

The energy of the photon interacting in the target to produce a charmed event, $k_{\text{interacting}}$ can be expressed as

$$k_{\text{interacting}} = E_0 - E' - \sum k_{\text{additional}} \tag{II.1}$$

where E_0 is the energy of the incident electron before bremsstrahlung radiation, E' is the energy of the electron after radiation loss, and $\sum k_{\text{additional}}$ is the sum of any additional multiple bremsstrahlung photons produced in the radiator.

The momentum of the incident electron/positron was measured with the use of five microstrips, two located before and after the recombining dipoles, and one between

the dipoles. This last plane provided redundant information, thus making the pattern recognition easier.

After the electron/positron has radiated via Bremsstrahlung, it is swept out of the beam using a dipole magnet and its momentum measured in the RESH (Recoil Electron Shower Hodoscope) or POSH (recoil POsitron Shower Hodoscope) detectors. The RESH and POSH detectors were composed of 13 counters each, labeled from 0 to 12 arranged sequentially at large angles. The first counter in each detector (i.e., closest to the beam), RESH0, and POSH0, detected electrons/positrons that did not radiate. Knowing which counter was struck by the recoil electron/positron reveals the momentum of the particle. Finally, $\sum k_{\text{additional}}$ was measured with the Beam Gamma Monitor (BGM), a zero–degree calorimeter located towards the end of the spectrometer.

The efficiency of obtaining photons from protons with a tertiary beam, like the one employed by FOCUS, is rather low. Only around one photon is obtained for every 5000 protons. This inefficiency is compensated by the cleanness of the resulting beam. Having a clean photon beam was important for FOCUS since the hadron-nucleon cross section, σ_{hn} is around 100 times larger than the photon-nucleon cross section, $\sigma_{\gamma n}$. Therefore, any hadronic component in the beam would have produced much higher multiplicity events making the triggering process more challenging.

II.1.2 Photo-production of Charm

Producing charmed events via photoproduction provides some clear advantages. For typical fixed target energies, the relative rate of events producing charmed particles is almost an order of magnitude larger for photoproduction ($\sim 0.6\%$) than for hadroproduction ($\sim 0.08\%$). In addition to the cross–section differences between both production mechanisms, in photoproduction, the photon acts as a $x \sim 1$ parton producing higher momentum charmed events. This becomes especially important in fixed target experiments where these events are more likely to travel within the acceptance of the spectrometer and
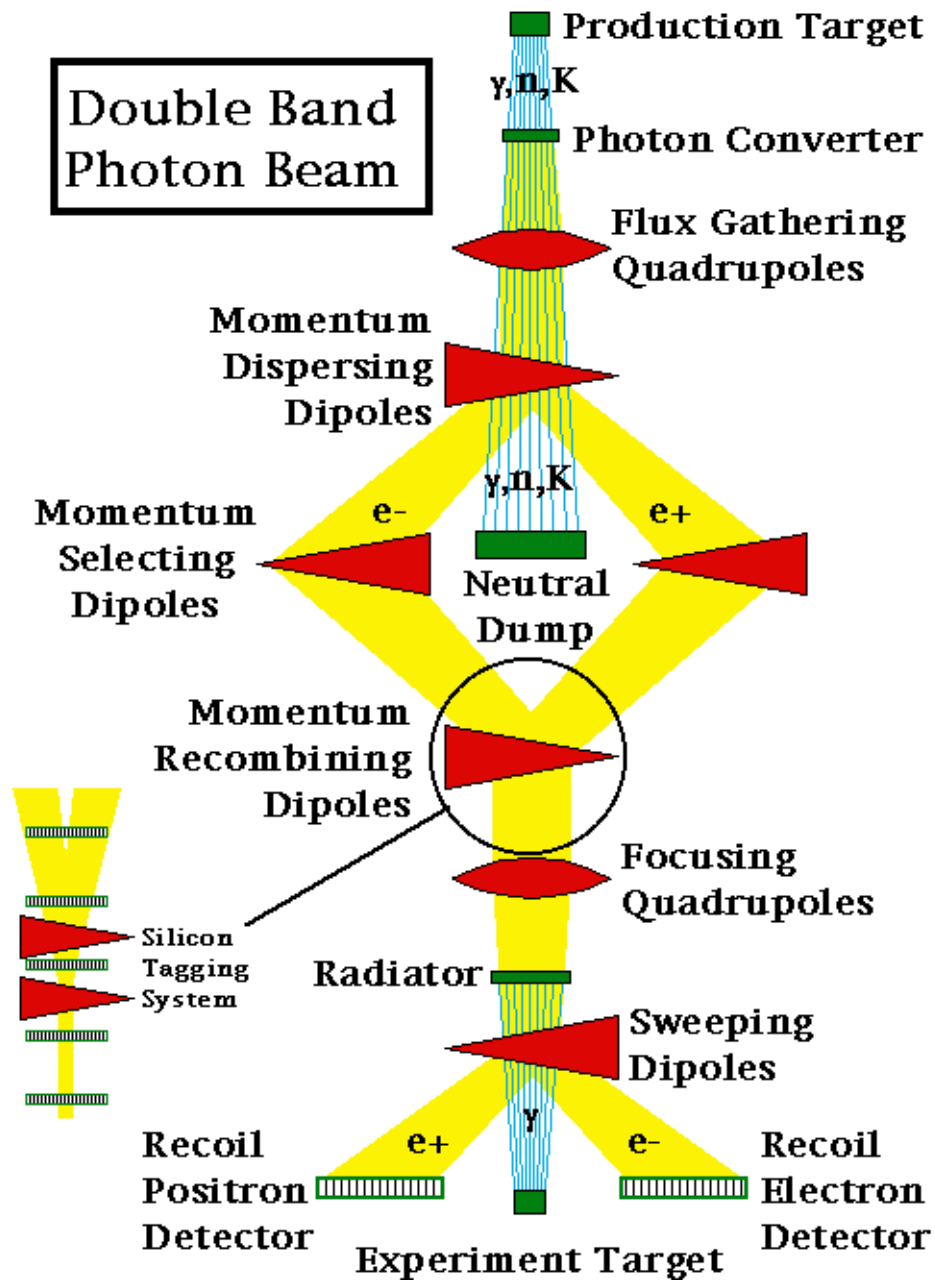
Figure II.4: Schematic diagram of the FOCUS beam.

have larger Lorentz boosts making the separation of the production and decay vertices easier to find.

Another advantage of photoproduction relative to hadroproduction is that its main background is the creation of $e^- e^+$ pair with a known distribution (Bethe-Heitler). This background is easy to identify since these electron–positron pairs travel down the spectrometer very close to the beamline. A requirement that the tracks are inconsistent with having zero–degree with respect to the beam is enough to suppress most of this background.

The main mechanism for the production of charm using high energy photons is the photon-gluon fusion (PGF) process. To leading order (LO), the incoming photon interacts with a radiated gluon from one of the nucleons in the target to produce a $c\overline{c}$ pair. A diagram for this process (to leading order) is shown in Figure II.5.
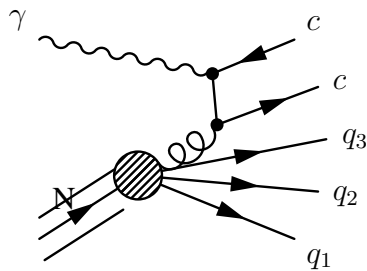
Figure II.5: LO Photon–gluon fusion diagram.

II.2 The FOCUS Spectrometer

The FOCUS spectrometer was a two magnet spectrometer with excellent vertex resolution and particle identification. The spectrometer was an upgrade of the spectrometer used by E687 [25]. Most of the detectors and reconstruction algorithms were improved for FOCUS. Briefly, the FOCUS spectrometer utilized Silicon microstrips for vertexing and tracking near the target region, proportional wire chambers (PWC) and straw tubes for tracking and vee reconstruction, two analysis magnets for momentum determination, three threshold Čerenkov for particle identification, hadronic and electromagnetic calorimeters

for energy measurement, and muon detectors. In the following sections, I describe the main detectors of the FOCUS spectrometer in the order they are first encountered by a high energy particle going in the direction of the beam. We start with the most upstream element, the target, and end at the most downstream, the inner muon detectors. A schematic diagram of the FOCUS spectrometer is shown in Figure II.6.

II.2.1   The Target

FOCUS used Be and BeO targets for the production of charmed particles . The choice of target was based mostly on maximizing the number of hadronic interactions while at the same time minimizing electromagnetic interactions. BeO, with an interaction length to radiation length ratio close to 2 is good for hadronic production.

Another important consideration in the selection of the target material was the desire to have a significant proportion of events with decay vertices outside of the target material. Based on experience gained in the E687 experiment we know that events where the secondary vertex occurs outside the target material have a significantly better signal to noise ratio than those where the secondary vertex is reconstructed inside the target. This is because inside the target secondary vertices can come from secondary hadronic interactions as well as from decays. In contrast, outside the target the secondary vertices are mostly coming from the decay of relatively long lived particles like charmed mesons. With a denser material like BeO the target can be made thinner enhancing the number of events with vertices occurring outside of the target.

The number of events with secondary vertices outside the target material is also increased by splitting the target into smaller pieces and having air gaps between the targets. Having a longer target can degrade the spatial vertex resolution if all the tracking is done downstream of the target. Tracking detectors in between the target elements can compensate for this lost resolution.

During most of the data taking period FOCUS used a segmented BeO target embedded
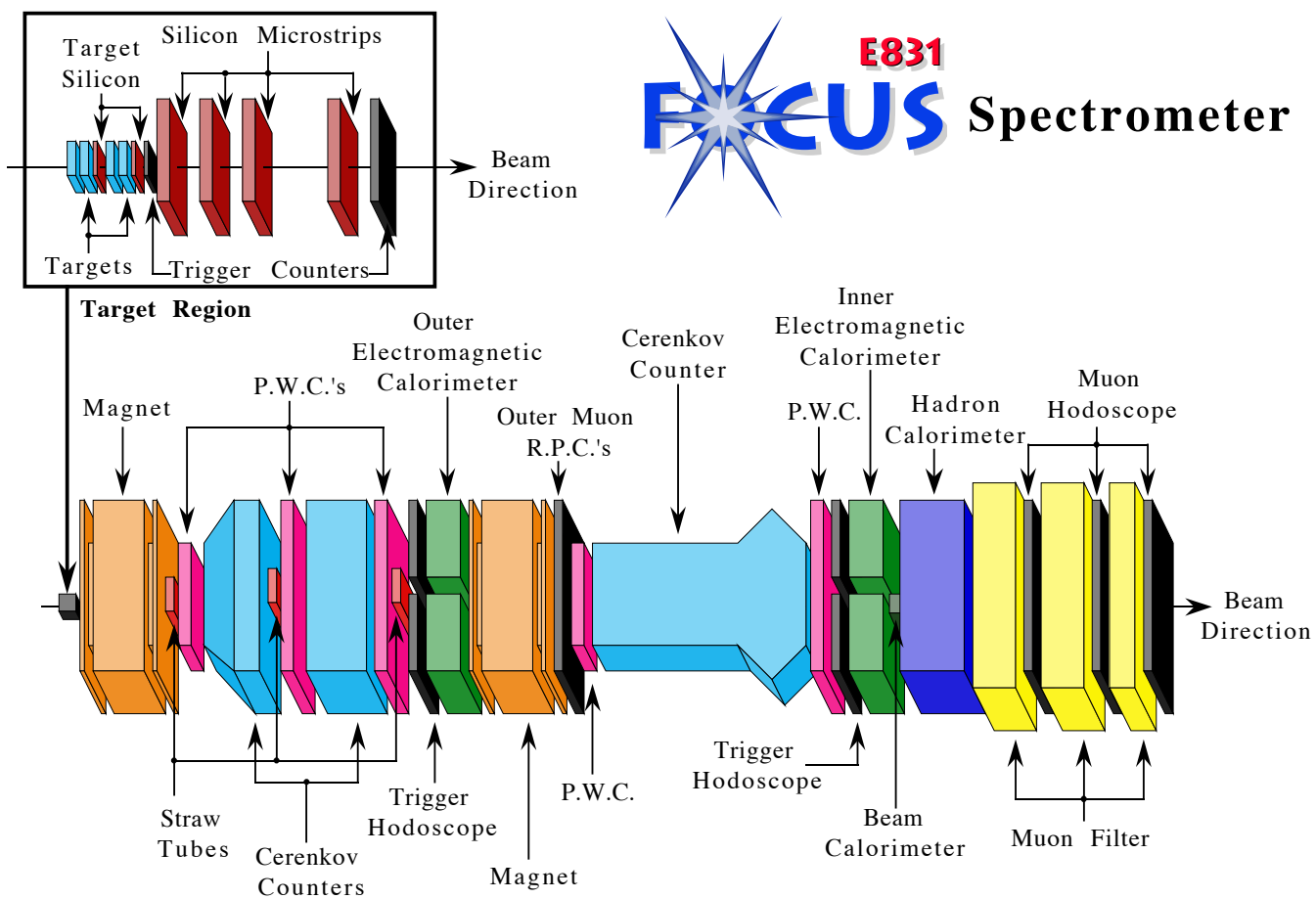
Figure II.6: Schematic diagram of the FOCUS spectrometer. The insert shows the target region.

with four silicon microstrip planes called the Target Silicon Strip Detector (TSSD)[1]. Each of the four targets was 3 cm square perpendicular to the beam and 6.75 mm long in the beam direction. A decay region of 1 cm followed each of the target elements. Four stations of Silicon Strip Detectors (SSD) and five trigger counters, TR1 and TR2 (an array of four counters), completed the target region. The final target configuration is shown in Figure II.7.
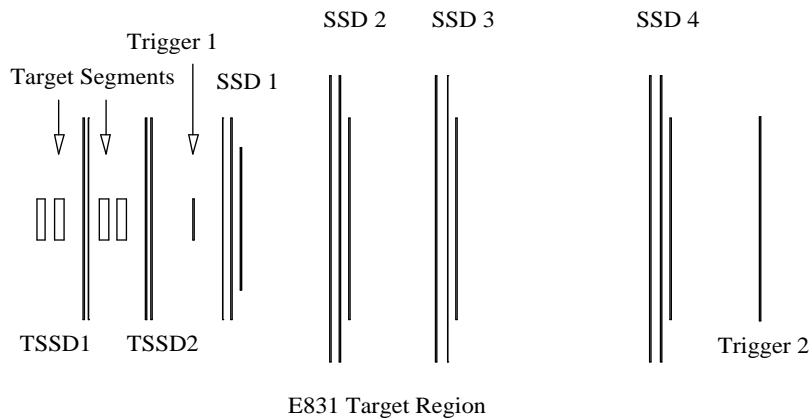
Figure II.7: Final target configuration used by FOCUS. The four BeO targets along with silicon microstip detectors (TSSD and SSD) and trigger hodoscopes (TR1 and TR2) are shown in the diagram. The beam enters from the left.
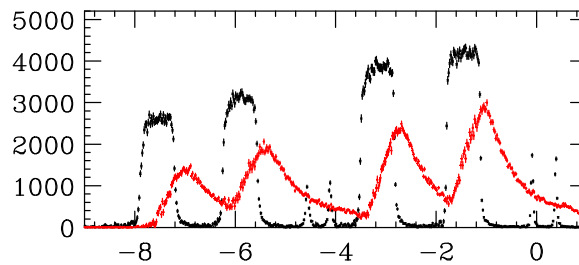
Figure II.8: Distribution of z–position for primary (black) and secondary vertices for Golden Mode charmed events.

---

[1]During the early running periods FOCUS used both a Be target as well as a BeO target without the embedded TSSD.

II.2.2 The Target Silicon Strip Detector

The Target Silicon Strip Detector (TSSD) was the first element of the FOCUS tracking system. As stated previously, increasing the number of secondary vertices occurring outside of the target introduced a loss in tracking resolution due to the longer lever arm associated with a long segmented target. In order to recover some of this lost resolution FOCUS installed silicon microstrip detectors among the target elements [26]. This has the added advantage of providing measurement points closer to the interaction regions. The TSSD was in place for about 2/3 of the running.

A charged particle passing through a solid state detector like the silicon microstrip detector used by FOCUS will leave ionizing energy manifested in the liberation of electron-hole pairs within the detector. The detector was run in reversed bias mode such that the electric field between the anode and the cathode separated the liberated charge before it could recombine. The liberated charge was then collected for amplification and digitization.

Two planes of TSSD doublets aligned at $\pm 45°$ from the horizontal were placed in between the second and third target elements and in between the fourth target element and the first trigger counter. Each view consisted of 1024 strips with a pitch of 25μm. The active region in each plane was 2.5 cm $\times$ 5 cm.

Along with the increased vertex resolution, the inclusion of the TSSD system yielded an improvement on the average proper time resolution for charmed particles of $\sim 20\%$ [26].

II.2.3 Silicon Strip Detectors

After the first trigger counter, TR1, and before TR2 tracking was done with four stations of silicon microstrip detectors (SSD) with three views each. The views were oriented at $\pm 45°$ and $90°$ from the horizontal. In each plane the inner region had twice the resolution of the outer region to resolve low angle tracks. The first SSD station had a 25μm pitch in the inner region and a 50μm pitch in the outer region. The remaining three stations had

inner region pitch of 50μm and 100μm outer region pitch. Each of the twelve planes had 688 readout channels. The properties of the four SSD stations are summarized in Table II.2.

Table II.2: Summary of the properties of the four SSD stations.

Station	Active Area (cm^2)		Pitch (μm)	
	Total	High Res.	Inner	Outer
1	2.5×3.5	1.0×3.5	25	50
2	5.0×5.0	2.0×5.0	50	100
3	5.0×5.0	2.0×5.0	50	100
4	5.0×5.0	2.0×5.0	50	100

II.2.4 Analysis Magnets

The momentum of charged particles can be determined by measuring the change in the trajectory of the particle before and after it passes through a uniform magnetic field. In FOCUS this was accomplished with the use of two large aperture dipole magnets with opposite polarities. The first magnet, M1, was located between TR2 and the first PWC station. The second magnet, M2, was located in the center of the spectrometer between the Outer Electromagnetic Calorimeter and P3, the fourth PWC station. The transverse momentum kick provided by the magnets was $0.40\,\mathrm{GeV}/c$ and $0.85\,\mathrm{GeV}/c$ for M1 and M2, respectively. With the magnets running in opposite polarities particles had the tendency to come back to their undeflected trajectories as they reached the end of C3, the last Čerenkov detector. More importantly, e^+e^- pairs produced in the target were focused and passed through the hole in the electromagnetic calorimeter and into the Beam Calorimeter.

II.2.5 Proportional Wire Chambers

Downstream of the first magnet the tracking was done with the use of proportional wire chambers (PWCs). A PWC is a gas filled enclosure in which parallel sense wires are sandwiched between planes of high voltage wires. A charged particle passing through the chamber ionizes the gas and the freed electrons are accelerated towards the sense wires for

collection. As the electrons from the initial ionization are accelerated towards the sense wires they in turn ionize the gas further creating an avalanche of electrons reaching the anodes. The positive ions moving away from the sense wire generate the signal that is amplified and converted into a spatial measurement.

FOCUS used five stations of proportional wire chambers. Each station had four planes measuring the X, Y, U, and V directions. The X and Y views were perpendicular to each other while the U and V planes were inclined at $\pm 11.3°$ from the horizontal as shown in Figure II.9. The five stations were labeled (from most upstream to most downstream) P0, P1, P2, P3, and P4. The gas used in all five stations was a 75% argon and 25% ethane mixture bubbled through alcohol. P0 and P3 were located right after the first and second magnet, respectively, therefore the properties of these chambers reflect their limited acceptance due to the magnet aperture.The properties of the PWC stations are summarized in Table II.3.

Table II.3: Summary of the properties of the five PWC stations.

Station	Wire Spacing	Wires/plane				Size $(X \times Y)$	Position (cm from target)
		X	Y	U	V		
P0	0.080"	376	640	640	640	$76 \times 127 \text{ cm}^2$	403
P1	0.130"	480	704	768	768	$152 \times 229 \text{ cm}^2$	644
P2	0.130"	480	704	768	768	$152 \times 229 \text{ cm}^2$	879
P3	0.080"	376	640	640	640	$76 \times 127 \text{ cm}^2$	1,444
P4	0.130"	480	704	768	768	$152 \times 229 \text{ cm}^2$	2,286

II.2.6 Straw Tube Chambers

The last element of the FOCUS tracking system consisted of three straw tube stations. Because straw tubes can be reliably operated in high rate environments, these stations were designed to cover the central region, where e^+e^- pairs produced in the target travel. The straw tubes were used as a redundant system in case the PWC stations could not cope with these high rates.

Anode Wire Orientation

(Looking downstream)
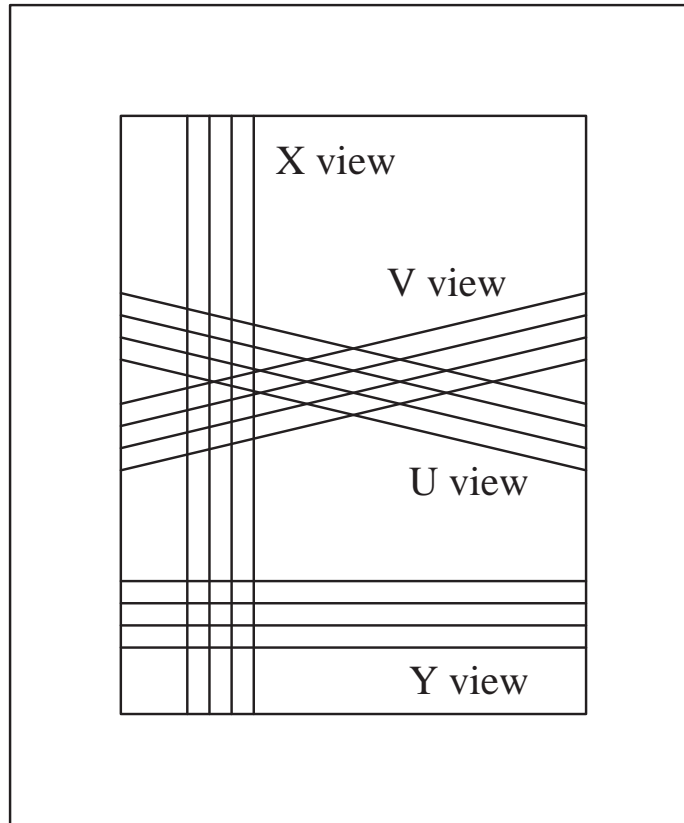
Figure II.9: Orientation of the PWC wires.

The detection mechanism of the straw tubes is similar to the one used in PWC stations. The main difference being that the gas is enclosed within a single tube with a sense wire in the center. The tube walls are grounded while the wire is kept at high voltage making the freed ionization charge drift towards the wire where the charge is collected.

The first two straw tube stations, ST0 and ST1 were placed in front of the first and second PWC stations, respectively. The third station, ST2, was placed behind the third PWC station. Each station had three views, one vertical and two aligned at $\pm 11.3°$ from the vertical, with each of the views having three sets of tubes. A diagram of a straw tube station is shown in Figure II.10. The tubes had a diameter of 5 mm.
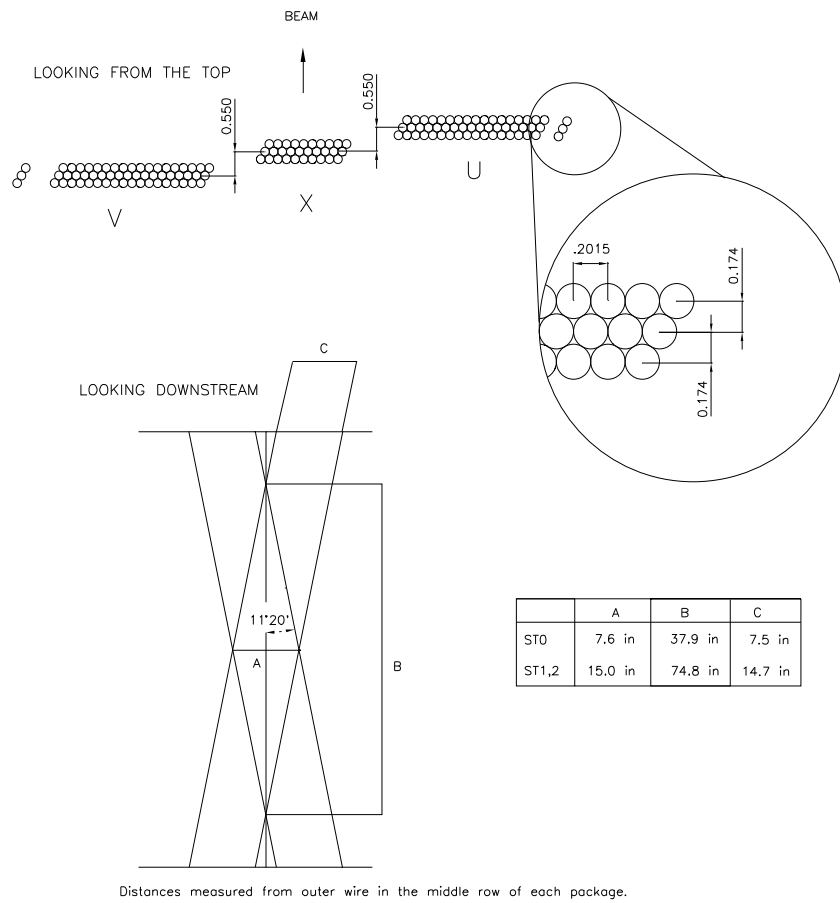
Figure II.10: Diagram showing the arrangement of the straw tube stations.

II.2.7 Čerenkov Detectors

Charged particle identification was done with three multi-cell threshold Čerenkov detectors. These three detectors were able to identify pions, Kaons, electrons and protons. Although the identifications of muons using the Čerenkov systems is possible, the limited momentum range in which the muons can be separated from pions makes it inefficient.

Čerenkov radiation is emitted when a charged particle is traveling through a medium

faster than the speed of light inside that medium (c/n):

$$\beta = \frac{p}{E} = \frac{p}{\sqrt{p^2 + m^2}} > \frac{1}{n} \tag{II.2}$$

where n is the index of refraction of the medium. The angle of the emitted light is described by [27]

$$\cos \theta_c = \frac{1}{n\beta}. \tag{II.3}$$

The number of photo-electrons is proportional to $L \sin^2 \theta_c$, where L is the length of the radiator. Threshold Čerenkov detectors exploit the fact that radiation will only be emitted when the momentum of a particle with mass m is greater than $p_{\text{threshold}}$ given by

$$p_{\text{threshold}} = \frac{m}{\sqrt{n^2 - 1}}. \tag{II.4}$$

As mentioned before FOCUS used three Čerenkov detectors labeled C1, C2, and C3 (from upstream to downstream). The medium for each Čerenkov detector was carefully selected to be able to distinguish pions from Kaons and protons in a wide momentum range. With three threshold Čerenkov detectors identification can be achieved by looking at the on/off status of the three detectors for a given track. As an example, a 25 GeV/c track that leaves signal in all three detectors is identified as a pion, while a $25\text{GeV}/c$ track that leaves a signal only in C2 is identified as a Kaon. The threshold momenta for pions, Kaons, and protons along with the gases used in each Čerenkov detector are summarized in Table II.4.

Table II.4: Characteristics of the three Čerenkov detectors.

Detector	Gas	$p_{threshold}(\text{GeV}/c)$			Length (cm)	No. Cells
		pion	Kaon	proton		
C1	He-N$_2$	8.5	29.9	56.8	180.3	90
C2	N$_2$O	4.5	16.2	30.9	188.0	110
C3	He	17.0	61.0	116.2	703.6	100

C1 was the most upstream of the Čerenkov counters and was located between the first two PWCs. The counter contained a He-N$_2$ mixture yielding a pion threshold of $8.5\,\mathrm{GeV}/c$. C2, located between the second and third PWCs used N$_2$O providing a pion threshold of $4.5\,\mathrm{GeV}/c$. The last counter, C3, was located downstream of the second magnet between the fourth and fifth PWCs. The gas used in this counter was He yielding a pion threshold of $17\,\mathrm{GeV}/c$.

II.2.8 Calorimetry

The energy of particles, both neutral and charged, can be measured with the use of destructive processes inside calorimeters. Electromagnetic calorimeters measure the energy of photons and electrons via pair production and Bremsstrahlung, while hadronic calorimeters measure the energy deposited by hadrons.

A high energy electron entering an electromagnetic calorimeter will emit Bremsstrahlung radiation as it is accelerated in the field of the atomic nucleus. If the energy of the Bremsstrahlung photon is large enough, an electron-positron pair is created as the resulting photon interacts with an adjacent nucleus. This process is repeated as the particles move through the calorimeter losing energy with each interaction. This multiplication process is called a shower. The resulting electromagnetic shower reaches a maximum and then stops suddenly when the energy of the particles inside the shower falls bellow E_c, the energy needed for electrons to radiate through Bremsstrahlung. Below E_c the particles loose energy mostly by ionization processes.

The number of particles at the maximum is approximately

$$N_{max} \approx \frac{E_0}{E_c} \tag{II.5}$$

where E_0 is the energy of the incident particle. By measuring the number of particles in the shower the energy of the incident particle can be determined.

Hadronic calorimeters function with the same principles as electromagnetic calorimeters. The main difference is the energy loss process involved. Hadrons interacting strongly in the calorimeter will loose energy mainly via pion production with all three, $\pi^\pm$ and π^0, produced at more or less the same rate. Other hadrons are also produced although with a much lower multiplicity.

About one third of the pions produced in the shower are neutral pions that quickly decay into two photons. Therefore, there is an electromagnetic component in the hadron shower. As in the case of the electromagnetic showers, the multiplication stops as soon as the energy of the particles in the shower is lower than the energy to produce pions.

FOCUS made use of three calorimeters to measure the energy of the produced particles. The Outer Electromagnetic Calorimeter (OE), located before M2, the Inner Electromagnetic Calorimeter (IE), located after the last PWC, and the Hadronic Calorimeter (HC), located after the IE.

The OE, located 900 cm from the target, was used to reconstruct showers initiated by charm radiative processes and π^0 decays with photon energy $(0.5 \leq \mathrm{E}_\gamma \leq 15)~\mathrm{GeV}$. It was also capable of extending the e/π discrimination beyond the Čerenkov range.

The detector, made of Pb plates and plastic scintillator layers corresponding to 19 radiation lengths and 1.4 interaction lengths, was $255 \times 205~\mathrm{cm}^2$ with an internal aperture of $55 \times 88~\mathrm{cm}^2$ that matched the aperture size of M2. A nine cm vertical gap along the detector protected the detector against the Bethe-Heitler pairs and non-interacting photons emerging from the target.

The scintillator layers were made of strips coupled to photomultipliers for the light readout. There were a total of 1036 readout channels associated with OE. The counters were arranged in nine independent views along the beam direction and four independent quadrants in the x–y plane. A module of S–Z strips oriented at $\pm 45°$ angles provided the horizontal–vertical matching.

An additional scintillator tile array was located between OE1 and OE2. This array was

used to recover showers in the small angle, high occupancy region. The use of this array also improved the horizontal–vertical matching as well as improved the π^0 mass resolution by rejecting fake matches. For a full description of the OE and its performance, see [28]. A schematic view of the OE can be seen in Figure II.11.

E831 FOCUS Outer em calorimeter
ELEVATION VIEW (NOT TO SCALE)
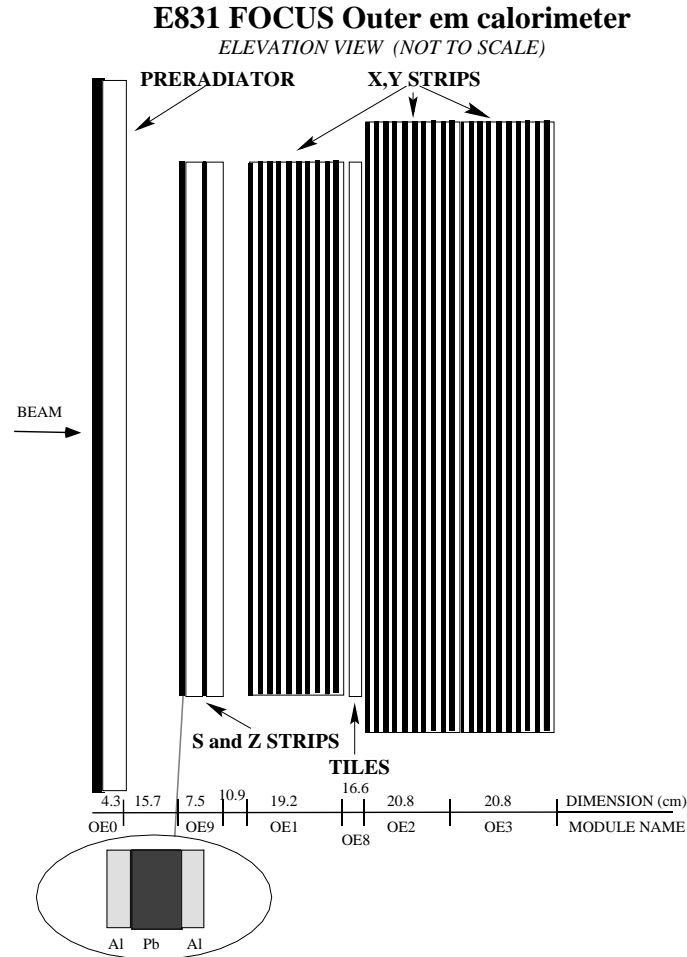
Figure II.11: Longitudinal structure of OE showing the layout of absorber and scintillator planes.

The IE was a lead glass calorimeter that detected photons and electrons that passed through M2. It consisted of 802 blocks, 37 blocks high and 22 blocks wide (3 blocks in each corner were missing) arranged in a tower geometry. This was equivalent to 18.75 radiation lengths and 2.2 interaction lengths. A shielded vertical gap 14 cm wide between the 11th and 12th columns allowed e^+e^- pairs coming from the target to passed through without producing a shower. The geometry of the IE can be seen in Figure II.12.
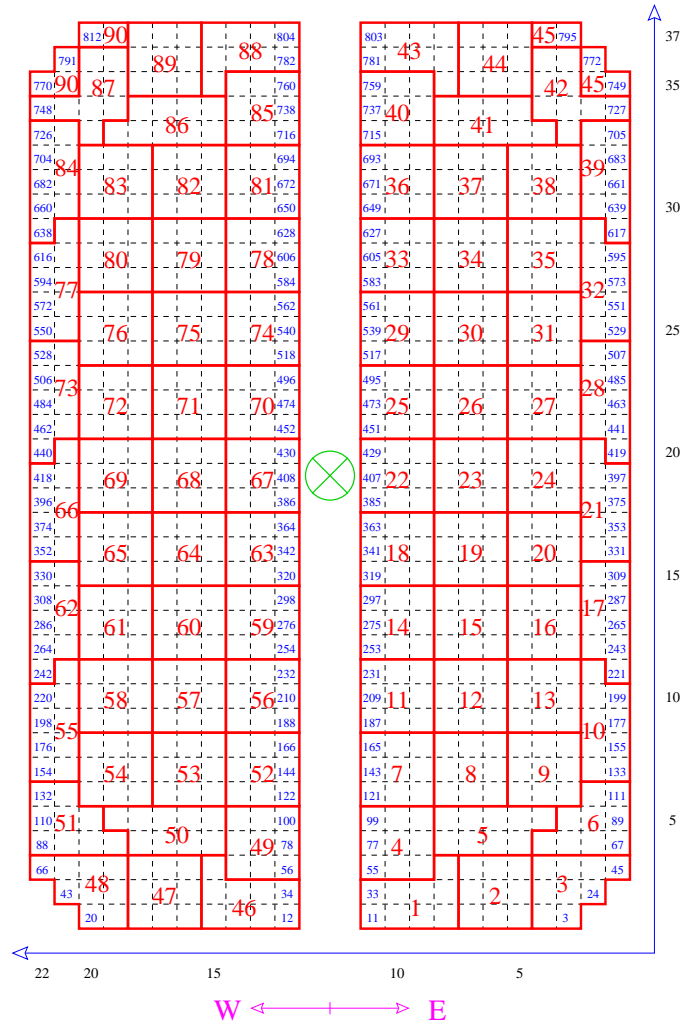
Figure II.12: Block arrangement for the IE. The dash lines represent individual blocks. For triggering purposes, blocks are summed together in groups of nine. The grouped blocks are enclosed within the red lines.

The HC was an iron-scintillator tile calorimeter. The main use of the HC was to trigger on the total hadronic energy released in the event. The HC was made with 28, $305 \times 208 \times 4.4$ cm^3 iron absorber plates (the first two planes were 6.4 and 5.1 cm thick, respectively) inter-spaced with 0.7 cm thick scintillator planes. This resulted in a calorimeter with 7.8 interaction lengths and 72.7 radiation lengths. Each plane consisted of 66 tiles of different sizes. The 28 planes were grouped together in three sections. The first section consisted of the first 9 most upstream planes, the second 15 planes made up the second station, while the last 4 planes comprised the last section. Fiber from tiles occupying the same x–y position in the same station were grouped together and connected to the same photomultiplier forming a tower. These arrangement resulted in 66 towers per section for a total of 198 readout channels.

The HC and its performance are fully described in Reference 29. A schematic diagram showing the HC is shown in Figure II.13.

II.2.9 **Muon Detectors**

The principle behind an efficient muon detector system lies in the great penetrating power that muons exhibit. Muons, with a mass more than 200 times heavier than electrons, experience very little energy loss when passing through material. Therefore, muons are able to pass through large amount of material without undergoing destructive processes. This penetrating power allows the muon systems to be located behind large amounts of shielding material, usually in the form of steel, that will filter most other particles.

FOCUS used two muon detector systems, the Outer Muon system (OMU) and the Inner Muon system (IMU). The OMU, located downstream of M2 utilized Resistive Plate Chambers (RPC). This muon detector detects low momenta/high angle muons that follow a trajectory outside the acceptance of M2. The Outer Electromagnetic Calorimeter and the steel from M2 acted as filters for the OMU.

Resistive plate chambers are gas-filled parallel plate detectors capable of providing
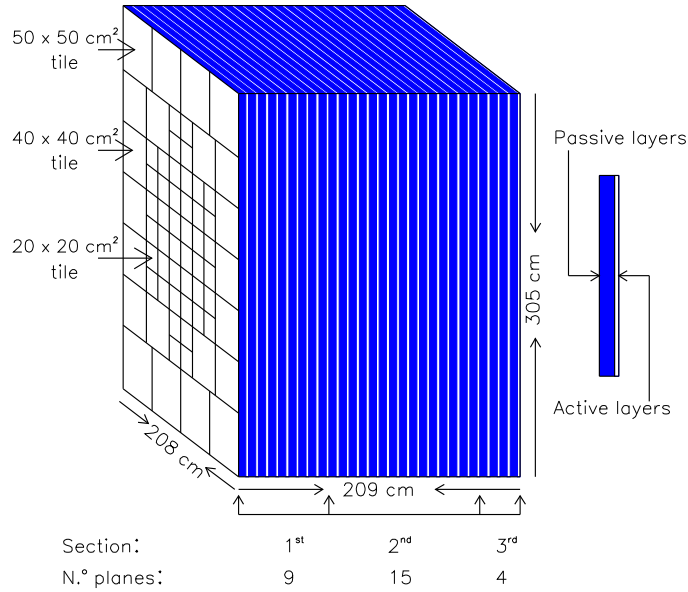
Figure II.13: Schematic view of the HC.

good spatial and timing resolution. RPCs don't use wires. Because of this, RPCs are ideal for measurements in regions where magnetic fields are present. In the case of FOCUS the OMU was in the vicinity of the M2 fringe field.

The OMU detector consisted of 24 RPC modules arranged in three views, x, y, and, a $45°$ u–view. The gas used was a mixture of 71% Argon, 8% Isobutane, *5% Freon*, and 16% CO_2. A schematic diagram of OMU and its relation with M2 is shown in Figure II.14.

The Inner Muon Detector was located at the end of the spectrometer. The IMU consisted of three stations of scintillating counter arrays labeled MH1, MH2, and MH3. MH1 and MH2 have x and y views while MH3 provided u and v views at a $45°$ angle. Each muon station was placed behind a filter made of 61 cm, 129 cm, and 69 cm of steel, for MH1, MH2, and MH3, respectively. In addition, the Hadron Calorimeter and the Inner
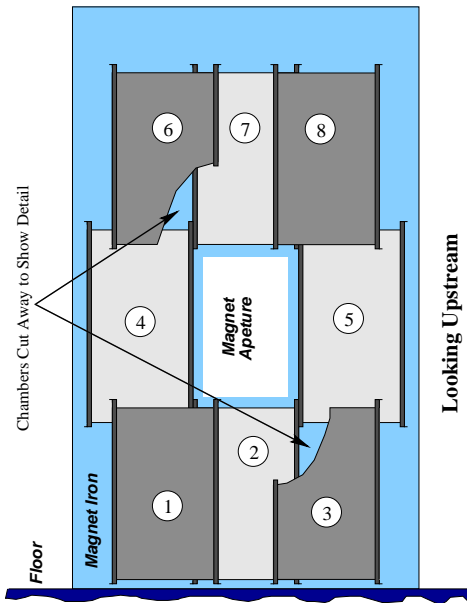
Figure II.14: Schematic diagram of the OMU system. The figure shows the arrangement of the RPC modules in relation to the M2 aperture. Each labeled module contains 3 views, x, y, and, u.

Electromagnetic Calorimeter also functioned as a filters for the IMU. The arrangement of the IMU counters is shown in Figure II.15.

II.2.10 Trigger

Not every event coming out of the target contains interesting physics. Because computing and storage resources are finite, every effort should be made to select only the most promising events for storage onto tape. This is accomplished by looking at the signals from different detectors for every event to determine if the signature of an interesting event is present or not. If the signature is present then the event is stored onto tape for offline analysis, otherwise the event is discarded and the same process is repeated again. This process is called triggering.

Timing considerations are very important in the development of an efficient trigger. In some cases, while an event is being analyzed to determine if it satisfies the trigger
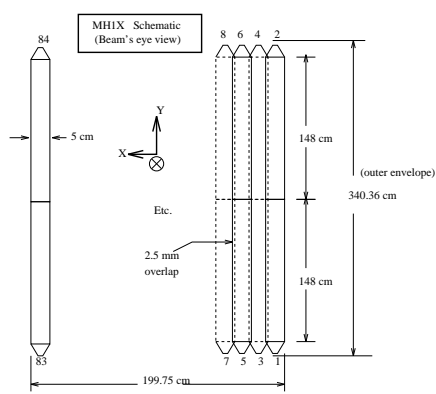
(a) X-view of MH1
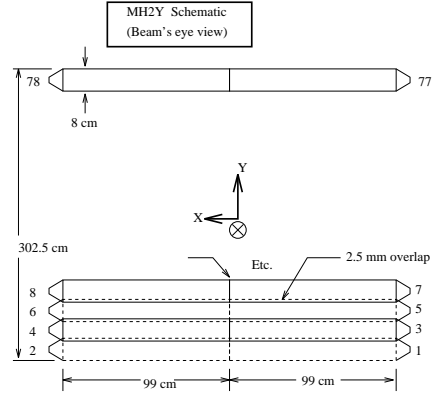
(b) Y-view of MH2
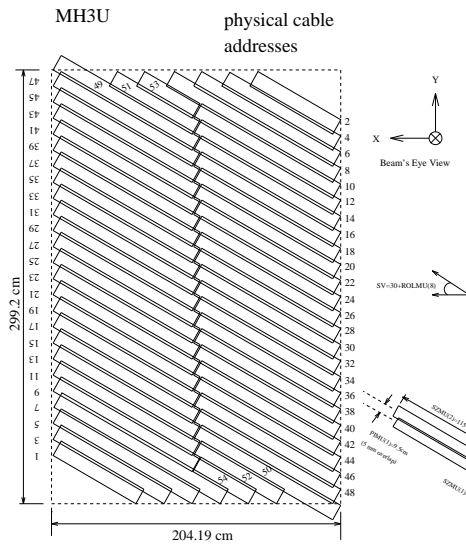
(c) U-view of MH3
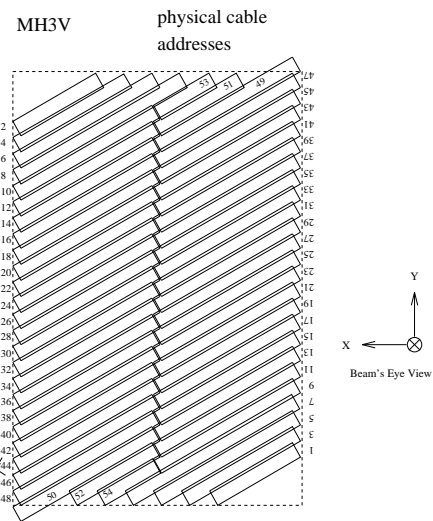
(d) V-view of MH3

Figure II.15: Arrangement of the IMU detector counters.

requirements the experiment can not take data. Therefore, the trigger decision must be made as fast as possible to minimize the detector dead-time.

The trigger decision in FOCUS was taken in two steps, the Master Gate (MG) and the second level trigger. This decision was based on the signal coming from the main detectors (provided that the information could be processed within the allotted time) as well as from the response of a collection of scintillator counters located within the spectrometer. These counters, listed below, were connected to very fast electronics to achieve a fast response to a given event.

A0 & A1: Located between the radiator and the target. These counters signaled that the beam contained charged particles. This was a possibility if photon conversion occurred after the radiator and the sweeping magnets.

TR1: Located between the last TSSD plane and the first SSD plane. This counter signaled that an interaction with at least one charged particle had occurred in the target.

TR2: Located after the last SSD plane. Shown in Figure II.7 as Trigger 2, consisted of four counters arranged in quadrant. A signal coming out of any of the four counters indicated that a charged particle passed within the acceptance of M1. TR2 in coincidence with TR1 was a good indicator that a charged particle had passed through the SSD planes.

TM1 & TM2: Two halves of a single hodoscope located immediately in front of the target hut. TM1 and TM2 were used to veto on halo muons.

AM & AMD: These two hodoscope arrays were located upstream of the target surrounding the beam. A coincidence signal between these two detectors indicated the presence of halo muons. These arrays were used as veto counters.

H×V: This array consisted of 36 counters located between C3 and the IE. Two possible trigger signals, $(H \times V)_1$) and $(H \times V)_2$) indicated that at least one or two, separate,

charged particles had passed through the array. This array had a vertical gap to avoid triggering on e^+e^- pairs.

OH: This array consisted of 24 counters positioned just upstream of the OE for triggering events with low momentum/high angle particles. The array had an aperture that matches the aperture of M2 and a vertical gap in the center to avoid electron–positron pairs. The signal from the OH array, known as OH_1, corresponded to at least one charge particle passing through the array.

IM1 & IM2: These arrays were located within the IMU. IM1 consisted of two perpendicular planes, IM1H and IM1V. IM1 was positioned downstream of MH2, while IM2 was located upstream of MH3. Signals in these arrays indicated the passage of charged particles through the muon system.

In addition to the signals from the trigger hodoscopes, the FOCUS trigger used information gathered from the main detectors in the the trigger decision. For the IE, the channels were arranged into groups of 9 based on the transverse energy. Then, the sum of the total IE energy, E_{IE}, and the sum of the transverse energy, $E_{T(\text{IE})}$, were formed. For the HC, the signals from the phototubes were summed and integrated. If the sum was greater than 20 GeV then the hadronic trigger was set.

The Master Gate or first level trigger, was designed to reject electron pairs in favor of hadronic events. This step was crucial since the pair production cross section is 500 times larger than the hadronic production cross section. The main signals used in the triggers were the following:

TR1: An interaction occurred in the target region.

TR2: One particle passed through the SSD planes.

OH_1: At least on particle in the outer region.

$(H \times V)_1$: At least one particle in the inner region.

55

(a) H×V

(b) OH

(c) IM1

(d) IM2
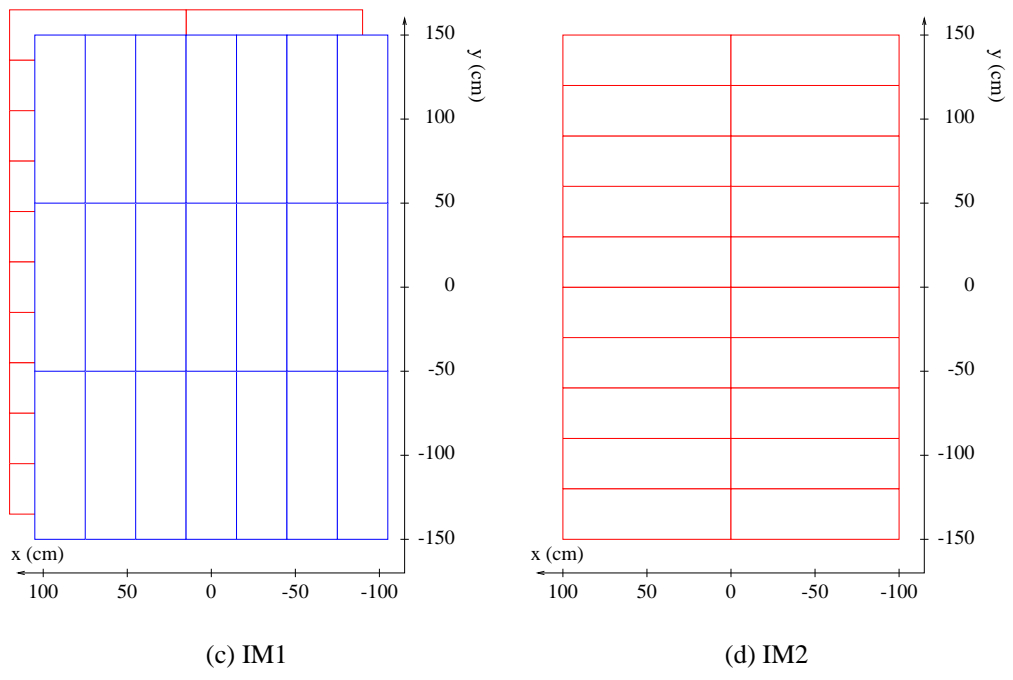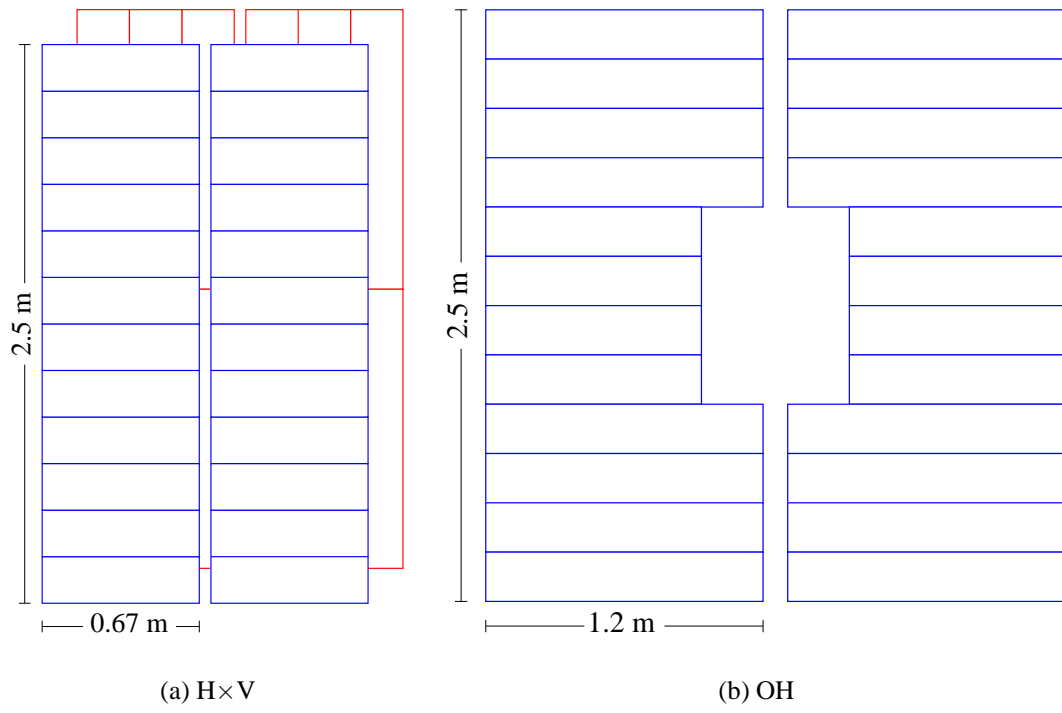
Figure II.16: Trigger hodoscope arrays.

$(H \times V)_2$: At least two particle in the inner region.

E_{HI}: Sum of hadronic energy over a high threshold.

E_{LO}: Sum of hadronic energy over a lower threshold.

E_{IE}: Sum of electromagnetic energy.

IE_2: At least two hits in the IE.

$E_{T(IE)}$: Sum of transverse energy in IE.

IM_1: At least one hit in the inner muon counters.

IM_2: At least two hits in the inner muon counters.

OM_1: At least one hit in the outer muon counters.

OM_2: At least two hits in the outer muon counters.

The main hadronic first level trigger was defined as

$$MG = TR1 \cdot TR2 \cdot [(H \times V)_2 + ((H \times V)_1 \cdot OH)] \cdot E_{HI} \qquad (II.6)$$

where the " $+$ " is logical OR and " $\cdot$ " is logical AND. This trigger required two charged particles passing through the SSD planes with two distinct signals in the H×V or signals in both the H×V and OH arrays. Along with the signals in the trigger hodoscopes, the MG also required a minimum amount of energy deposited in the HC. A semimuonic trigger was defined as

$$MG_{\text{semi-muonic}} = TR1 \cdot TR2 \cdot [IM_1 + OM_1] \cdot E_{LO}. \qquad (II.7)$$

A complete list of triggers can be seen in Table II.5. In the table the symbol $2B$, indicating the presence of at least two charged particles, is defined as $2B \equiv (H \times V)_2 + ((H \times V)_1 \cdot OH)$.

The decision of whether to pass an event to the second level trigger took around 200 ns, while the time required for a decision by the second level trigger was 1.2μs. If the second

Table II.5: Master Gate triggers used by FOCUS to collect data.

Trigger	Definition	Signal
MG1	$TR1 \cdot TR2 \cdot \mathbf{2B} \cdot \mathbf{E_{HI}}$	Main Hadronic Trigger
MG2	$TR1 \cdot TR2 \cdot \mathbf{2B} \cdot \mathbf{IE_2}$	$J/\psi \to e^+ e^-$
MG3	$TR1 \cdot TR2 \cdot [IM_1 + OM_1] \cdot \mathbf{E_{LO}}$	Semi–muonic decays
MG4	$TR1 \cdot TR2 \cdot \mathbf{2B} \cdot [IM_2 + OM_2 + IM_1 \cdot OM_1]$	$J/\psi \to \mu^+ \mu^-$
MG5	$TR1 \cdot TR2$	Prescaled $e^+ e^-$
MG6	$TR1 \cdot TR2 \cdot \mathbf{2B}$	Prescaled two–body
MG7	$TR1 \cdot TR2 \cdot [IM_1 + OM_1]$	Prescaled One–muon

level trigger was set the event was read out; this process required at least 10 μs. Otherwise, if the second level trigger failed a reset lasting 1μs cleared the readout electronics.

The second level trigger was designed to refine the rejection of electron pairs and to distinguish charm from light quarks events. The main requirement was the presence of multiple charged particles outside the pair region. In addition to the information out of the Master Gate triggers, the second level trigger used new information that was not available at the time the MG triggers fired. This new information is listed below. The set of typical second level triggers are listed in Table II.6.

$MULT_n$: Enough hits to form at least n tracks in the PWC.

AM·AMD: Veto on halo muons.

IM(E+W): Exclude hits in both halves of IM triggers.

$\mathbf{E_{IE\text{-}2}}$: Refined electromagnetic energy sum.

II.3 Monte Carlo Simulation

The FOCUS Monte Carlo simulation (ROGUE) utilizes Pythia (version 6.127) [30] to simulate the production of charmed events. Pythia takes as input a random photon energy corresponding to FOCUS beam energies and outputs a list of particles and their four–momenta after interacting with a target nucleon via photon–gluon fusion. If a charmed

Table II.6: Typical second level triggers used by FOCUS.

Trigger	Definition	Signal
TRIG1	MG1·E_{IE-2}·MULT4	Hadronic Trigger
TRIG2	MG2·$(H \times V)_2$ · E_{IE-2}	$J/\psi \rightarrow e^+ e^-$
TRIG4	MG4·IM_2 · $(H \times V)_2$·!$(AM \cdot AMD)$	J/ψ, inner
TRIG5	MG5	Prescaled MG5
TRIG6	MG6	Prescaled MG6
TRIG8	MG1	Prescaled MG1
TRIG9	MG4·OH·OM_2·MULT2·!$(AM \cdot AMD)$	J/ψ, outer
TRIG11	MG4·IM_1·OM_1·MULT1·$(H \times V)_1$·IM(E+W)	J/ψ, inner/outer

event is generated the output particles are decayed and traced through a simulation of the FOCUS spectrometer. As the decayed particles are traced through the spectrometer, the response from the different detectors are simulated and stored. This information is later used to reconstruct the events using the same algorithms as for real data.

Parameters like lifetime, branching fraction, etc., are used in the simulation of the events. ROGUE also utilizes the decay matrix elements of the decays when known. If the decay matrix element is not known, ROGUE simulates the event using a matrix element uniform in phase–space.

Many parameters in the simulation can be tuned in order to have a faithful representation of the particle production mechanism, detector response, and backgrounds. The tuning of these parameters has extensively been studied and implemented by the FOCUS collaboration leading to very good agreement between data and Monte Carlo for most observables.

ROGUE provides the option of generating generic $c\bar{c}$ Monte Carlo, where all known charm species are generated with their corresponding properties, as well as a specific decay chain. When choosing the later, Rogue generates the event with the specific decay chain in either the charm or its anti–charm mode on one side and decays the oppositely charmed particle following the hadronization process as simulated by Pythia. Large samples of signal and known charmed background events can be generated in a rapid way

by specifying the desired decay channels. Furthermore, when specifying a given decay channel, the number of events generated for that channel is known. This number is needed to calculate the reconstruction efficiency of said channel.

In order to limit the statistical uncertainty of the Monte Carlo sample, it is recommended to generate at least an order of magnitude more Monte Carlo events than data produced in the experiment. For this analysis, we generated $\sim 80 \times 10^6$ and $\sim 30 \times 10^6$ $D^+ \to \rho^0 \mu^+ \nu$ and $D^+ \to \overline{K}^{*0} \mu^+ \nu$ events, respectively. The $D^+ \to \rho^0 \mu^+ \nu$ decay was generated using both a flat phase–space and with a matrix element similar to the one measured for $D^+ \to \overline{K}^{*0} \mu^+ \nu$, in which the pole masses were changed to reflect the $c \to d$ transition present in the decay. This choice does not change the shape of $M(\pi^+ \pi^-)$ used to fit the data.

Another 10×10^6 events were generated for each known background. A sample of $\sim 800 \times 10^6$ $c\overline{c}$ Monte Carlo events were also generated.

CHAPTER III

DATA RECONSTRUCTION

During the data taking period FOCUS recorded over 6.5 billion photon interactions. The electronic signals coming out of the detectors for particles that went through the spectrometer had to be converted to physical quantities before the data analysis began. During this process hits were converted into tracks, vertices were formed, particles were identified, etc. Once reconstructed, events were sorted based on broad physical characteristics for further processing.

III.1 Reconstruction Algorithms

In this section a brief description of the track, vertex, and Čerenkov reconstruction algorithm is presented. We begin by discussing the track reconstruction from hits found in the tracker elements. Once the tracks are reconstructed the search for vertices can begin. After finding the decay vertices we need to be able to identify the charged particles that are emerging from the decay vertex if we wish to reconstruct the decay process. For this we need to convert the Čerenkov light collected in the Čerenkov detectors into a determination of which particle is most likely responsible for such a light pattern.

III.1.1 Track Reconstruction

FOCUS used both the SSD and PWC tracking systems to form tracks. Tracks in each system were, to some extent, reconstructed independently of one another and then linked together. Linking is the process of relating a SSD track with a PWC track.

SSD Tracks

Finding tracks in the SSD begins by making a very conservative analysis of the valid hits based on the charge released. This reduced the number of clusters of adjacent hits when they were consistent with a number of minimum ionization particles (MIP) crossing lower than the number of clusters and improved the resolution by charge interpolation. The resulting clusters were used to form projections of hits in each of the three views. In order to form a projection for a given view, the view must contain hits in at least three of the four stations. Hits were allowed to be shared among the resulting tracks except for those on the last three stations for tracks with hits in all four stations.

Once the projection for a given view was found, the projection was tested against the hypothesis that it formed a straight line by fitting it with a first order polynomial. Only those projections with $\chi^2/\mathrm{DOF} < 3$ were kept.

In order to form tracks, projections for all three views were combined and accepted as tracks if they matched in space with $\chi^2/\mathrm{DOF} < 8$. Tracks with shared projections were arbitrated based on the lowest χ^2/DOF. If more than one track had nearly identical track parameters, the tracks were collapsed into a single track. Hits not used in any track were then used to search for wide angle tracks and single segments of multiple Coulomb scattered tracks.

TSSD Hit Reconstruction

The SSD tracks parameters were improved by adding the information from the Target Silicon Detector (TSSD) [26]. As a first step, the SSD tracks were refitted taking into consideration the multiple Coulomb scattering in the determination of their parameters. The refitted SSD track was then extrapolated to the most downstream of the TSSD planes and a 3σ search radius was used to search for hits. This search was restricted to no more than ± 40 strips. The closest hit to the extrapolated SSD track was used as a seed to determine the number of adjacent hits. The adjacent hit with the largest signal and the

resulting seed were then weighted to determined the centroid. The track is then refitted at the most downstream of the TSSD planes. Once the refit at the most downstream planes was done, the track was extrapolated to the upstream planes and the process was repeated.

Once the refit process was completed, the most likely production vertex was calculated via (III.3) (see Section III.1.2) using only the SSD tracks. If the production vertex was located upstream of any of the TSSD planes, the SSD track was replaced with the track refitted with the TSSD information.

PWC Tracks

The algorithm used to find PWC tracks is similar to the one used to find SSD tracks. The main difference is that instead of independently finding the projections for all four views (x, y, u, and v), the x–view projection was found by extrapolating the x–component of SSD tracks onto P0. The x–view was chosen because it is the direction least affected by the magnetic kick. Because of this extrapolation, it was required that the x–projection had hits in P0. The projections for the other three views were formed independently.

The resulting x–projections were combined with all other views to form tracks. The tracks were fitted using a least square fit to determine the track parameters, the slope and intercept in x and y. For tracks passing through M2, the change in slope in the y view was also a fit parameter.

Low momentum tracks that do not pass through M2, called stubs, were recovered by combining unused hits in the x–view of P0 and P1 with projections in the other views. Tracks with hits only in P0 were required to have hits in all four views; tracks that extend through P1 were required to have hits in at least three of the four views in each station.

Linking SSD and PWC Tracks

Linking refers to the association of SSD tracks with PWC tracks. This was done by extrapolating SSD tracks and PWC tracks to the center of M1 where the slope and intercepts

were checked for consistency. A global least square fit was performed using both SSD and PWC hits to check if the tracks were consistent with coming from the same particle. Arbitration between possible track candidates was based on the lowest χ^2/DOF.

Momentum Determination

The momenta of the tracks was determined by the measuring the slope of the track before and after the magnets. For 5–chamber tracks, the PWC information from both sides of M2 was used to determined the momentum. A fit to the track parameters, including the change in the slope was performed, returning the track's momentum and improved track parameters. The momenta of stubs and four–chamber tracks was determined using the SSD information along with the PWC information between M1 and M2 based on the deflection in M1. The momentum resolution as measured in M1 is approximately

$$\frac{\sigma}{p} = 3.4\% \left(\frac{p}{100\text{GeV}}\right) \sqrt{1 + \left(\frac{17\text{GeV}}{p}\right)^2} \qquad \text{(III.1)}$$

and for M2 is

$$\frac{\sigma}{p} = 1.4\% \left(\frac{p}{100\text{GeV}}\right) \sqrt{1 + \left(\frac{23\text{GeV}}{p}\right)^2}. \qquad \text{(III.2)}$$

At low momentum, the resolution is dominated by multiple Coulomb scattering, while the position resolution of the PWC system dominates at high momentum.

III.1.2 Vertex Reconstruction

Finding displaced vertices is essential in the reconstruction of charm decays. A rough estimate of the vertex positions can initially be obtained by assuming that all tracks in the event originate from the same vertex. This hypothesis was tested by minimizing the

transverse distance of closest approach via the χ^2 equation

$$\chi^2 = \sum_{i=1}^{n} \left(\frac{x - (x_i + x_i'z)^2}{\sigma_{x,i}} \right)^2 + \left(\frac{y - (y_i + y_i'z)^2}{\sigma_{y,i}} \right)^2 \tag{III.3}$$

where x, y, and z are the fit parameters, x_i, x_i', y_i, and y_i' are the parameters of the ith track, and the σ represent the errors on the track parameters. If the χ^2/DOF was greater than 3, the track contributing the most to the χ^2/DOF was removed. This process was repeated until $\chi^2/\mathrm{DOF} < 3$ for the given vertex. The removed tracks were then used to form other vertices until no tracks were left or no more vertices could be found.

For most analysis, including the analysis discussed here, FOCUS uses a "candidate driven" algorithm, known as DVERT, to find secondary vertices. The algorithm works by assuming that the reconstructed final state particles form a decay (secondary) vertex. The resulting vertex was required to have a confidence level (CL$_{\mathrm{sec}}$) greater than certain threshold, usually 1%, for the vertex to be kept. Once a good secondary vertex was found, the search for the production (primary) vertex could begin.

The primary vertex finder to be used depended on whether all final state particles were reconstructed (e.g., $D^+ \rightarrow K^-\pi^+\pi^+$), or one or more final state particles were missing (e.g., semileptonic decays). For a fully reconstructed charmed decay, FOCUS uses DVNUCL. The DVNUCL algorithm begins by taking the secondary vertex and projecting back towards the target along the D momentum vector. All unused tracks that intersected this line were then used to try to form the highest multiplicity vertex possible. The resulting primary vertex was required to have a confidence level (CL$_{\mathrm{prim}}$) greater than 1%. Once the production vertex had been found, the separation between the production and decay vertex, L, was calculated along with the error associated with it, σ_L.

For semileptonic decays, where the final state neutrino escapes detection, the primary vertex algorithm, known as DVFREE, begins by combining two unused tracks into a vertex. Tracks were added one by one into the vertex until the confidence level of the resulting

vertex was less than 1%. The process was then repeated beginning with a track that had not been previously assigned to a vertex and continued until all tracks had been used and were either in at least one vertex or no more vertices could be formed. Notice that tracks could be shared among vertices. Once the list of primary vertices candidates was found, the highest multiplicity vertex was selected as the event primary vertex. Ties were broken by selecting the most upstream vertex.

III.1.3 Particle Identification Algorithm

FOCUS used three Čerenkov detectors (see Section II.2.7) operating in threshold mode to identify charged particles passing through the spectrometer. The standard method for charged particle identification using threshold Čerenkov detectors yields a TRUE or FALSE answer to the question of whether the track is consistent with a given identification hypothesis. This decision is made based solely on the ON/OFF status of the Čerenkov detectors and the momentum of the track. This method is hindered by the accidental firing within a counter since the counter is declared ON if any of the cells within the track's Čerenkov cone fired.

FOCUS incorporated the accidental firing rate in its Čerenkov algorithm known as CITADL [31] (Čerenkov Identification of Tracks by an Algorithm using Digital Likelihood) to improve the particle identification. Instead of returning a TRUE or FALSE answer CITADL returned the relative likelihood that the track had a Čerenkov pattern consistent with a given particle identification hypothesis. The advantages of this approach are twofold: first, the discrimination among identification hypotheses is extended over the threshold momentum ranges and secondly, the particle identification variable becomes a continuous variable instead of TRUE/FALSE.

The likelihood was formed based on the firing probability of all Čerenkov cells within the track's Čerenkov cone, $\beta = 1$, including the accidental firing rate. For a cell that fired, the log likelihood was increased by $\log(1 - \exp(-\mu))$, where μ is the number of

photo-electrons expected for a given hypotheses; if the cell did not fire, the likelihood was increased by $\log(\exp(-\mu))$. The variable returned by CITADL is a χ^2 like variable, W_i, defined as

$$W_i = -2 \sum_{j}^{\text{cells}} \log P_j \qquad \text{(III.4)}$$

where P_j is the firing probability of the jth cell. This variable was calculated for all four particle hypothesis, electron, pion, Kaon, and proton.

The accidental rate was included in CITADL by measuring the firing rate of cells outside of the track's Čerenkov cone. It was found that the accidental rate was often proportional to the beam intensity, particularly near the beam axis, making the noise for central cells rather large.

Armed with the log likelihoods for all four particle identification possibilities, a comparison between two hypothesis can be made. For example, a track with $W_K - W_\pi > 0$ is more likely to be a pion than a Kaon. The variable $W_K - W_\pi$ is known as pionicity. In Figure III.1, the kaonicity variable, $W_\pi - W_K$, is shown. The clear separation between the Kaon and pion hypothesis makes this variable very useful for particle identification.

III.1.4 Muon Identification

High momentum muons were identified in the IMU consisting of three stations, each with two views, of scintillating material (see Section II.2.9). As a first step, reconstructed tracks were projected onto the IMU. Hits were then searched within a $3\sigma_{\text{mcs}}$ radius of the projected track, where σ_{mcs} is the width of the Multiple Coulomb Scattering distribution. Once the hits were found, the χ^2 of the hypothesis that the projected track passed through the reconstructed hits within its anticipated errors was calculated. The candidate track was required to have hits in at least four of the six planes. The calculation of the χ^2 took into account both the multiple Coulomb scattering and the granularity of the detector. The muon identification was based on the confidence level, defined as the probability of obtaining a
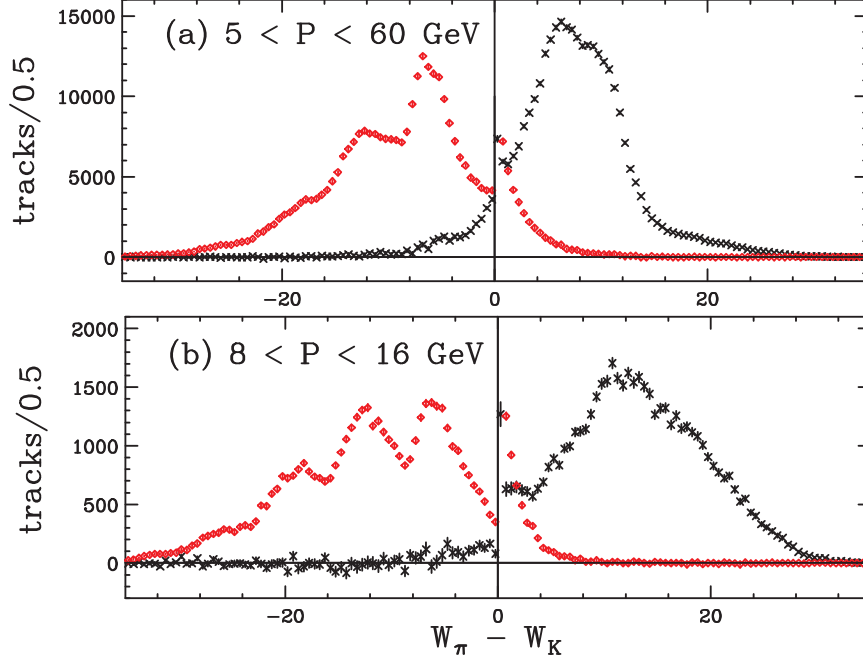
Figure III.1: Log likelihood difference $W_\pi - W_K$ for Kaons (black) and pions (red) for background subtracted Golden Mode charmed events. Taken from Reference [31].

χ^2 equal or greater than the calculated χ^2 for the track, for the hypothesis that the track was the result of a muon passing through the detector.

Low momentum tracks have larger σ_{mcs}. This increases the probability of including spurious hits as well as hits left from nearby tracks. This was minimized by requiring a smaller search radius for low momentum tracks. For tracks with momentum less than 10 GeV/c the minimum number of planes hit was reduced to two. For these tracks a search radius of $2\sigma_{mcs}$ was used and the confidence level calculated. If the confidence level was less than 1%, the search was redone using a search radius of $1\sigma_{mcs}$.

The efficiency of the muon identification algorithm was greater than 98% for tracks with momenta greater than 10 GeV/c. The greatest contribution to the muon misidentification rate came from in–flight decaying pions.

The algorithm to identify low momentum tracks passing through the OMU is similar. The main difference is that M2 was the filter used for the OMU. Thus, the magnetic deflection in the filter was taken into account when projecting the tracks.

68

In order to reduce the muon misidentification background, the final data set contains only events with muons interacting in the IMU detector.

III.1.5 Calorimetry Reconstruction

The electromagnetic (IE, OE) and hadron (HC) calorimeters were used to reconstruct photons and neutral hadrons. The first step in reconstructing the energy deposited in the IE was to find the energy of each block by converting the ADC (analog–to–digital converter) counts into energy values. Each block had its own conversion value which changed over time. After the pedestal subtraction, each ADC count was equivalent $10\,\mathrm{MeV}$ of deposited energy. After reconstructing the energy of the individual blocks, the highest energy block was identified and it was clustered with the surrounding eight blocks. This clustering of blocks was repeated until all possible clusters were found.

An estimate of the position of a cluster was found after performing a weighted average of the energy given by

$$x_c = \frac{\sum_i E_i x_i}{\sum_i E_i}$$

where x_c is the x–position of the cluster and E_i and x_i are the energy and x–position of the ith block. The same calculation was performed for the y–position. An improved position of the cluster was be obtained via [32]

$$x'_c = 0.76 \sinh^{-1}\left[\frac{(x_c - x_b)}{S/2} \sinh\left(\frac{S/2}{0.76}\right)\right] + x_b$$

where x_b is the position of the center of the central block. The same calculation was used for the y'_c. This position was further corrected for systematic effects using a six order polynomial.

Once all the clusters were found, the PWC tracks were projected onto the IE and those tracks within 6 cm of a cluster center were assigned to that cluster. Clusters not matched to any PWC track were identified as neutral clusters.

The OE showers were reconstructed after first identifying the energy clusters. Clusters associated with reconstructed charged tracks were tagged; the remaining clusters were assigned to neutral showers. The energy of the cluster was found after converting the ADC counts for each counter into an energy value and summing over the cluster. The weighted center–of–energy position determined the position of the cluster after correcting for systematics.

Since about 80% of hadrons passing through the IE undergo a hadronic interaction, neutral hadrons were identified by matching neutral clusters in the IE with clusters in the HC. The total energy of the hadron was then the sum of the energy deposited in the IE and HC. The energy deposited by charged hadronic tracks by projecting the tracks onto the HC. Towers within 1 interaction length radius from the front of the impact point in front of the HC were then identified and their energy summed.

Other than the trigger requirements applied to our data, no calorimeter information was used in this analysis.

III.2 **Cut Descriptions**

One of the most important aspects of any analysis is finding the correct set of cuts that is able to differentiate between signal and background processes. The main characteristic of a charmed event is its large separation between the production and decay vertices. Therefore, it is imperative to have access to variables that can exploit this detachment. Before the separation between the production and decay vertices can be used, the final state particles need to be identified and assigned to either of the vertices. With these needs in mind, the variables used in this analysis can be separated into two main categories: vertexing variables and particle identification variables. In this section, I give a description of the most important variables used throughout this analysis.

L$/\sigma$ Distance between the primary and secondary vertex (L) divided by its error (σ). L/σ is one of the most important cuts used to discriminate against non–charmed events.

70

Confidence Level (CL) In FOCUS the confidence level is defined as the probability of obtaining a χ^2 smaller than the observed χ^2 for a given hypothesis. As an example, consider the hypothesis that a group of tracks originate from a common vertex. If the hypothesis is true, the CL will take any value from 0 to 1 (mostly a flat distribution). If the hypothesis fails, the CL will be a value close to 0. Therefore, by defining good vertices as those exceeding a CL threshold α (usually 1%), we are effectively rejecting most events where the tracks do not originate from a common vertex while keeping good vertices with an efficiency of $1 - \alpha$.

In this analysis a CL cut is mainly used in testing the hypothesis of tracks forming good vertices (both primary and secondary) and in the identification of muons.

Secondary vertex isolation (Iso2) The secondary vertex isolation cut refers to the highest CL that a track not assigned to the primary or secondary vertex belongs to the secondary vertex. The smaller the value for this variable the more likely it is that the secondary vertex formed has no other tracks associated to it. This cut is useful in rejecting high multiplicity events.

Primary vertex isolation (Iso1) The primary vertex isolation cut refers to the highest CL for the hypothesis that any track assigned to the secondary vertex belongs to the primary vertex. This variable was obtained by adding one by one the tracks in secondary vertex to the primary vertex. The highest CL is returned. The smaller the value for this variable the more likely it is that no tracks assigned to the secondary vertex should be assigned to the primary vertex.

Vertex In/Out of target This variable refers to the significance of the location of a vertex (primary or secondary) with respect to the target material. Primary vertices are usually required to be located inside the target, while secondary vertices are required to be located outside of the target material.

Pion Consistency CITADL variable for pion identification defined as $W_{\text{best}} - W_\pi$. This variable compares the pion hypothesis with the other possible identification hypotheses. A typical requirement is that no identification hypothesis is favored over the pion hypothesis by more than 7 units of likelihood.

pionicity/Kaonicity CITADL variable used to compare the pion identification hypothesis to the Kaon identification hypothesis. It is defined as $W_K - W_\pi$. A positive pionicity value means that the pion hypothesis is favored over the Kaon hypothesis. The converse, $W_\pi - W_K$, is defined as Kaonicity.

III.3 Data Reduction

FOCUS wrote about 6000 8 mm tapes containing raw data coming out of the data acquisition systems. Before any physics analysis began, the data was converted into physical objects. The general reconstruction and sorting of the data was done in three phases, Pass One, Skim One, and Skim Two. During Pass One the general reconstruction was applied, while during Skim One and Skim Two the events were sorted into smaller data sets.

III.3.1 Pass One

The reconstruction of the data recorded by FOCUS began with Pass One. During Pass One all the reconstruction algorithms were run on the data. Events with clear reconstruction errors, such as events with no reconstructed tracks, were discarded at this stage. The reconstruction effort took around ten months to be completed using Fermilab's computing farms. The output was written onto approximately 6000 8 mm data tapes.

III.3.2 Skim One

After the Pass One reconstruction was completed at Fermilab, the output tapes were shipped to the University of Colorado and Vanderbilt University for Skim One. Skim One

was the first general effort to sort the data according to the physics process involved. Six super–streams, containing summarized rather than the full information from Pass One, were created. Each super–stream contains one or two broad physical characteristics.

To avoid cutting away too many events in the early stages of data analysis the selection criteria used in Skim One were very loose. For example, an event with a muon, defined as a track with momentum greater than 8 GeV/c and muon confidence level greater than 0.1%, was assigned to super–stream one (SS1). Around 50% of Pass One events passed Skim One. Many of the events were written into more than one super–stream. The six super–streams used to sort the data are shown in Table III.1.

Table III.1: Skim One Super-streams.

Super-stream	Description	Approx. # of Tapes	Skim2 Institution
SS1	Semileptonic ans Dileptons	330	UPR Mayagüez
SS2	Global Vertex and K_s	552	U. of Illinois
SS3	EM and ϕ	360	Brazil, CPBF
SS4	Baryons	426	Fermilab
SS5	Diffractive, Leptonic and Out of Target	480	U. of California
SS6	SEZDEE	294	U. of California

III.3.3 **Skim Two**

Skim Two was the last skim process applied to all the data collected during the FOCUS experiment. In this skim, each super-stream was divided into even smaller data sets, each of which contain events of a very specific processes. The responsibility for Skim Two was shared among the institutions that form the FOCUS collaboration as listed in the last column of Table III.1.

The data for the analysis presented in this thesis was taken from the Slepnrm sub–stream of SS1 (see Table III.2). The Slepnrm sub–stream required at least two charged tracks in an event. For semimuonic events, the muon track was required to have a muon confidence level greater than 0.01%; the hadron track was required to have $W_\pi - W_K > 1$ for the track to be identified as a Kaon, or that no particle hypothesis was favored over the

pion hypothesis by more than 7 units of likelihood (pion consistency) for the track to be identified as pion. The muon and hadron tracks were required to form a good vertex with confidence level greater than 0.01%.

Table III.2: SS1 sub-streams.

SS1 Sub-stream	Description	Num. of Tapes
1	Semimuonic	26
2	Dileptonic and PPbar	45
3	Semielectronic with mesons	37
4	Semielectronic with baryons	27
5	Normalization (Slepnrm)	58

CHAPTER IV

DATA SELECTION AND ANALYSIS

The ρ^0 is a resonant particle that decays strongly into two pions. Therefore, in order to reconstruct the $D^+ \to \rho^0 \mu^+ \nu$ decay we searched for two oppositely–charged pions along with a muon forming a good secondary vertex. The secondary vertex was required to be significantly detached from the primary vertex in order to discriminate against non–charm decays.

Many difficulties were inherent in this analysis. There were large backgrounds coming both from charm and non–charm sources that needed to be identified and minimized while at the same time maximizing our signal. Because some of the backgrounds are irreducible, the yield was extracted with a binned maximum log likelihood fit where the shapes of the signal and known backgrounds were used.

IV.1 Skim Three

The data used in this analysis comes from the Slepnrm subskim of SS1. This subset contains 58 8–mm tapes, each with approximately 4.5 GB of data. In order to facilitate the analysis of the data the Slepnrm subskim was subjected to another reduction called Skim Three. The main objective of Skim Three was to further reduce the data for final analysis by applying very loose cuts that have already been proven to work in reducing known backgrounds by other analyses within the collaboration. Furthermore, in Skim Three the data was separated according to the meson content of the secondary vertex.

In Skim Three an event was accepted if the secondary vertex contained a muon with either of the following meson combinations: two pions (ρ), two Kaons (ϕ), or a Kaon and a pion ($\overline{K}^{*0}$). Tracks with $W_\pi - W_K > 1$ (Kaonicity) were identified as Kaons while those tracks with $W_K - W_\pi > 0$ were identified as pions.

Tracks in the Inner Muon System were identified as muons if they had momentum greater than 10 GeV/c and a muon confidence level (CL_μ) greater than 0.005. Low momentum tracks in the IMU, with momentum between 6 and 10 GeV/c were identified as muons if the CL_μ was greater than 0.01. Tracks in the Outer Muon System were identified as muon if the momentum was greater than 4 GeV/c and CL_μ greater than 0.01.

The secondary vertex formed must be a good vertex with a confidence level (CL_{sec}) greater than 0.01. The highest multiplicity vertex formed after excluding all tracks used in the secondary vertex was selected as the primary vertex. If more than one candidate vertex had the same multiplicity, the most upstream candidate was selected. The separation between the primary vertex and the secondary vertex was required to have a significance exceeding five sigmas ($L/\sigma > 5$).

The Skim Three outputs were approximately 9 GB each for the $\pi\pi\mu$ and $K\pi\mu$ streams and 4 GB for the $KK\mu$ stream. The main advantage of reducing the Slepnrm data down to less than 4% of the original data size for each stream is that the computational time needed for final analysis was greatly minimized. This becomes especially important because any changes in the selection criteria (e.g., loosening a previously applied cut) requires running over the whole data set anew.

IV.2 Selection of $D^+ \rightarrow \rho^0 \mu^+ \nu$ Candidates

The $D^+ \rightarrow \rho^0 \mu^+ \nu$ candidates were selected from the $\pi\pi\mu$ stream of Skim Three. The Skim three data were subjected to further selection criteria in which most cuts were tightened to enhance the $\pi\pi\mu$ sample and where all variables needed for the analysis were calculated. The output of this analysis step was a PAW (Physics Analysis Workstation) [33] Ntuple. In an Ntuple, the values of the variables used for an analysis are stored for every accepted event. Once an Ntuple is created, cuts can be applied and changed interactively without having to recompile and run the analysis code again.

76

In addition to the Skim Three requirements, an event was accepted and written to the Ntuple if the conditions described below were satisfied.

We began by requiring all tracks to be singly linked (i.e., correspondence between the SSD track and PWC track). Any track consistent with being parallel to the beam was discarded in order to eliminate contamination from e^+e^- pairs. Muon candidates were required to have $p_\mu > 8$ and $\mathrm{CL}_\mu > 0.01$ for tracks inside the IMU and $p_\mu > 6$ and $\mathrm{CL}_\mu > 0.05$ for tracks inside the OMU. As in Skim three, the two oppositely charged pion tracks were required to have $W_\mathrm{K} - W_\pi > 0$.

The secondary vertex formed with the two pions and the muon must form a good secondary vertex with $\mathrm{CL}_\mathrm{sec} > 0.01$ and not be more than 5 sigmas inside the target. Once the secondary vertex was formed, the mass for the three charged tracks, $M(\pi^+\pi^-\mu^+)$, was calculated. This mass was required to be less than $2\ \mathrm{GeV}/c^2$. It was also required that the mass of the two pion system, $M(\pi^+\pi^-)$, be less than $1.5\ \mathrm{GeV}/c^2$.

Tracks not used in the secondary vertex were used to form candidate production vertices. Of these vertices, the one with the highest multiplicity was selected as the primary vertex; ties were broken by selecting the most upstream vertex. The production vertex was required to have a confidence level greater than 1% and be within 3σ of the target material.

It should be noted that at this stage most of the cuts were still very loose. The intention was to eliminate from the sample those combinations that were blatantly wrong. All these cuts were tightened interactively using PAW++ (PAW's graphical interface) in later stages of the analysis. In Figure IV.1, the mass of the $\pi^+\pi^-$ system is shown. In this plot only the cuts described above are used. As can be seen in the plot, the $D^+ \to \rho^0\mu^+\nu$ signal is buried under a large background.

During the course of this analysis, three major sources of backgrounds were identified. The first kind of background came from semileptonic decays with two opposite charged pions plus neutrals (i.e., γ's, π^0's, and η's) in the final state. If the neutral particle or its decay products are not reconstructed then a good secondary vertex with two oppositely
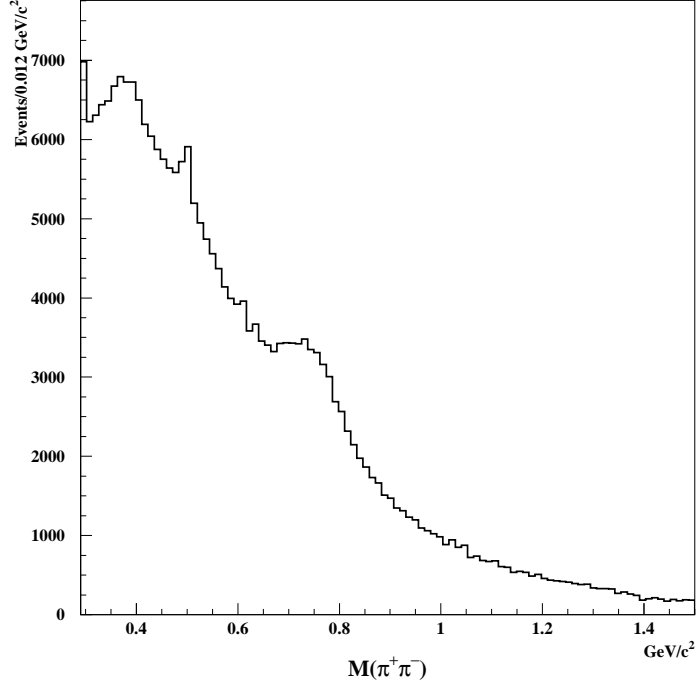
Figure IV.1: $M(\pi^+\pi^-)$ for events passing Skim Three and the loose selection criteria described in the text.

charged pions and a muon can be formed. More importantly, since the ρ is a very broad state with a width of 150 MeV/c^2, it is very likely that the mass of the background state will be reconstructed near or under the signal peak. These decays include $D_s^+ \rightarrow \eta'\mu^+\nu$ with η' following the decay chains $\eta' \rightarrow \rho^0\gamma$ and $\eta' \rightarrow \eta\pi\pi$ and $D_s^+ \rightarrow \eta\mu^+\nu$ with η decaying as $\eta \rightarrow \pi\pi\gamma$ and $\eta \rightarrow \pi\pi\pi^0$. The recently observed $D^+ \rightarrow \omega e^+\nu$ [34] also contributes to the background in its semimuonic mode since the ω can decay via $\omega \rightarrow \pi^+\pi^-$ and $\omega \rightarrow \pi^+\pi^-\pi^0$. The last semileptonic decay that enters in the background is $D^+ \rightarrow \overline{K}^{*0}\mu^+\nu$. In this case if the Kaon from the $\overline{K}^{*0}$ was be misidentified as a pion, it mimicked our signal resulting in a distribution very similar to that of the ρ^0 but with a mass peak slightly shifted towards the low mass end. Contributions from the Cabibbo suppressed decay $D_s^+ \rightarrow K^{*0}\mu^+\nu$, $D^+ \rightarrow \eta\mu^+\nu$, and $D^+ \rightarrow \eta'\mu^+\nu$ are negligible.
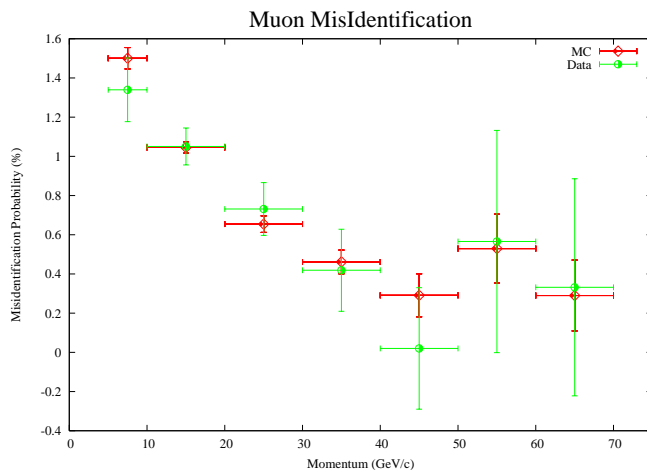
Figure IV.2: Muon misidentification probability as function of momentum for in–flight decaying pions for data (green) and Monte Carlo generated samples (red). The study was performed with samples of $K_s^0 \to \pi^+\pi^-$. The pions were required to pass typical cuts used for muon identification.

The second major source of background was due to muon misidentification. Most of the muon misidentification in this analysis is due to in–flight decaying pions. In this context the misidentification comes because we expect the muon to come from the secondary vertex not as a decay product of a hadron.

The muon misidentification probability can be calculated using both data and Monte Carlo. In FOCUS, a clean sample of $K_s^0 \to \pi^+\pi^-$ was used to determined how many pions were identified as muons. For this study, the pions were required to have $\text{CL}_\mu > 1\%$ and to have left hits in at least four of the six muon planes, typical cuts for the identification of muons. In Figure IV.2, the results of this study are shown. Although the muon misidentification probability in FOCUS is less than 1% over most of the momentum range, this background becomes significant when dealing with small signals such as those coming from Cabibbo suppressed decays like $D^+ \to \rho^0 \mu^+ \nu$.

The last major source of background was the combinatorial background. Combinatorial background arises when the algorithm tries to form a ρ^0 using two unrelated pions. Since

pions are very copious in the experiment, having random combinations that pass our final selection criteria is not rare.

Once the major contributions to the background are known, the process of finding the optimal cuts in order to extract the signal can begin. During this optimization process we looked for cuts that would minimize the backgrounds while at the same time keeping the most signal events possible as determined by a binned maximum log likelihood fit used to extract the signal yield. This fitting methodology is discussed in the next section.

IV.3 Fitting Technique

In order to extract the $D^+ \rightarrow \rho^0 \mu^+ \nu$ yield, the $M(\pi^+ \pi^-)$ data distribution was fit with a binned maximum log likelihood fit taking into account all the known backgrounds. Because the data sample contains some irreducible backgrounds along with the $D^+ \rightarrow \rho^0 \mu^+ \nu$ signal, the purpose of the fit is to give the best estimate of how much each source contributes to the number of events in each data histogram bin. In order to do this, we used a likelihood function based on Poisson statistics defined as:

$$\mathcal{L} = \prod_{i=1}^{\#\text{bins}} \frac{n_i^{s_i} e^{-n_i}}{s_i!} \times \text{penalty} \tag{IV.1}$$

where s_i is the number of events in bin i of the data histogram, n_i is the number of events in bin i of the fit histogram, and a penalty term, described below, is used to set a loose constraint on a known branching ratio.

Maximizing (IV.1) can be a very expensive in terms of computing resources, instead we minimized $-\log \mathcal{L}$. This is a much easier computational job since the product becomes a sum over the bins. The CERN package MINUIT [35] was used for the minimization and error determination.

The fit histogram is composed of binned, normalized shapes, shown in Figure IV.3, of

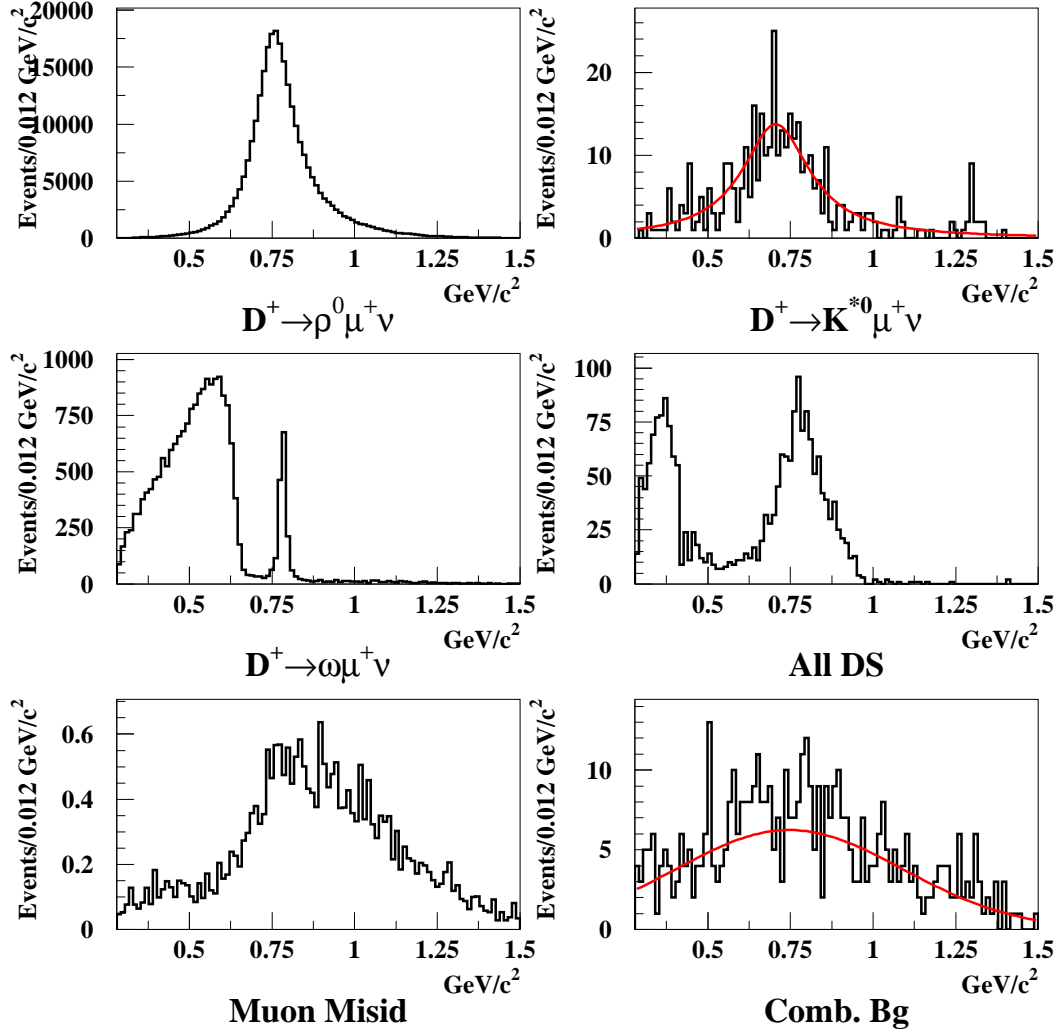signal and background components obtained both from Monte Carlo simulations and real data.

Figure IV.3: $M(\pi^+\pi^-)$ shapes used to fit the data. In order to get smoother shapes, the $D^+ \rightarrow \overline{K}^{*0}\mu^+\nu$ contribution and combinatorial background distributions have been fitted with a Breit Wigner and a broad Gaussian, respectively.

The number of events in each fit histogram bin is

$$n_i = Y_{D^+ \to \rho^0 \mu^+ \nu} S_{\rho^0 \mu^+ \nu} + \text{ECY}_{D^+ \to K^- \pi^+ \mu^+ \nu} \epsilon(K\pi\mu\nu \to \rho\mu\nu) S_{K\pi\mu\nu} +$$

$$Y_{D^+ \to K_S^0 \mu^+ \nu} S_{K_S^0 \mu^+ \nu} + Y_{D^+ \to \omega \mu^+ \nu} S_{\omega \mu^+ \nu} + Y_{D_s^+} S_{D_s^+} + Y_{\mathcal{C}} S_{\mathcal{C}} + Y_{\mathcal{M}} S_{\mathcal{M}} \qquad \text{(IV.2)}$$

where the terms in (IV.2) are explained in detail below. In general, S_x symbolizes the shape for a given source while the Y_x symbolizes its estimated contribution.

$Y_{D^+ \to \rho^0 \mu^+ \nu}$ is the yield of the $D^+ \to \rho^0 \mu^+ \nu$ signal. $\text{ECY}_{D^+ \to K^- \pi^+ \mu^+ \nu}$ is the efficiency-corrected yield (ECY) for $D^+ \to K^- \pi^+ \mu^+ \nu$. This quantity is the estimated number of $D^+ \to K^- \pi^+ \mu^+ \nu$ events produced by FOCUS. This, along with the Monte Carlo efficiency for a $D^+ \to K^- \pi^+ \mu^+ \nu$ event to be misidentified as a $D^+ \to \rho^0 \mu^+ \nu$ event, $\epsilon(K\pi\mu\nu \to \rho\mu\nu)$, provide an estimate of the amount of feed-down of this mode into our signal. The ECY is fixed in the fit to the value obtained from the $D^+ \to K^- \pi^+ \mu^+ \nu$ analysis used for the normalization mode (see Section IV.6). $Y_{D^+ \to K_S^0 \mu^+ \nu}$ is the yield of a small $K_S^0 \to \pi^+ \pi^-$ component.

$Y_{D^+ \to \omega \mu^+ \nu}$ is the yield of $D^+ \to \omega \mu^+ \nu$, where the ω could decay either to $\pi^+ \pi^- \pi^0$ or to $\pi^+ \pi^-$. We use the recent CLEO–c collaboration measurements of the absolute branching ratio of $D^+ \to \overline{K}^{*0} e^+ \nu$ and $D^+ \to \omega e^+ \nu$ [34] to set a loose constraint on the yield of $D^+ \to \omega \mu^+ \nu$. To this end, we add a penalty term to the likelihood of the form[1]

$$\exp\left[-\frac{1}{2} \left(R_{\omega/\overline{K}^{*0}} \epsilon_{\omega \mu^+ \nu} \times \text{ECY}_{D^+ \to \overline{K}^{*0} \mu^+ \nu} - Y_{D^+ \to \omega \mu^+ \nu} \right)^2 / \sigma^2_{D^+ \to \omega e \nu} \right] \qquad \text{(IV.3)}$$

where $R_{\omega/\overline{K}^{*0}} = \frac{\text{BR}(D^+ \to \omega e^+ \nu)}{\text{BR}(D^+ \to \overline{K}^{*0} e^+ \nu)}$ and $\epsilon_{\omega \mu^+ \nu}$ is the $D^+ \to \omega \mu^+ \nu$ reconstruction efficiency. The $\sigma_{D^+ \to \omega e \nu}$ error used in Eq. IV.3 is based on the errors in the branching fractions reported by CLEO-c with statistical and systematic errors added in quadrature to the error in the efficiency corrected yield for $D^+ \to \overline{K}^{*0} \mu^+ \nu$.

$Y_{D_s^+}$ is the combined yield of the modes $D_s^+ \to \eta' \mu^+ \nu$, $D_s^+ \to \eta \mu^+ \nu$, and $D_s^+ \to \phi \mu^+ \nu$

---

[1]Here we have assumed that the electronic and muonic rates are equal.

with η' decaying to either $\rho^0\gamma$ or to $\eta\pi^+\pi^-$, η decaying to either $\pi^+\pi^-\pi^0$ or to $\pi^+\pi^-\gamma$, and ϕ decaying to $\rho\pi$. This shape was obtained from a large $c\bar{c}$ Monte Carlo where all other decays were filtered out. The advantage of this method as opposed to generating every source individually, is that all the relative branching ratios are incorporated by default.

$Y_\mathcal{C}$ is the number of combinatorial background events where at least one of the three charged tracks forming the decay vertex does not belong to the vertex. After applying our selection criteria, this background is dominated by charm decays. In order to generate $S_\mathcal{C}$, the combinatorial background shape, we used a large Monte Carlo sample which simulated all known charm decays, in which, after an event was selected, the reconstructed tracks were matched against the generated tracks. If one of the reconstructed tracks did not belong to the generated decay vertex, the event was flagged as a combinatorial background event.

The last term of (IV.2), $Y_\mathcal{M}$, is the number of events due to muon–misidentification. The muon misidentification shape is also obtained from a large Monte Carlo sample where all known charm decays were simulated. In this case tracks within the acceptance of the inner muon system with a confidence level less than 1% and momentum greater than 10 GeV/c were taken as (fake) muons. This allowed us to use the same selection as in the analysis, but with very few real semi-muonic decays in the sample. This shape was then weighted with a momentum-dependent misidentification probability function to obtain the final shape used in the fit. The same technique, applied to a sub-sample of the FOCUS data, resulted in a shape in very good agreement with the shape used in the fit. The muon–misidentification shapes obtained from both data and Monte Carlo are shown in Figure IV.4. We chose not to use shape or $Y_\mathcal{M}$ estimates from the data due to the limited statistics available. Instead, we allowed $Y_\mathcal{M}$ to float freely in the fit.

As can be seen in Figure IV.3, some of the shapes used in the fit are not smooth after all the cuts are applied, even when large Monte Carlo samples were used. This is specially evident when looking at the K/π misidentification and combinatorial background shapes. In order to improve the $M(\pi^+\pi^-)$ fit, these shapes were parametrized. For the K/π
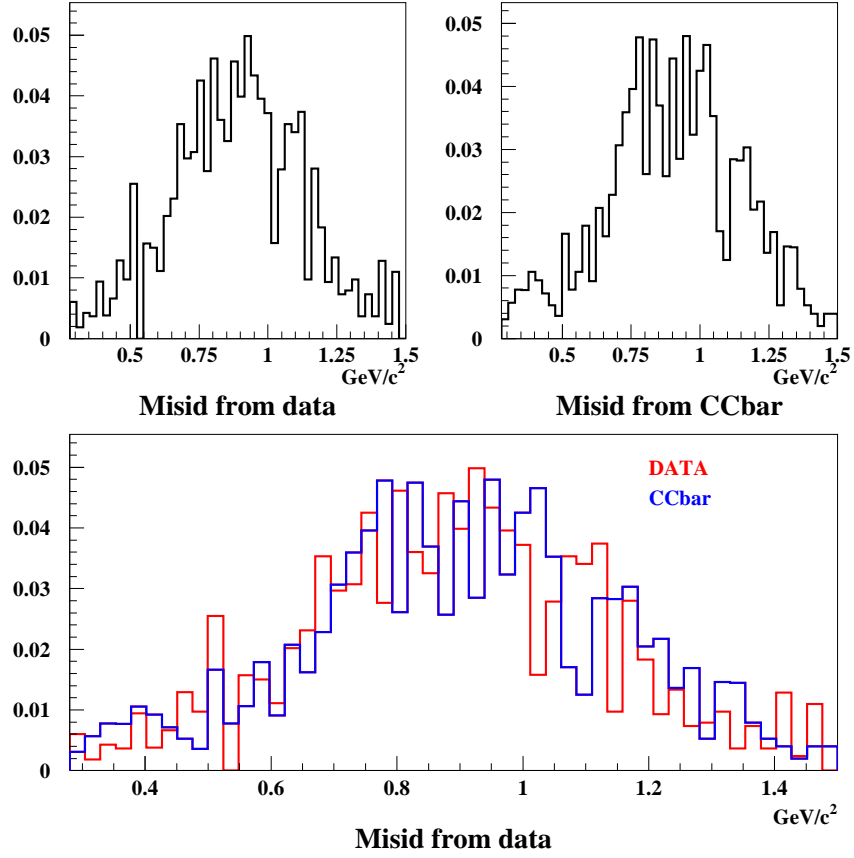
Figure IV.4: Muon–misidentification shape for data and Monte Carlo.

misidentification distribution, the parametrization was based on a Breit–Wigner function, while the combinatorial background was parametrized with a broad Gaussian.

IV.4 Branching Fraction Ratio

The branching fraction ratio $\frac{\Gamma(D^+ \to \rho^0 \mu^+ \nu)}{\Gamma(D^+ \to \overline{K}^{*0} \mu^+ \nu)}$ was calculated using

$$\frac{\Gamma(D^+ \to \rho^0 \mu^+ \nu)}{\Gamma(D^+ \to \overline{K}^{*0} \mu^+ \nu)} = \frac{Y_{D^+ \to \rho^0 \mu^+ \nu}/\epsilon_{D^+ \to \rho^0 \mu^+ \nu}}{Y_{D^+ \to K^- \pi^+ \mu^+ \nu}/\epsilon_{D^+ \to K^- \pi^+ \mu^+ \nu}} \times BR(\overline{K}^{*0} \to K^- \pi^+) \quad \text{(IV.4)}$$

where Y_x and ϵ_x are the yield and efficiency, respectively. The yields were extracted form the signal and normalization fits, while the efficiencies were calculated as

$$\epsilon = \frac{\text{Num. of accepted MC events}}{\text{Num. of generated MC events}}. \quad \text{(IV.5)}$$

Because we wish to calculate the $D^+ \to \rho^0 \mu^+ \nu$ branching fraction with respect to the $D^+ \to \overline{K}^{*0} \mu^+ \nu$ branching fraction, but we measure the number of resonant $D^+ \to K^- \pi^+ \mu^+ \nu$ events, we must use the $\overline{K}^{*0} \to K^- \pi^+$ branching ratio, $BR(\overline{K}^{*0} \to K^- \pi^+)$, to convert to $D^+ \to \overline{K}^{*0} \mu^+ \nu$. Furthermore, analyses by FOCUS of the $D^+ \to \overline{K}^{*0} \mu^+ \nu$ decay mode [21, 22] have shown that there is an s–wave interference present in the $D^+ \to K^- \pi^+ \mu^+ \nu$ spectrum that needs to be taken into consideration when calculating $\frac{\Gamma(D^+ \to \rho^0 \mu^+ \nu)}{\Gamma(D^+ \to \overline{K}^{*0} \mu^+ \nu)}$. This interference accounts for $(5.30 \pm 0.74^{+0.99}_{-0.96})\%$ of the $D^+ \to K^- \pi^+ \mu^+ \nu$ yield, therefore we correct our branching fraction ratio, (IV.4), accordingly. The corrected branching fraction ratio becomes

$$\frac{\Gamma(D^+ \to \rho^0 \mu^+ \nu)}{\Gamma(D^+ \to \overline{K}^{*0} \mu^+ \nu)} = \frac{Y_{D^+ \to \rho^0 \mu^+ \nu}/\epsilon_{D^+ \to \rho^0 \mu^+ \nu}}{Y_{D^+ \to K^- \pi^+ \mu^+ \nu}/\epsilon_{D^+ \to K^- \pi^+ \mu^+ \nu}} \frac{BR(\overline{K}^{*0} \to K^- \pi^+)}{1 - f_{\text{s–wave}}} \quad \text{(IV.6)}$$

where $f_{\text{s–wave}}$ is the fraction of the $D^+ \to K^- \pi^+ \mu^+ \nu$ in the s–wave configuration.

IV.5 Final Cut Selection

Finding the optimal cut requirements that will give us the best measurement of the $\frac{\Gamma(D^+ \to \rho^0 \mu^+ \nu)}{\Gamma(D^+ \to \overline{K}^{*0} \mu^+ \nu)}$ branching fraction began by establishing a basic set of cuts that favored the $D^+ \to \rho^0 \mu^+ \nu$ decay over the existing backgrounds. This baseline cut set, drawn from the experience gained from previous semileptonic analyses by FOCUS, is discussed below.

In addition to the cuts discussed in Section IV.2 the baseline cut set incorporated two very important mass cuts. The first cut was the requirement that the mass difference $M(\pi^+ \pi^- \mu^+) - M(\pi^- \mu^+)$ be greater than 0.20 GeV/c^2. This cut reduced the possible background that originates from the decay process $D^{*0} \to D^0(\pi^- \mu^+ \nu)\pi^+$ where the soft

pion from the D^{*0} decay is erroneously assigned to the secondary vertex. The effect of this cut can be seen in Figure IV.5. It is readily apparent from the figure that this cut is very effective in reducing this kind of background with very little loss of real $D^+ \rightarrow \rho^0 \mu^+ \nu$ events.

The second cut was to the mass of the three tracks assigned to the secondary vertex. In order to allow for the missing contribution to the mass by the undetected neutrino, the charged mass $M(\pi^+ \pi^- \mu^+)$ should be cut below the mass of the D^+ (1.87 GeV/c^2). Because a significant fraction of the background originates from high multiplicity decay channels where one or more final state particles go undetected, $M(\pi^+ \pi^- \mu^+)$ should also be bounded from below. The cut, shown in Figure IV.6, was set as $1.2 < M(\pi^+ \pi^- \mu^+) < 1.8$ GeV/c^2. As can be seen in the figure, this cut sacrifices a good part of the $D^+ \rightarrow \rho^0 \mu^+ \nu$ signal but is even more effective against high multiplicity backgrounds and the muon misidentification background. The effect of this cut on the data can be seen in Figure IV.7.

In addition to the mass cuts described above, the baseline cut set includes stronger identification requirements for the two pions and the muon in the secondary vertex, as well as harder vertexing cuts. These identification requirements are described next.

In order to get a cleaner sample, only muons form the IMU system were used in the analysis. These muons were required to have a momentum greater than 10 GeV/c^2 and to have left hits in at least five of the six muon planes. Only muons with CL_μ greater than 1% were accepted. In addition, the muon track must have consistent momentum as measured in M1 and M2 independently.

Pions were required to be pion consistent: no other identification hypothesis is favored over the pion hypothesis by more than five units of likelihood. In order to reduce the contamination from the Cabibbo favored decay $D^+ \rightarrow \overline{K}^{*0} \mu^+ \nu$ the pion with charge opposite to the muon was required to have $W_K - W_\pi$ greater than 1 unit of likelihood. This cut is applied only to this pion because in $D^+ \rightarrow \overline{K}^{*0}(K^- \pi^+) \mu^+ \nu$ the Kaon and muon are oppositely charged. Thus, requiring harder pion identification cuts reduces significantly the
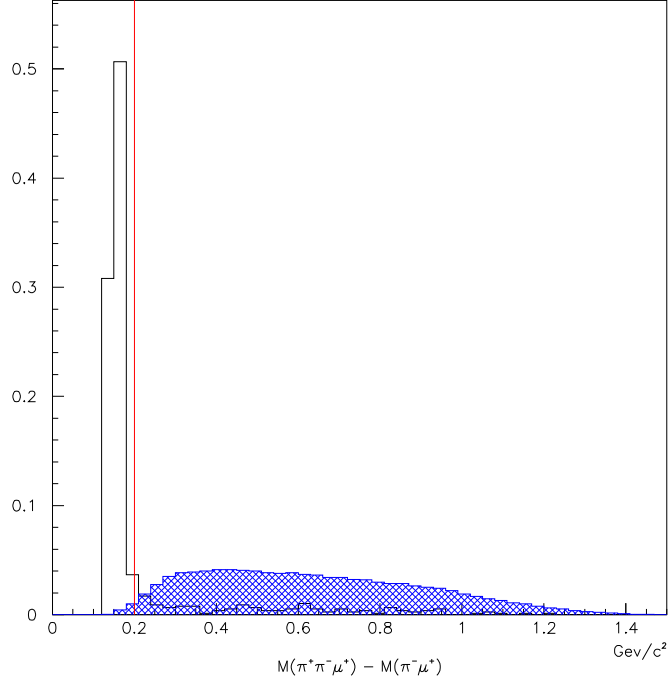
Figure IV.5: $M(\pi^+\pi^-\mu^+) - M(\pi^-\mu^+)$ mass cut. In this plot the effect of cutting on the mass difference $M(\pi^+\pi^-\mu^+) - M(\pi^-\mu^+)$ can be seen. Blue (hatched), $D^+ \rightarrow \rho^0\mu^+\nu$ simulated events. The solid histogram are simulated $D^{*0} \rightarrow D^0(\pi^-\mu^+\nu)\pi^+$ events. The red line indicates the value used to cut. Both distributions are normalized to unity.

K/π misidentification probability. The pionicity cut for the pion with the same charge as the muon was left unchanged at $W_K - W_\pi > 0$. The efficiency of applying pionicity cuts to simulated samples of $D^+ \rightarrow \rho^0\mu^+\nu$ and $D^+ \rightarrow \overline{K}^{*0}\mu^+\nu$ can be seen in Figure IV.8. It is clear that while applying harder cuts on the pion with the same charge as the muon has the same effect on both samples, a harder cut on the pion with opposite charge as the muon greatly reduces the $D^+ \rightarrow \overline{K}^{*0}\mu^+\nu$ background compared to the $D^+ \rightarrow \rho^0\mu^+\nu$ signal.

The baseline cut set required the secondary vertex to have CL_{sec} greater than 1% and Iso2, secondary vertex isolation, less than 1%. The secondary vertex was required to be outside the target (OoT$> 0\sigma$). The secondary vertex was also required to be outside all
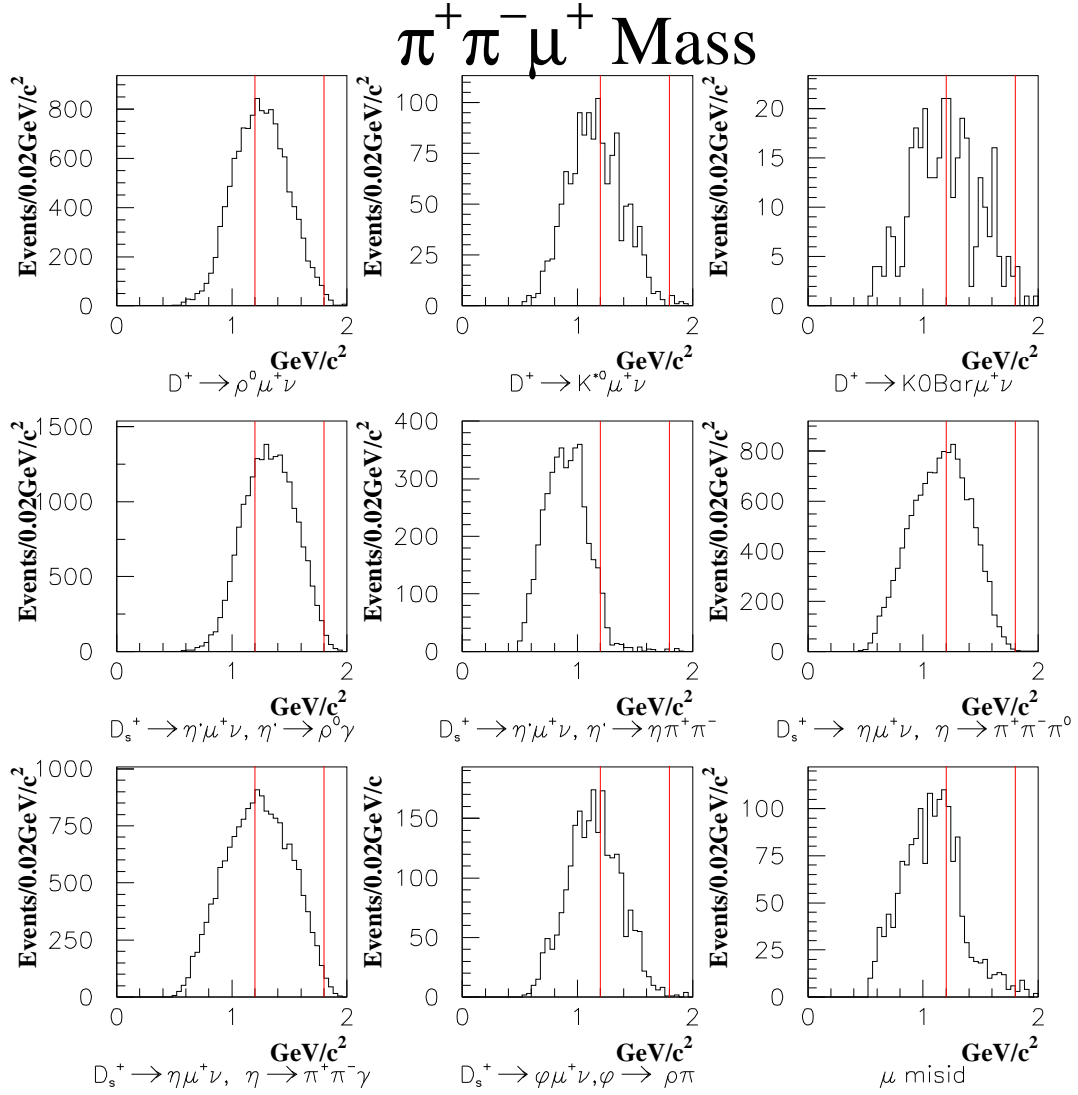
Figure IV.6: $M(\pi^+\pi^-\mu^+)$ mass cut. In this plot the effect of cutting on the mass $M(\pi^+\pi^-\mu^+)$ of signal and background channels can be seen. The red line indicates the cut applied.
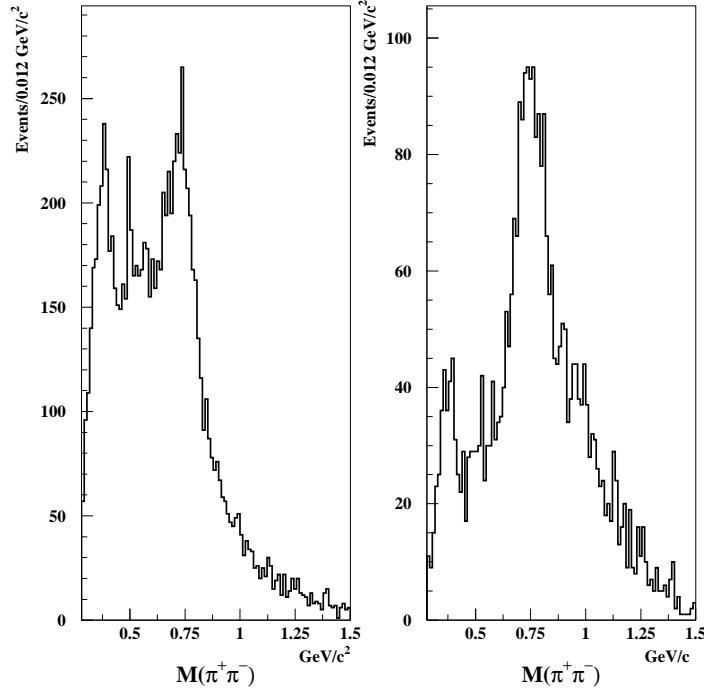
Figure IV.7: $M(\pi^+\pi^-\mu^+)$ mass cut effect on the data. Left, $M(\pi^+\pi^-)$ for events with no cut on $M(\pi^+\pi^-\mu^+)$. Right, $M(\pi^+\pi^-)$ for events with a cut on $M(\pi^+\pi^-\mu^+)$ as described in the text. All other baseline cuts are applied equally to both plots.

material[2] (OoM $> 0\sigma$). For the primary vertex, the minimum confidence level was set to 1% while the primary vertex isolation cut, Iso1, was less than 1%. The minimum separation between the primary and the secondary vertex was left at 5σ's.

Once the baseline cut set was determined, we began to change these cuts in order to find the best possible cut combination. Changing all possible cuts is a computer–intensive task. In order to minimize the time required for this, only a subset of the cuts, those that discriminate best between charmed and non–charmed decays, and between signal and backgrounds, were changed. The chosen cuts are L/σ, CL_{sec}, Iso2, out of target, and pionicity of the pion with opposite charge as the muon. In total, 1260 cut combinations were tested. The values used for the cuts are summarized in Table IV.1. The results of the test are shown in Figure IV.9, where we have plotted the branching fraction ratios for

---

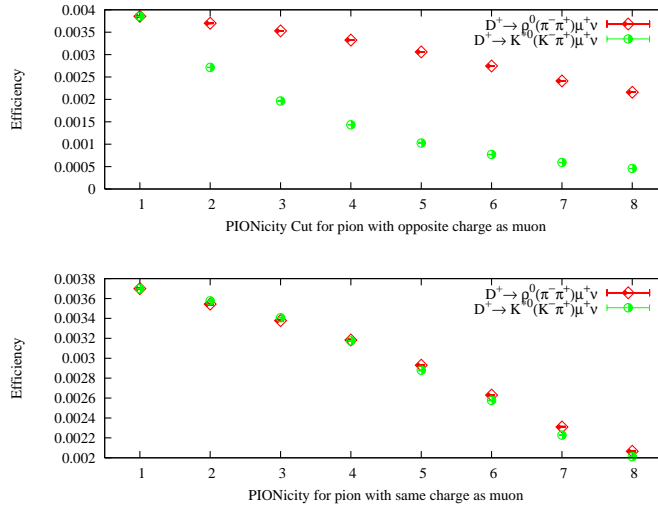[2]Material is defined as target + SSD.

Figure IV.8: Efficiency of pionicity cuts for $D^+ \to \rho^0 \mu^+ \nu$ and $D^+ \to \overline{K}^{*0} \mu^+ \nu$ samples. Both samples were treated equally. The $D^+ \to \overline{K}^{*0} \mu^+ \nu$ efficiency was normalized to match the $D^+ \to \rho^0 \mu^+ \nu$ sample efficiency for $W_K - W_\pi$ greater than 1. Top, pionicity cut applied to the pion with opposite charge as the muon. Bottom, pionicity cut applied to pion with same charge as the muon. The figure shows that in order to minimize the $D^+ \to K^- \pi^+ \mu^+ \nu$ background, the pionicity cut needs to be applied to the pion opposite charge as the muon.

the 1260 cut combinations. A clear pattern emerges when the combinations are plotted. Within each plot, corresponding to a value of L/σ, the four values of the Out of Target cut are distinguishable. Furthermore, there are large variations, within each Out of Target cut, that correspond to the changes in the pionicity cut. These variations are independent of any other cut applied, suggesting that when there is a considerable amount of $D^+ \to K^- \pi^+ \mu^+ \nu$ background present, the fit overestimates the $D^+ \to \rho^0 \mu^+ \nu$ yield. The overestimation of the $D^+ \to \rho^0 \mu^+ \nu$ yield is the consequence of underestimating of the K/π misidentification rate in the Monte Carlo for low values of pionicity [36].

Selecting which cut combination to use as our final selection requirements is a subjective decision since several selection requirements produce similar results. Thus, we established a criteria, striving to be as unbiased as possible, that could distinguish between all such combinations. The decision was made based on two considerations. First, which combination maximizes the significance of the relative branching fraction ratio, and second,

90

Table IV.1: Cut values used to find final cut combination. A total of 1260 cut combinations were tested.

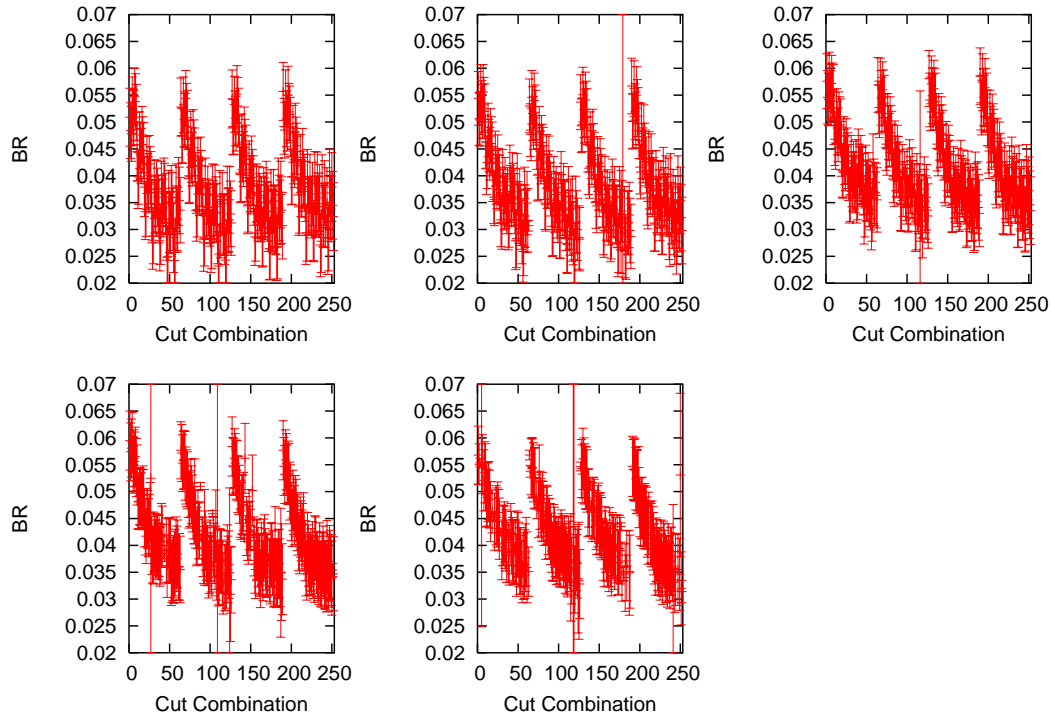| Cut	Cut Values
L/σ	5, 10, ..., 25
CL_{sec}	0.01, 0.05, 0.10
Iso2	0.10, 0.01, 0.001
Out of Target	0,1,2,3
Pionicity	1,2, ..., 7

Figure IV.9: Branching fraction ratio for the 1260 cut combinations. Each plot corresponds to an L/σ cut value ranging from $L/\sigma > 5$ (top left) to $L/\sigma > 25$ (bottom right). In each plot, four regions, corresponding to the four Out of Target cut values are distinguishable. The large variations within these four regions correspond to variations in the pionicity cut. Extremely large error bars on some of the data points indicate a failed fit.

which combination resulted in the best match between the fit and data histograms. Based on this, we chose the events that had $L/\sigma > 15$, $\text{CL}_{\text{sec}} > 0.05$, Iso2 < 0.01, OoT $> 1\sigma$, and $W_{\text{K}} - W_{\pi} > 5$. The final cut combination is summarized in Table IV.2. In this table Mispl refers to the maximum number of muon planes allowed to have missing hits; TRKFIT is the confidence level of the hypothesis that muon momentum determination is consistent as measured in M1 and M2 independently; REME is the maximum confidence level for the hypothesis that the track is consistent with having zero–degree angle with respect to the beamline.

Table IV.2: Cuts applied to the $\pi\pi\mu$ sample.

Tracking	Part. I.D.	Vertexing	Inv. Mass
REME$> 3\%$	$\mu_p > 10\text{GeV}/c$ (IMU)	$L/\sigma > 15$	$0.28 < M(\pi^+\pi^-) < 1.5$
Singly Linked	$\text{CL}_\mu > 1\%$ (IMU)	$\text{CL}_{\text{sec}} > 5\%$	$M(\pi^+\pi^-\mu^+) - M(\pi^-\mu^+) > 0.20$
	Mispl< 2 (IMU)	Iso2 $< 1\%$	$1.2 < M(\pi^+\pi^-\mu^+) < 1.8$
	TRKFIT $> 1\%$ (IMU)	Sec. OoT $> 1\sigma$	
	$W_{\text{best}} - W_{\pi_{1,2}} > -5$	Sec. OoM $> 0\sigma$	
	$W_{\text{K}} - W_{\pi_1} > 5$	$\text{CL}_{\text{prim}} > 1\%$	
	$W_{\text{K}} - W_{\pi_2} > 0$	Iso1 $< 1\%$	

IV.5.1 $D^+ \to \rho^0\mu^+\nu$ **Fit Results**

After applying the cuts, the maximum log likelihood fit was performed. A total of 320 ± 44 $D^+ \to \rho^0\mu^+\nu$ events survived these cuts. The results of the fit are shown in Figure IV.10. The contributions to the fit histogram from the individual sources are summarized in Table IV.3. The largest contributions to the background are muon misidentification and combinatorial backgrounds.

In order to test the stability of the cuts and make sure that we were not choosing a cut combination that resulted in a statistical fluctuation, we scanned the L/σ, OoT, CL_{sec}, and pionicity cuts one by one (after fixing the others) and plotted the Efficiency Corrected yield (ECY), defined as

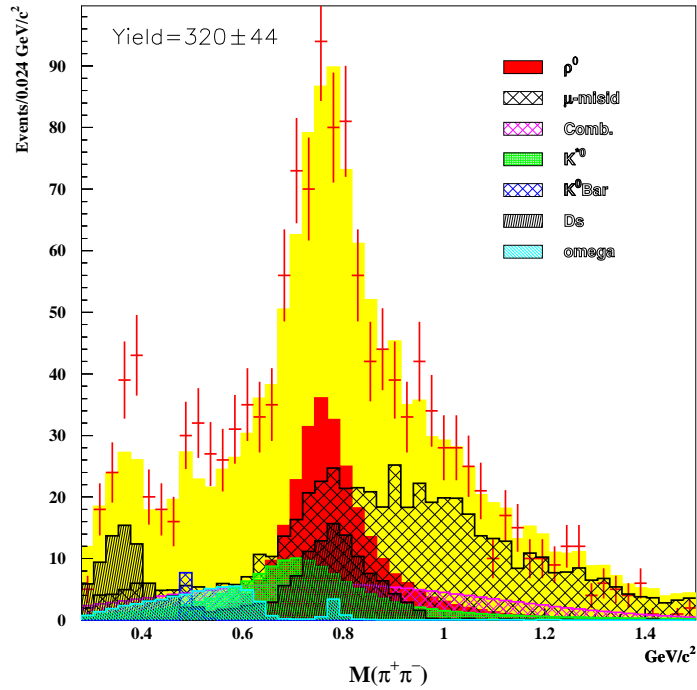$$ECY = \text{Yield/efficiency}. \tag{IV.7}$$

Figure IV.10: $M(\pi^+\pi^-)$ fit. The data (red with error bars) histogram is superimposed on the fit histogram (solid yellow).

Table IV.3: Contributions to the $M(\pi^+\pi^-)$ fit histogram

Decay Mode	Yield
$D^+ \to \rho^0 \mu^+ \nu$	320 ± 44
$\overline{K}^{*0}, K/\pi$ Mis-id	68
$D^+ \to \overline{K}^0 \mu^+ \nu$	7 ± 6
D_s^+ modes total	181 ± 39
$D^+ \to \omega \mu^+ \nu$	51 ± 22
Muon Mis-Id	554 ± 43
Combinatorial	233 ± 50

The ECY represents the number of events produced in the experiment, thus it is invariant with respect with the cuts applied to the sample. This exercise is shown in Figure IV.12. The figure shows that all cuts, except for the scan in pionicity of the pion with opposite charge as the muon, are very stable as we scan from very loose to very hard cuts. The pionicity plot becomes stable once the cut is set to at least three units of
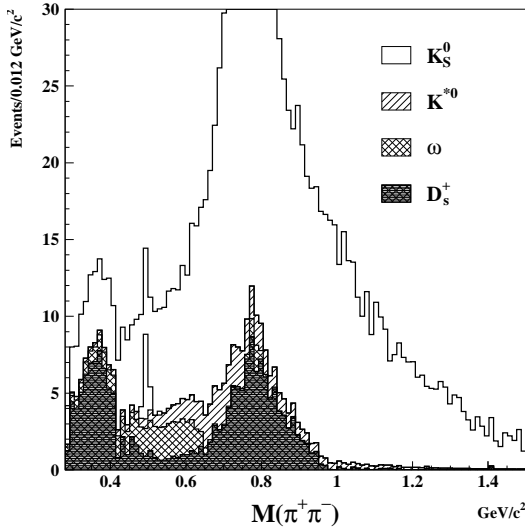
(a) Semileptonic contributions
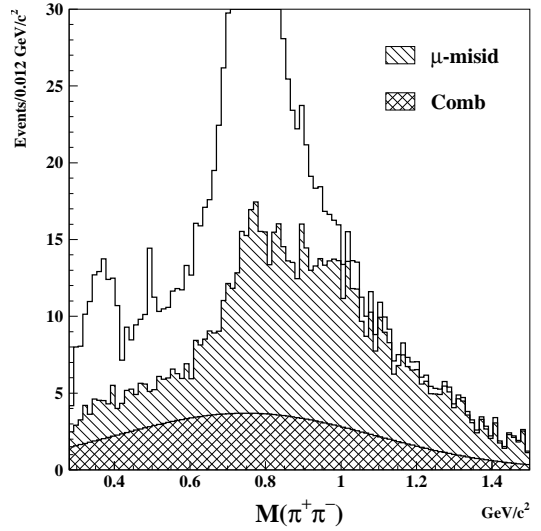
(b) Muon misidentification and combinatorial backgrounds

Figure IV.11: $M(\pi^+\pi^-)$ background contributions shown as cumulative plots. The fit histogram is shown in both plots for reference.

likelihood. This is the result of underestimating the K/π misidentification rate in MC for low values of pionicity discussed in Section IV.5.

IV.6   Normalization Mode

The Cabibbo favored $D^+ \rightarrow K^-\pi^+\mu^+\nu$ decay channel serves as the ideal normalization mode since it shares many features with $D^+ \rightarrow \rho^0(\pi^+\pi^-)\mu^+\nu$. Because of this, the skim and cut requirements can be made almost identical. The main advantage of having similar decay topologies is that most of the common systematics, like the detector's response and Monte Carlo simulation, will cancel out when taking the ratio.

The $D^+ \rightarrow K^-\pi^+\mu^+\nu$ sample used for the normalization has the same requirements, up to Skim Three, as the $D^+ \rightarrow \rho^0\mu^+\nu$ sample. During Skim Three, those events with a muon and oppositely charged Kaon–pion combination in the decay vertex, as opposed to pion–pion combination, were flagged as $D^+ \rightarrow K^-\pi^+\mu^+\nu$ candidates and were output to
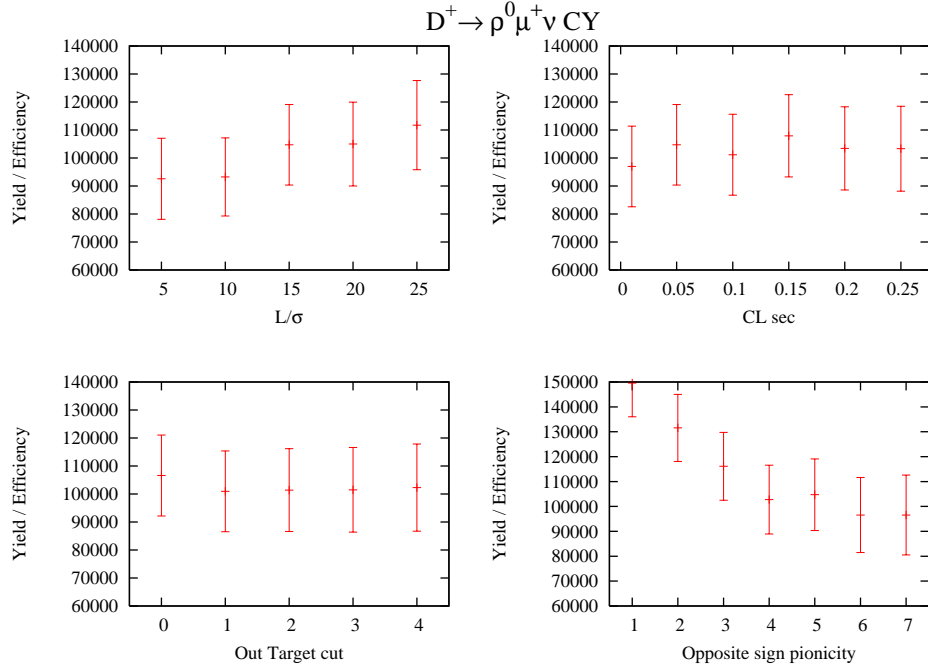
Figure IV.12: Efficiency Corrected Yield for the $D^+ \to \rho^0 \mu^+ \nu$ sample. From top left to bottom right: L/σ, $\mathrm{CL_{sec}}$, OoT, and $W_K - W_\pi$ cut scans. In each plot only the cut that is being plotted has been changed. All other cuts are set to their final value as stated in the text.

a different stream. As previously stated, the requirement for a track to be identified as a Kaon was to have a $W_\pi - W_K > 1$.

As was the case with $D^+ \to \rho^0 \mu^+ \nu$, the $K\pi\mu$ Skim Three output stream was subjected to further (very loose) requirements designed to expunge the more blatantly wrong combinations. During this stage, all the variables needed for the analysis were calculated and output into an Ntuple for interactive analysis. The mass of the $K^-\pi^+$ system for those events passing the requirements described above is shown in Figure IV.13. Even when very loose selection requirements are made, there is a clear $\overline{K}^{*0} \to K^-\pi^+$ signal present on top of a smooth background.

An important consideration in the selection of $D^+ \to K^-\pi^+\mu^+\nu$ events is the distinction between Right Sign (RS) and Wrong Sign (WS) events. Events flagged as RS are those where the Kaon and the muon have opposite sign; events flagged as WS are those where the Kaon and muon have the same charge. In both cases, the secondary vertex has
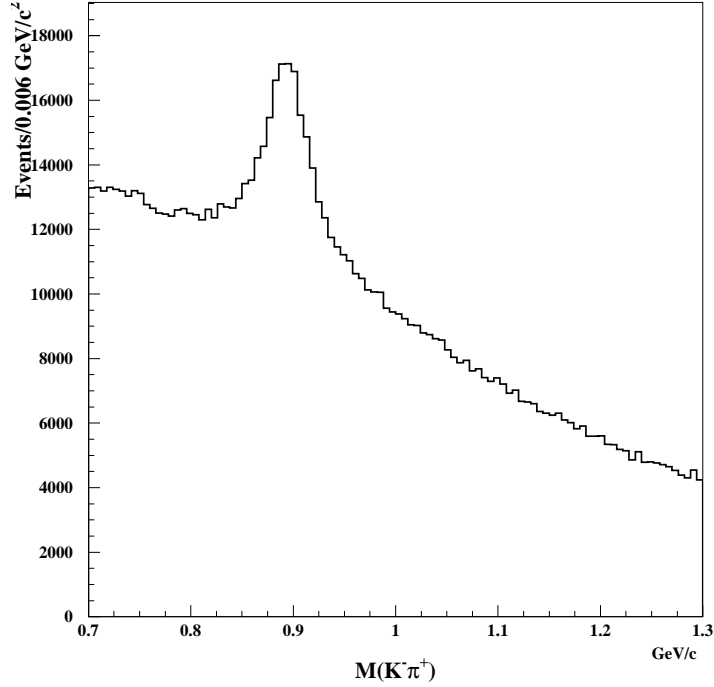
Figure IV.13: M($K^-\pi^+$) candidates for events passing Skim Three and loose selection criteria.

unit charge and the Kaon–pion combination is neutrally charged. The WS events can be used to gauge the level of combinatorial background present in the signal.

The final selection criteria applied to $D^+ \rightarrow K^-\pi^+\mu^+\nu$ events differs only slightly compared to the selection criteria imposed on the $D^+ \rightarrow \rho^0\mu^+\nu$ sample. Two main differences are the Kaon/pion identification requirements and the use of the RS events. In what follows, the final selection requirements are discussed.

Tracks with $W_\pi - W_K > 1$ were identified as Kaons, while those with $W_K - W_\pi > 0$ were identified as pions. Only muons accepted into the IMU were considered. Tracks with momentum greater than 10 GeV/c, with hits in at least five of the six IMU planes were identified as muons if they had $\mathrm{CL}_\mu > 0.01$.

The secondary vertex was found using DVERT by combining the Kaon, pion, and muon

candidates. The secondary vertex was required to have unit charge. Furthermore, the Kaon and the muon candidates were required to be oppositely charged. Only events with a secondary vertex occurring outside of the target material with $\mathrm{CL_{sec}} > 0.05$ and $\mathrm{Iso2} < 0.01$ were accepted. The primary vertex was found from the remaining tracks in the event (after excluding the tracks in the secondary) using DVFREE. Primary vertices were required to have $\mathrm{CL_{prim}} > 0.01$ and $\mathrm{Iso1} < 0.01$. The minimum separation between the primary and secondary vertex was required to have $L/\sigma > 15$.

In order to allow for the missing energy of the neutrino, and at the same time reduce contamination from higher multiplicity states, we required $1.0 < M(K^-\pi^+\mu^+) < 1.8$. As with the $D^+ \rightarrow \rho^0\mu^+\nu$ data, background from $D^{*0} \rightarrow D^0(K^-\mu^+\nu)\pi^+$ where the soft pion is erroneously assigned to the secondary vertex was minimized by requiring $M(K^-\pi^+\mu^+) - M(K^-\mu^+) > 0.20$.

Table IV.4: Cuts applied to the $K\pi\mu$ normalization sample.

Tracking	Part. I.D.	Vertexing	Inv. Mass
REME$> 3\%$	$\mu_p > 10\mathrm{GeV}/c$ (IMU)	$L/\sigma > 15$	$0.7 < M(K^-\pi^+) < 1.3$
Singly Linked	$\mathrm{CL}_\mu > 1\%$ (IMU)	$\mathrm{CL_{sec}} > 5\%$	$M(K^-\pi^+\mu^+) - M(K^-\mu^+) > 0.20$
	Mispl< 2 (IMU)	$\mathrm{Iso2} < 1\%$	$1.0 < M(K^-\pi^+\mu^+) < 1.8$
	TRKFIT $> 1\%$ (IMU)	Sec. OoT $> 1\sigma$	
	$W_\pi - W_{\mathrm{K}} > 2$ (Kaon)	Sec. OoM $> 0\sigma$	
	$W_{\mathrm{K}} - W_\pi > 0$ (pion)	$\mathrm{CL_{prim}} > 1\%$	
		$\mathrm{Iso1} < 1\%$	

The $D^+ \rightarrow K^-\pi^+\mu^+\nu$ yield was estimated by fitting $M(K^-\pi^+)$ of the surviving events using a binned maximum log likelihood fit. The likelihood function was defined as

$$\mathcal{L} = \prod_{i=1}^{\#\mathrm{bins}} \frac{n_i^{s_i} e^{-n_i}}{s_i!}. \tag{IV.8}$$

In the previous equation the symbols n_i and s_i have the same meaning as in (IV.1). In this case, only two shapes were needed to get a good estimate of the $D^+ \rightarrow K^-\pi^+\mu^+\nu$

yield. The number of events in bin i of the fit histogram was simply defined as

$$n_i = Y_{D^+ \to K^- \pi^+ \mu^+ \nu} S_{K^- \pi^+ \mu^+ \nu} + Y_{\text{BG}} S_{\text{BG}}. \qquad \text{(IV.9)}$$

The first shape is the $D^+ \to K^- \pi^+ \mu^+ \nu$ signal and the second shape is a background obtained from a large $c\bar{c}$ Monte Carlo where the $D^+ \to K^- \pi^+ \mu^+ \nu$ signal mode was filtered out. This background represents all possible charm contributions to the background. Included in this shape are contributions from muon–misidentification and combinatorial background. The results of the $D^+ \to K^- \pi^+ \mu^+ \nu$ fit are shown in Figure IV.14.
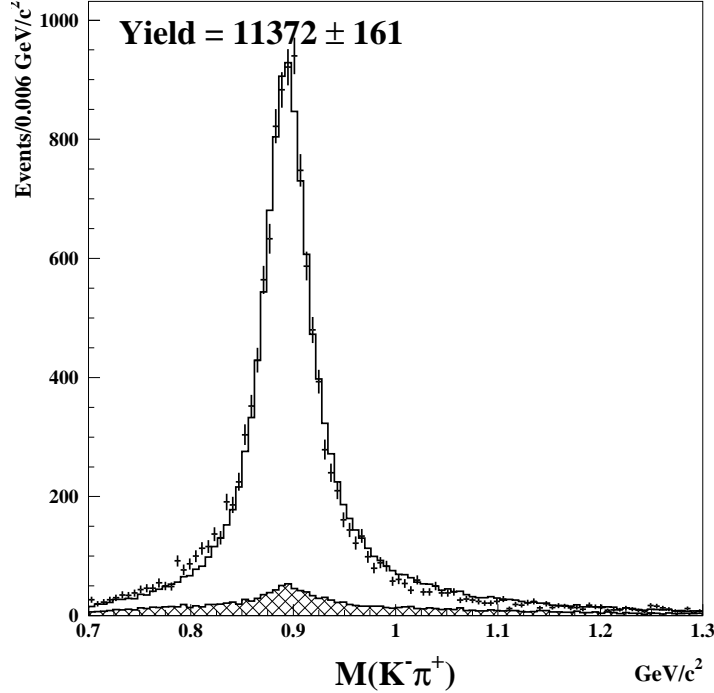

Figure IV.14: Fit to $M(K^- \pi^+)$ for the normalization mode using a binned maximum log likelihood technique.

The $D^+ \to K^- \pi^+ \mu^+ \nu$ yield obtained using the procedure detailed above was checked by fitting the $M(K^- \pi^+)$ following the methodology outlined in Reference 37. For this, the WS contribution is subtracted from the RS and the resulting histogram is fitted using a Breit-Wigner line-shape plus a first order polynomial as shown in Figure IV.15. The

subtraction of the WS is justified since the combinatorial background that gives rise to it is symmetric with respect to the charge of the hadrons.
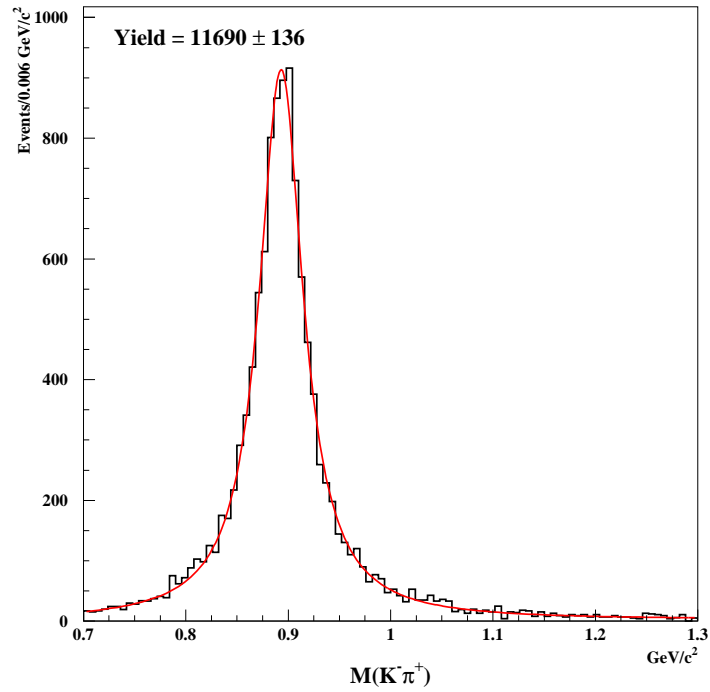

Figure IV.15: Fit to $M(K^-\pi^+)$ for the normalization mode using a S–wave Breit Wigner lineshape. The wrong sign has been subtracted prior to the fit.

CHAPTER V

RELATIVE BRANCHING FRACTION RATIO RESULTS

From the fits to the $\pi^+\pi^-$ and $K^-\pi^+$ invariant masses we found 320 ± 44 and 11372 ± 162 $D^+ \to \rho^0\mu^+\nu$ and $D^+ \to K^-\pi^+\mu^+\nu$ events, respectively. With these yields and the Monte Carlo efficiencies for the signal and normalization modes, the relative branching fraction ratio, $\frac{\Gamma(D^+\to\rho^0\mu^+\nu)}{\Gamma(D^+\to\overline{K}^{*0}\mu^+\nu)}$, was calculated using (IV.6). We found

$$\frac{\Gamma(D^+ \to \rho^0\mu^+\nu)}{\Gamma(D^+ \to \overline{K}^{*0}\mu^+\nu)} = 0.0412 \pm 0.0057.$$

The stability of the results can be seen by plotting $\frac{\Gamma(D^+\to\rho^0\mu^+\nu)}{\Gamma(D^+\to\overline{K}^{*0}\mu^+\nu)}$ as the variables are scanned. This is shown in Figure V.1. The relative branching fraction ratio follows closely the ECY shown in Figure IV.12.

In order to check that the statistical error reported by the fit was accurate, we performed a mini Monte Carlo study where each bin of the $D^+ \to \rho^0\mu^+\nu$ data histogram was fluctuated using a Poisson distribution. The resulting fluctuated histogram was then fit following the standard procedure and the resulting branching fraction ratio was saved. This process was repeated around 950 times and the distribution of the $\frac{\Gamma(D^+\to\rho^0\mu^+\nu)}{\Gamma(D^+\to\overline{K}^{*0}\mu^+\nu)}$ branching fraction ratio was plotted. If the statistical error reported by the fit to the data is correct then it should be consistent with the standard deviation of the distribution of the fluctuated results. The standard deviation of the fluctuated results was obtained by fitting the distribution using a Gaussian function. The result of this study is shown in Figure V.2. The standard deviation extracted from the Gaussian fit was 0.0057. Both the mean of the distribution as well as the standard deviation are in excellent agreement with the values returned by the fit.
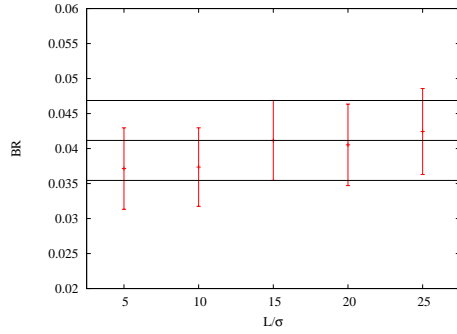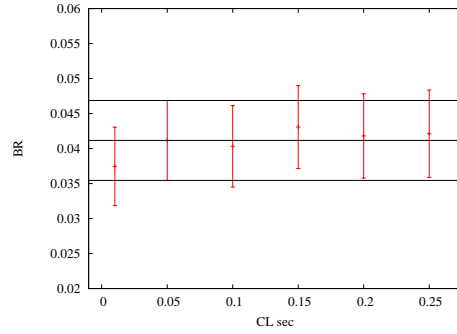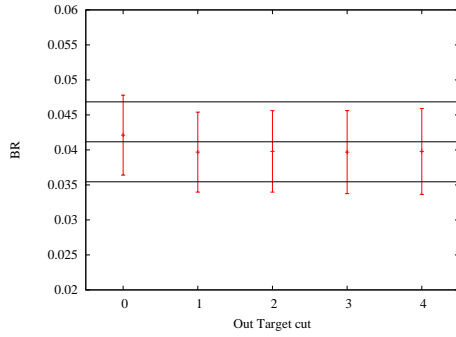
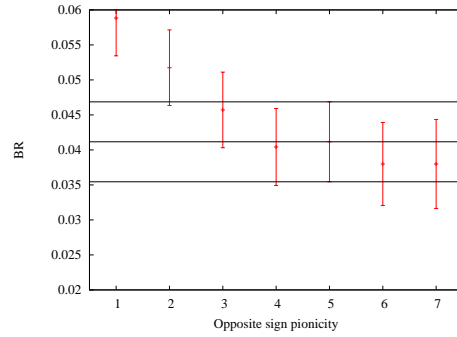Figure V.1: Relative branching fraction ratio. From top left to bottom right: L/σ, CL_{sec}, OoT, and $W_K - W_\pi$ cut scans. In each plot only the cut that is being plotted has been changed. All other cuts are set to their final value as stated in the text.
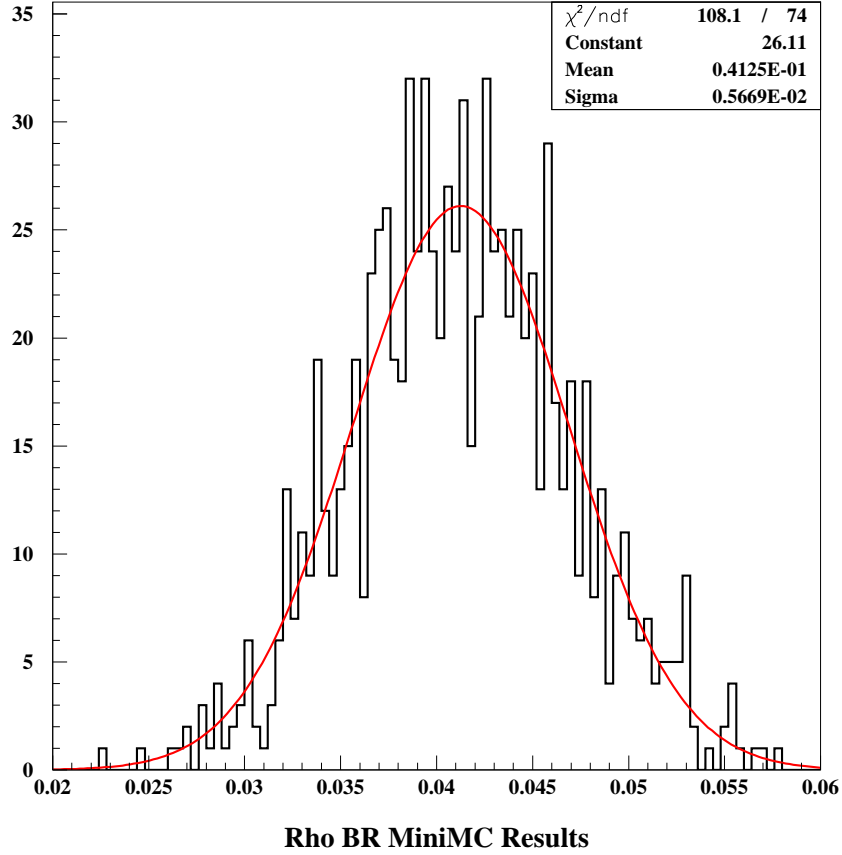
χ²/ndf	108.1 / 74
Constant	26.11
Mean	0.4125E-01
Sigma	0.5669E-02

Rho BR MiniMC Results

Figure V.2: Distribution of $\frac{\Gamma(D^+ \to \rho^0 \mu^+ \nu)}{\Gamma(D^+ \to \overline{K}^{*0} \mu^+ \nu)}$ results using fluctuated data.

V.1 Systematic Studies

Several studies were performed in order to asses systematic contributions to the ratio. Three possible contributions were identified. The first is due to the final cut selection, the second contribution is due to the fitting procedure, and the third, is due to possible uncertainty that may come from the detector simulation and charm production mechanism used to generate the Monte Carlo samples.

V.1.1 Cut Systematics

The final set of cuts applied to the data was chosen based on maximizing the significance of the branching fraction ratio and minimizing the χ^2/DOF between the data

and the fit histograms. To test that our final result was not the product of a statistical fluctuation or strange extrema, we varied the cuts around the final choice in order to exercise likely differences between signal and backgrounds. For each new cut combination, applied (when possible) to both signal and normalization mode, the branching fraction ratio was calculated. We looked for cuts that should have different effects on both the data and backgrounds and assumed that the resulting branching fraction ratios were, a priori, the same. The sample variance for the returned values of the branching fraction ratio was then used as our systematic uncertainty due to the final cut combination. The cut variations are described below.

Since the D^+ is longer–lived compared to sources of background from D_s^+, and other short-lived backgrounds such as those coming from non-charm sources, we varied the significance of the separation between the production and the decay vertices from 10σ to 20σ, and out of target requirements for the decay vertex from 0σ to 2σ. To look for poorly formed vertices and vertices that are formed from particles that decayed into muons early in the spectrometer, we varied the confidence level of the secondary vertex from 1% to 10%. We had estimated the feed-down from $D^+ \rightarrow K^-\pi^+\mu^+\nu$ using our Monte Carlo simulation, but looked for backgrounds we might have missed by varying the Čerenkov identification cuts for the pions from 4 to 6 units of likelihood. The level of the muon misid was checked by changing the muon identification confidence level from 1% to 10%, the muon momentum cut from 10 GeV/c to 20 GeV/c, and selecting events that left hits in all 6 of the muon planes. A very stringent test which dramatically changes the background level was to relax the visible mass cut. Though the statistical significance of the result suffered due to the inclusion of so much background, this was an important check on backgrounds we might have missed coming from higher multiplicity modes, which were expected to be small, and combinatorial sources.

These variations resulted in changes in yields from -30% to +45%. In terms of signal to background ratios, the variations yielded changes ranging from -50% to +35%. Because

Table V.1: Cut variations used to assess the systematic uncertainty due to our cut selection.

Cut	Default Value	Variation
L/σ	15	10, 20
OoT	1	0, 2
OoM	0	1, 2
CL_{sec}	0.05	0.01, 0.10
Iso2	0.01	0.10, 0.001
Mispl (IMU)	2	1
μ_p (IMU)	$10\,\mathrm{GeV}/c$	15, 20 (GeV/c)
CL_μ (IMU)	0.01	0.05, 0.10
$W_K - W_{\pi_1}$	5	4, 6
$M(\pi^+\pi^-\mu^+) - M(\pi^-\mu^+)$	0.20	No cut

our tested cuts have succeeded in delivering a broad range of signal to background values as well as changes in the final yield, this method is likely to deliver a conservative estimate of the systematic error due to our cut selection. We found no significant change in the branching ratio due to our particular cut choice and assigned a systematic uncertainty of 0.0023 due to our cut selection. The resulting branching fraction ratios are shown in Figure V.3.
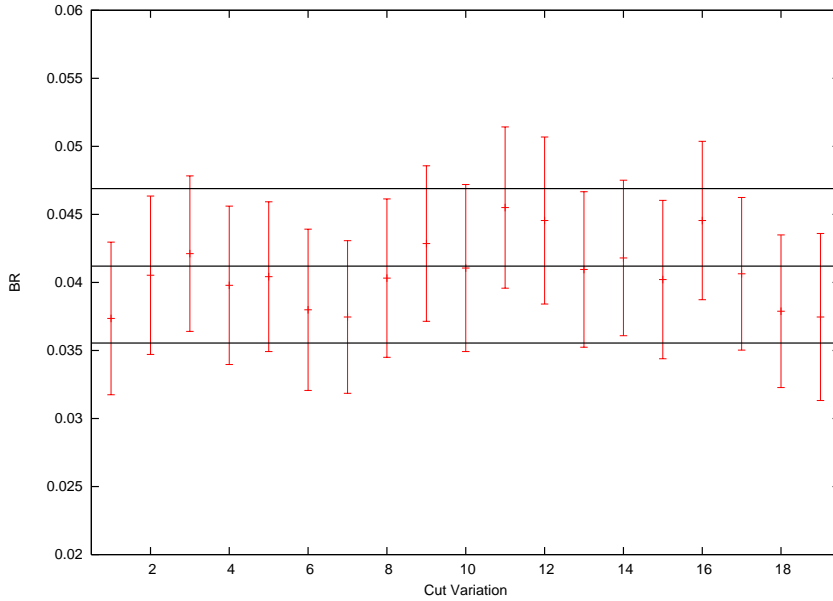

Figure V.3: $\frac{\Gamma(D^+\to\rho^0\mu^+\nu)}{\Gamma(D^+\to\overline{K}^{*0}\mu^+\nu)}$ for cut systematics. The solid lines represent the results with the standard cut set.

V.1.2 Fit Systematics

When performing the fit to the signal and normalization modes we can inadvertently introduce biases that could affect the final result. For example, when dealing with low statistic samples, like the $D^+ \to \rho^0 \mu^+ \nu$ data, the binning scheme and fitting range can affect the true shape of the distribution. Therefore, it is important to check every assumption and decision made during the fitting step.

Even more important than the binning scheme and the fitting range used in the fit, the choices over how to deal with the shapes used as backgrounds and how to estimate their yields could have a significant effect on the $D^+ \to \rho^0 \mu^+ \nu$ yield. The first of those decisions was the estimation of the $D^+ \to \overline{K}^{*0} \mu^+ \nu$ background based on the $D^+ \to \overline{K}^{*0} \mu^+ \nu$ ECY obtained during the normalization process. We decided to fix this parameter as opposed to adding it as a fit parameter because, apart from the slightly shifted mass peak compared to the $D^+ \to \rho^0 \mu^+ \nu$ signal, the shapes are very similar, and therefore, hard to differentiate. Second, we chose to use a penalty term to constrain the $D^+ \to \omega \mu^+ \nu$ yield as opposed to have this yield as a free parameter in the fit. Lastly, we chose to use only one shape encompassing all the D_S semileptonic modes instead of generating them individually. This implies that we trust that all the relevant D_s relative branching ratios in our Monte Carlo are correct.

In order to test for biases introduced by these choices we vary the $D^+ \to \overline{K}^{*0} \mu^+ \nu$ ECY by a factor of plus/minus two, effectively doubling/halving the amount of K/π misidentification allowed in the signal region. Note that this is an extreme variation since the actual expected variation on the ECY was at most a few sigmas ($\sigma_{\mathrm{ECY}}/\mathrm{ECY} \sim 1.4\%$). In the case of the $D^+ \to \omega \mu^+ \nu$ yield, we performed the fit without any constraints on the yield using it as a free parameter of the fit.

As discussed in Section IV.2, many different D_s semileptonic modes contribute to the $M(\pi^+ \pi^-)$ background. The advantage of using a single shape arising from a large $c\bar{c}$ Monte Carlo sample is that the resulting shape will contain all the relevant modes

with their expected rates and relative branching fractions. Because some of the relative branching fractions involved are better known than others it is important to check how sensitive the results are to the relative branching fractions assumed in our Monte Carlo. We tested this by performing the fit using one distinct shape for each D_s mode we believed to be present in the background.

Adding each D_s mode as an additional free parameter in the fit was not a viable option. The main difficulty arises because modes such as $D_s^+ \to \eta' \mu^+ \nu$ with $\eta' \to \rho^0 \gamma$ and $D_s^+ \to \phi \mu^+ \nu$ with $\phi \to \rho \pi$ are reconstructed with the same mass as the $D^+ \to \rho^0 \mu^+ \nu$ signal. This makes it extremely difficult for the fit to separate signal from background. Fortunately, we can tie the level of background underneath the signal to the background present in the low mass region due to $D_s^+ \to \eta' \mu^+ \nu$ with $\eta' \to \eta \pi \pi$ and $D_s^+ \to \eta \mu^+ \nu$ with $\eta \to \pi \pi \pi^0$ with knowledge of the $D_s^+ \to \phi \mu^+ \nu$ efficiency corrected yield. We do this with the use of the known relative branching fractions $\frac{BR(D_s \to \eta' \ell \nu)}{BR(D_s \to \phi \ell \nu)}$ and $\frac{BR(D_s \to \eta \ell \nu)}{BR(D_s \to \phi \ell \nu)}$, along with the branching fractions and efficiencies for each individual background source. The D_s yield fit parameter in (IV.2) was then replaced by

$$
\mathrm{N}^{\text{fitPar}}_{D_s^+ \to \phi \mu^+ \nu} \frac{\Gamma(D_s \to \eta' \ell \nu)}{\Gamma(D_s \to \phi \ell \nu)} \left[\left(BR(\eta' \to \rho^0 \gamma) \epsilon(\eta' \to \rho^0 \gamma) S_i + BR(\eta' \to \eta \pi \pi) \epsilon(\eta' \to \eta \pi \pi) S_i \right) \right] +
$$
$$
\mathrm{N}^{\text{fitPar}}_{D_s^+ \to \phi \mu^+ \nu} \frac{\Gamma(D_s \to \eta \ell \nu)}{\Gamma(D_s \to \phi \ell \nu)} \left[\left(BR(\eta \to \pi \pi \pi^0) \epsilon(\eta \to \pi \pi \pi^0) S_i + BR(\eta \to \pi \pi \gamma) \epsilon(\eta \to \pi \pi \gamma) S_i \right) \right] +
$$
$$
\mathrm{N}^{\text{fitPar}}_{D_s^+ \to \phi \mu^+ \nu} BR(\phi \to \rho \pi) S_i
$$

$$\text{(V.1)}$$

where $\mathrm{N}^{\text{fitPar}}_{D_s^+ \to \phi \mu^+ \nu}$ is a new fit parameter representing the $D_s^+ \to \phi \mu^+ \nu$ efficiency corrected yield, the total number of $D_s^+ \to \phi \mu^+ \nu$ produced in the experiment. $\epsilon(X)$ is the efficiency for the mode X to be reconstructed as a $D^+ \to \rho^0 \mu^+ \nu$ event, and S_i is the shape associated with each mode. Since the relative branching fraction ratios, as well as the branching fractions are known we can fit for the number of $D_s^+ \to \phi \mu^+ \nu$ produced in the experiment. In this way we can vary the relevant branching fractions within their known uncertainties

while at the same time controlling the total D_s contribution with a single fit parameter. The resulting fit is shown in Figure V.4.
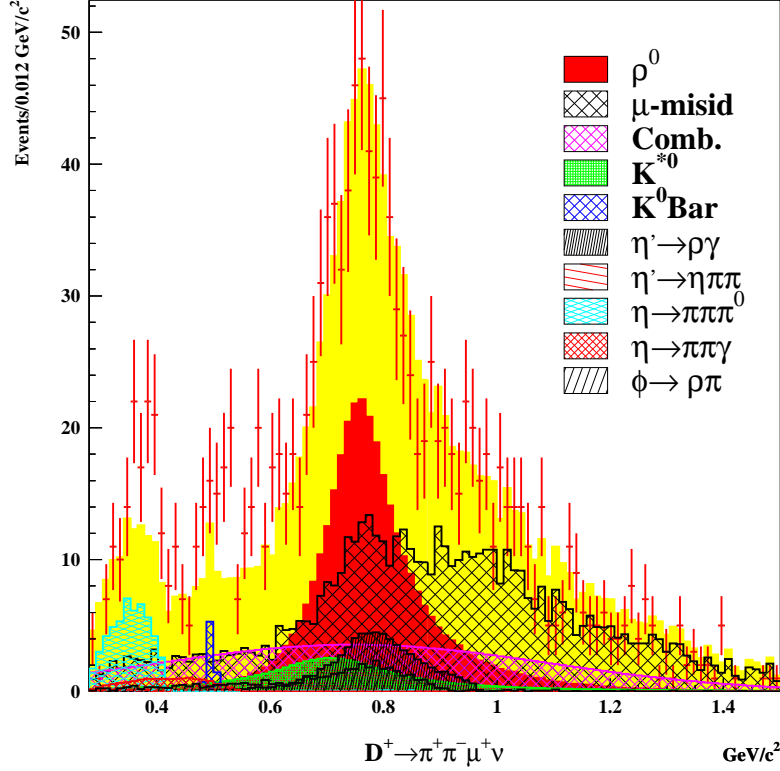

Figure V.4: $M(\pi^+\pi^-)$ fit using individual shapes for D_s contribution. The fit returns a total of 333 ± 43 $D^+ \to \rho^0 \mu^+ \nu$ events.

One additional advantage of this approach is that $N_{D_s^+ \to \phi\mu^+\nu}$ can be measured independently via the decay $\phi \to K^- K^+$ and this result compared to the value returned by the fit. The total number of $D_s^+ \to \phi\mu^+\nu$ produced in the experiment, $N^{\text{measured}}_{D_s^+ \to \phi\mu^+\nu}$, is defined as

$$N^{\text{measured}}_{D_s^+ \to \phi\mu^+\nu} = \frac{Y_{D_s \to K^+K^-\mu^+\nu}}{\epsilon(D_s \to K^+K^-\mu^+\nu) \times BR(\phi \to K^-K^+)} \tag{V.2}$$

where $Y_{D_s \to K^+K^-\mu^+\nu}$ is the data yield, $\epsilon(D_s \to K^+K^-\mu^+\nu)$ is the efficiency for observing $D_s \to K^+K^-\mu^+\nu$ events, and $BR(\phi \to K^-K^+)$ is the branching fraction for a ϕ to decay into two oppositely charge Kaons. Figure V.5 shows the $M(K^-K^+)$ distribution for both data and Monte Carlo. Both distributions were fit using a Breit-Wigner lineshape.

We found $N^{\text{measured}}_{D_s^+ \to \phi \mu^+ \nu} = 416611 \pm 19550$. The returned fit parameter is $N^{\text{fitPar}}_{D_s^+ \to \phi \mu^+ \nu} = 339580 \pm 68996$.
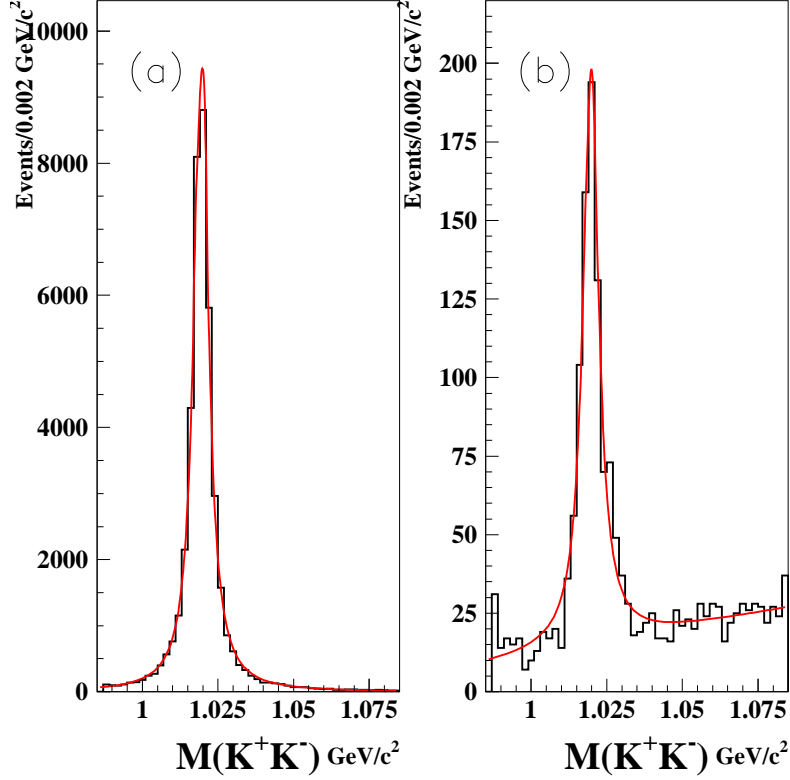

Figure V.5: $M(K^- K^+)$ distribution for Monte Carlo (left) and data (right). Both distributions have been fitted with a Breit-Wigner lineshape.

The last source of fit systematic considered is due to the shape selected to represent the combinatorial background. Although we believe that our choice for selecting this shape from a large $c\bar{c}$ Monte Carlo gives us an accurate representation of this kind of background, other possible ways of obtaining this shape are worth consideration.

One possibility is to use a variation of the technique used to model the non–charm/combinatorial background in $D^+ \to K^- \pi^+ \mu^+ \nu$. For real $D^+ \to K^- \pi^+ \mu^+ \nu$ the muon and Kaon candidates are oppositely charged. Nevertheless, vertices formed with a pion and a muon track with opposite charge were accepted and flagged as wrong sign candidates. The wrong sign events were then used to represent the combinatorial

Table V.2: Yields and reconstruction efficiencies for the semileptonic modes included in the fit.

Semileptonic Mode	Yield	Efficiency
$D^+ \rightarrow \rho^0 \mu^+ \nu$	333 ± 43	3.10×10^{-3}
$D^+ \rightarrow K^- \pi^+ \mu^+ \nu$	68	3.80×10^{-5}
$D^+ \rightarrow \overline{K}^0 \mu^+ \nu$	8 ± 6	3.20×10^{-6}
$D_s^+ \rightarrow \eta\prime(\rho^0\gamma)\mu^+ \nu$	69	1.57×10^{-3}
$D_s^+ \rightarrow \eta\prime(\eta\pi\pi)\mu^+ \nu$	2	2.28×10^{-5}
$D_s^+ \rightarrow \eta(\pi\pi\pi^0)\mu^+ \nu$	53	5.42×10^{-4}
$D_s^+ \rightarrow \eta(\pi\pi\gamma)\mu^+ \nu$	16	7.77×10^{-4}
$D_s^+ \rightarrow \phi(\rho\gamma)\mu^+ \nu$	42	7.94×10^{-4}
$D_s^+ \rightarrow \omega\mu^+ \nu$	51	1.02×10^{-3}

background since such combinations were most likely the result of randomly combining a Kaon and a pion to form the $\overline{K}^{*0}$.

In the $D^+ \rightarrow \rho^0 \mu^+ \nu$ case comparing the charge of one of the pions with that of the muon provides no clean distinction between right sign and wrong sign events. Nonetheless, we can accept and flag events with vertices made of same sign pions and use them to represent the combinatorial background. Although these events were likely the result of random combination of pions to form the ρ, there are two main reasons for why this approach is not preferred. First, this technique does not take into account the events where the muon candidate is the track that is being randomly assigned to the vertex, and second, charm decays with multiple pions can enter the distribution.

To test the sensitivity of the branching fraction result to the shape of the combinatorial background we performed the fit using the shape obtained using same sign pions from the data. This shape, obtained from both data and Monte Carlo sources is shown in Figure V.6. The good agreement between data and Monte Carlo provides furhter evidence that the $c\overline{c}$ Monte Carlo is able to reproduce the charm backgrounds well. A summary of the fit variations considered is presented in Table V.4.

The systematic associated with the fit was assessed by calculating the variance for the returned branching fraction ratios due to the fit variations. We found this contribution to be
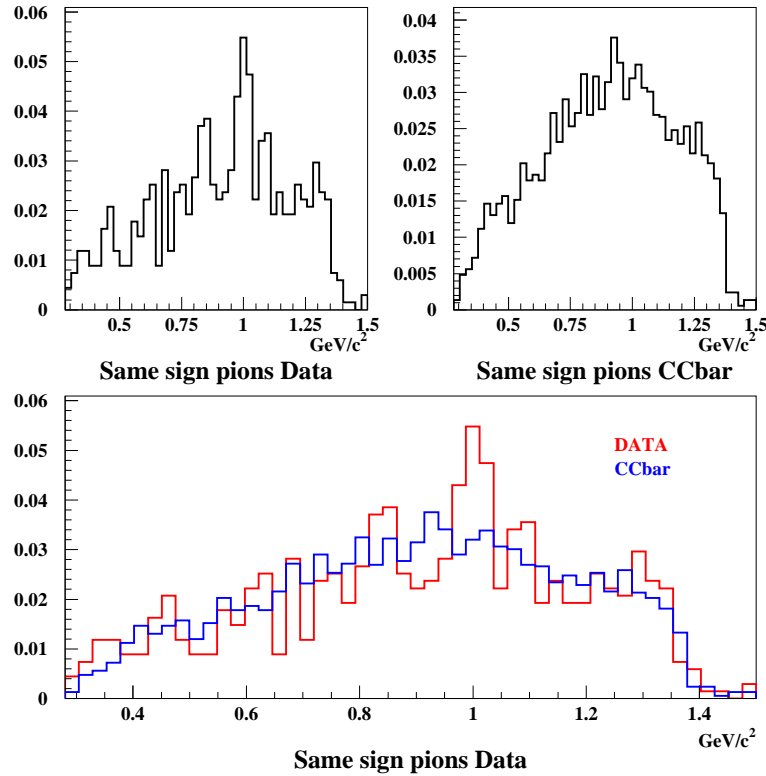
Figure V.6: $M(\pi\pi)$ distribution for events with same sign pions for data (red) and $c\overline{c}$ Monte Carlo (blue). The same sign pions distribution is used to represent the combinatorial background.

0.0033 mostly coming from the choice of combinatorial background shape. The branching fraction ratios for each fit variation are shown in Figure V.8.

V.1.3 Split Sample Systematics

The last type of systematic considered tests whether our Monte Carlo simulation can reproduce the different experimental conditions, as well as take into consideration the uncertainty associated with the charm production mechanism. To do this we split our sample in three pairs of statistically independent sub–samples. The first pair of sub–samples was split according to the D momentum. This a powerful test for the production model, trigger and detector simulation. Another test of the production mechanism was to
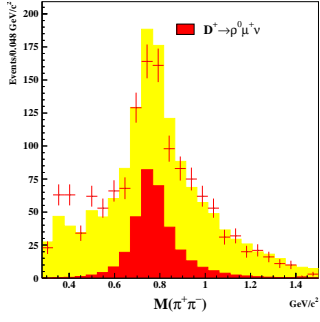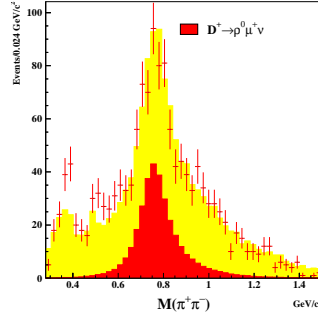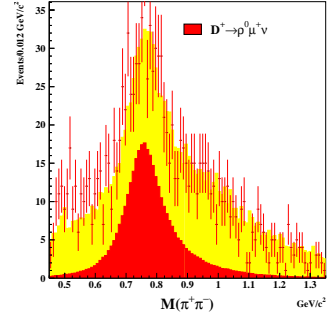
(a) 25 Bins   (b) 50 Bins   (c) $0.45 < M(\pi\pi) < 1.35$

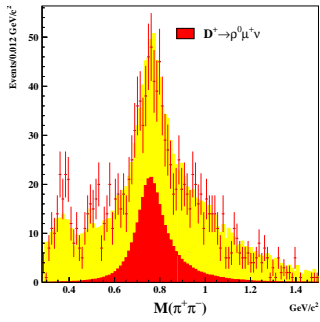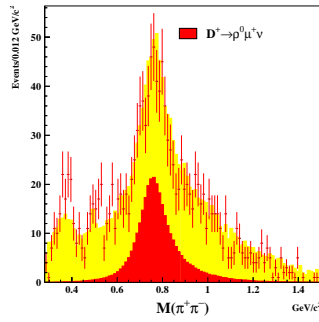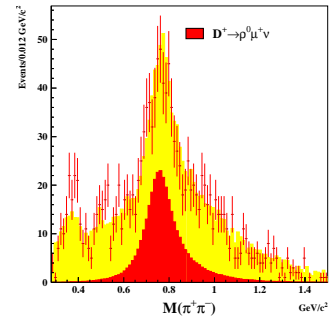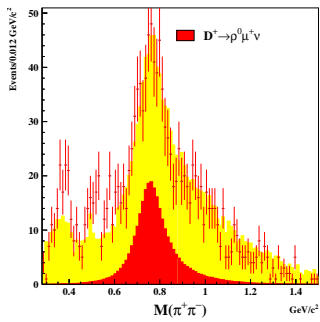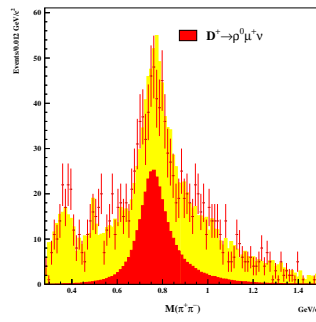(d) $2 \times \overline{K}^{*0}$ yield   (e) $1/2 \times \overline{K}^{*0}$ yield   (f) D_s shapes BR $+ 3\sigma$
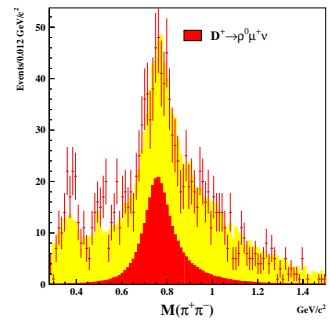
(g) D_s BR $- 3\sigma$ (h) Combinatorial shape   (i) No penalty term

Figure V.7: Fit results for fit variant systematics.

Table V.3: Variations used to assess the systematic uncertainty due to our fitting choices.

Fit Variation	$D^+ \to \rho^0 \mu^+ \nu$ Yield	$\frac{\Gamma(D^+ \to \rho^0 \mu^+ \nu)}{\Gamma(D^+ \to \overline{K}^{*0} \mu^+ \nu)}$
25 bins	323 ± 44	0.0417 ± 0.0058
50 bins	323 ± 44	0.0417 ± 0.0057
$0.45 < M(\pi\pi) < 1.35$	354 ± 50	0.0459 ± 0.0066
$2 \times \overline{K}^{*0}$	321 ± 43	0.0411 ± 0.0056
$1/2 \times \overline{K}^{*0}$	318 ± 43	0.0408 ± 0.0056
D_s ind. shapes	333 ± 43	0.0429 ± 0.0056
D_s ind. shapes BR $+3\sigma$	346 ± 43	0.0446 ± 0.0056
D_s ind. shapes BR -3σ	284 ± 44	0.0366 ± 0.0057
Combinatorial shape	379 ± 43	0.0489 ± 0.0057
No penalty term	314 ± 43	0.0432 ± 0.0067
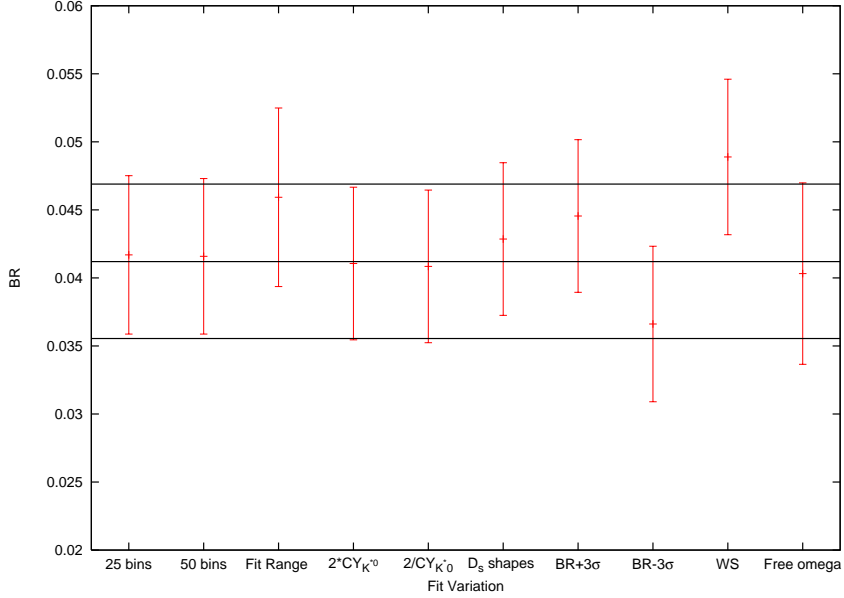
Figure V.8: $\frac{\Gamma(D^+ \to \rho^0 \mu^+ \nu)}{\Gamma(D^+ \to \overline{K}^{*0} \mu^+ \nu)}$ for fit systematic studies. The solid lines represent the fit result for the standard fitting procedure.

split the sample according to the $D^\pm$ charge. The final split–sample was done to examine two different detector configurations. For roughly 30% of the data taking period the target did not have the interleaved silicon detectors (TSSD). Therefore, we split our sample according to the run number. Run numbers greater than 9750 represent the period when the TSSD was in place and operational.

By splitting our sample we have effectively reduced the statistics by about a factor of two. In order to assess any systematic uncertainty present we need to distinguish between deviations caused by pure statistical effects from those that are associated with something in the data that we don't understand. To achieve this, FOCUS uses a technique based on the "Scale factor" method used by the PDG [10] to average different experimental results when the $\chi^2/(\text{N-1})$ obtained from the weighted average of these N results is somewhat larger than one. When this is the case, the errors are increased by a factor S defined as

$$S = \sqrt{\chi^2/(\text{N - 1})}. \tag{V.3}$$

The procedure used by FOCUS to assess systematic uncertainties with split–samples is as follows [38]. First, the weighted average of the N independent sub-samples $< x >$ is defined as

$$< x >= \frac{\sum_i x_i/\sigma_i^2}{\sum_i 1/\sigma_i^2} \tag{V.4}$$

where x_i is the branching fraction ratio result for the ith sub-sample and σ_i is the statistical uncertainty on it. The statistical error for the weighted average is then

$$< \sigma >= \frac{1}{\sum_i 1/\sigma_i^2}. \tag{V.5}$$

The χ^2 is then calculated.

$$\chi^2 = \sum_i^{\text{N}} \frac{(< x > -x_i)^2}{\sigma_i^2} \tag{V.6}$$

If $\chi^2/(\text{N - 1})$ is greater than 1 then we increase the statistical error of the weighted average by a scale factor equal to $\sqrt{\chi^2/(\text{N - 1})}$. The scaled error, $\widetilde{\sigma}$, is then

$$\widetilde{\sigma} =< \sigma > \sqrt{\chi^2/(\text{N - 1})}. \tag{V.7}$$

Armed with the scaled error $\widetilde{\sigma}$, we can compare it to the statistical error of the un-split sample to check for evidence of any systematic uncertainty. Specifically, we quote a systematic error if $\widetilde{\sigma}$ is greater than the statistical error of the un–split sample. The quoted systematic error is

$$
\sigma_{syst} = \sqrt{\widetilde{\sigma}^2 - \sigma^2} \quad \text{if} \quad \widetilde{\sigma} > \sigma
$$
$$
\sigma_{syst} = 0 \quad \text{if} \quad \widetilde{\sigma} \leq \sigma
$$
(V.8)

where σ is the statistical error of the un–split sample.

Table V.4: Yields and branching ratios for the sub–samples used in split sample test.

Split Sample	$D^+ \to \rho^0 \mu^+ \nu$ Yield	$\frac{\Gamma(D^+ \to \rho^0 \mu^+ \nu)}{\Gamma(D^+ \to \overline{K}^{*0} \mu^+ \nu)}$
$D_p > 85$ GeV$/c$	120 ± 27	0.039 ± 0.008
$D_p > 85$ GeV$/c$	227 ± 35	0.040 ± 0.007
D^+	146 ± 30	0.038 ± 0.008
D^-	172 ± 32	0.049 ± 0.008
Run Number > 9750	222 ± 37	0.041 ± 0.007
Run Number < 9750	117 ± 25	0.049 ± 0.011

The results for this test are presented in Table V.4 and plotted in Figure V.9. It is clear that the results for the three split–samples are consistent with the results obtained using the complete data set. We conclude that our Monte Carlo simulation correctly reproduces the two main data taking conditions and does a very good job in simulating the charm production mechanisms. No additional systematic uncertainty contribution was indicated by this search.

With the three sources of systematic uncertainties considered we can now assess the total systematic uncertainty for the branching fraction ratio. For this we added the individual contributions in quadrature as summarized in Table V.5. We quote our final result to be

$$
\frac{\Gamma(D^+ \to \rho^0 \mu^+ \nu)}{\Gamma(D^+ \to \overline{K}^{*0} \mu^+ \nu)} = 0.0412 \pm 0.0057 \pm 0.0040.
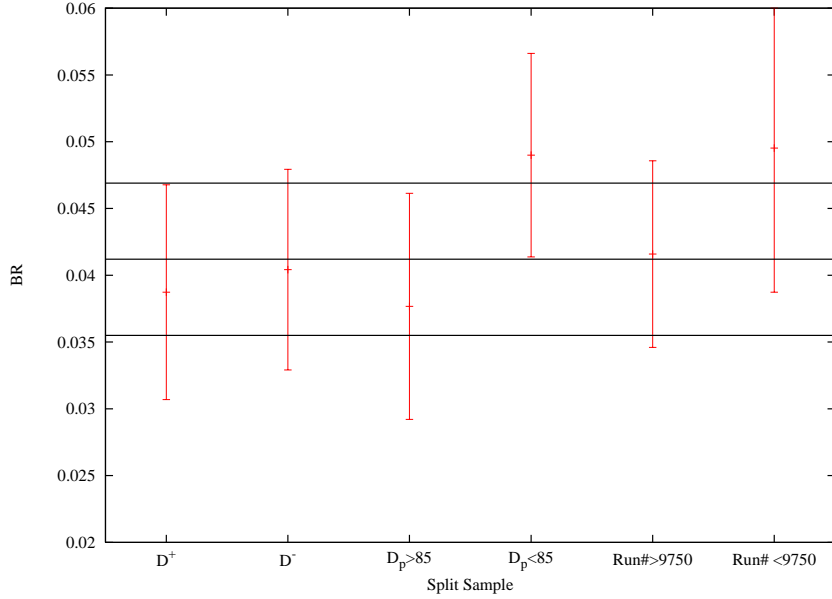$$

114

Figure V.9: $\frac{\Gamma(D^+\to\rho^0\mu^+\nu)}{\Gamma(D^+\to\overline{K}^{*0}\mu^+\nu)}$ branching fraction ratio for the split–sample systematic test. The branching fraction ratio for each sub-sample is consistent with the results from the complete sample (solid line). No systematic uncertainty is evident.

Table V.5: Sources of systematic uncertainties. The three sources are added in quadrature to obtain the total systematic uncertainty.

Systematic Source	Error
Cut Variations	0.0023
Fit Variations	0.0033
Split Sample	negligible
Total	0.0040

V.2   Comparison with Theoretical Models and Previous Experiments

In this section we compare the results obtained in this analysis with some theoretical expectations and other experimental results.

Until recently, the few experiments which measured of the relative branching fraction ratio, $D^+ \to \rho^0\mu^+\nu$, observed very few events resulting in measurements with large uncertainties. This lead to a world average value of 0.061 ± 0.014 [10]. Just before this analysis was published, the CLEO-c collaboration published their measurement of the absolute branching fraction, $\Gamma(D^+ \to \rho^0 e^+\nu)$, using a sample with integrated luminosity of 55.8 pb^{-1} [34]. Results from several experiments are presented in Table V.6 and

Figure V.10. With the addition of our result, the new world average for the muonic mode becomes 0.045 ± 0.007 [1].

Table V.6: Experimental results for the branching ratio. Statistical and systematic errors have been added in quadrature.

Reference	Yield	$\frac{\text{BR}(D^+ \to \rho^0 \mu^+ \nu)}{\text{BR}(D^+ \to \overline{K}^{*0} \mu^+ \nu)}$	$\frac{\text{BR}(D^+ \to \rho^0 e^+ \nu)}{\text{BR}(D^+ \to \overline{K}^{*0} e^+ \nu)}$
E653 [39]	$4.0 \pm^{2.8}_{2.3}$	$0.044^{+0.034}_{-0.029}$	
E687 [40]	39 ± 9	0.079 ± 0.023	
E791 [41]	103 ± 25	0.051 ± 0.017	0.045 ± 0.017
CLEO [34]	27.4 ± 5.7		0.038 ± 0.008
This result	320 ± 44	0.041 ± 0.007	
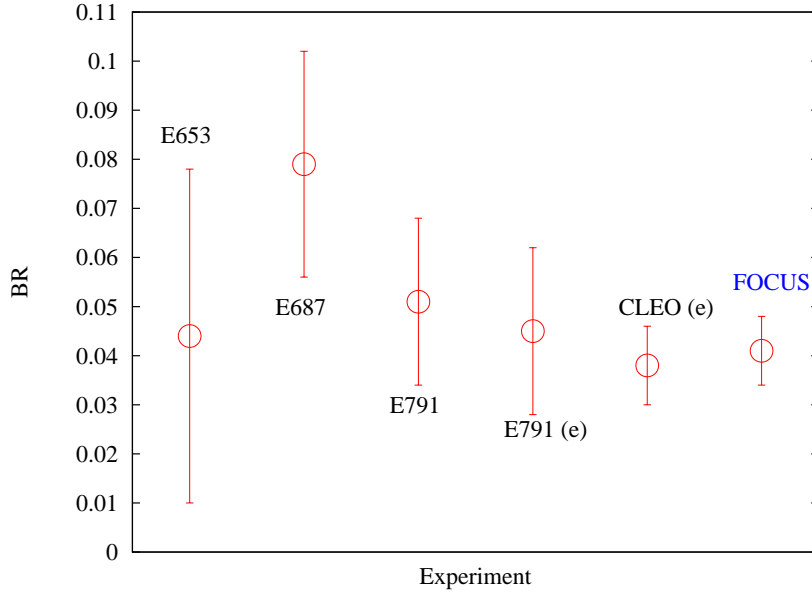
Figure V.10: Summary of experimental results for BR($D^+ \to \rho^0 \ell^+ \nu$)/BR($D^+ \to \overline{K}^{*0} \ell^+ \nu$). Statistical and systematic errors have been added in quadrature.

Many theoretical models have been used to predict the values for the relative branching fractions and decay widths of heavy to light semileptonic decays. Nonetheless, predictions based on the quark model (QM), Sum Rules (SR), Lattice QCD (LQCD), etc, differ significantly. The large uncertainty in the $D^+ \to \rho^0 \ell^+ \nu$ branching fraction made it hard to distinguish between competing models. With the improvement in the determination of the $D^+ \to \rho^0 \ell^+ \nu$ branching fraction we reduce some of the ambiguity. Some of the predictions made in the context of the different models are presented in Table V.7. In order to fully

compare our result to the theoretical predictions we have calculated the partial decay width from our $D^+ \to \rho^0 \mu^+ \nu$ result, the FOCUS measurement of the ratio $\frac{\Gamma(D^+ \to \overline{K}^{*0} \mu^+ \nu)}{\Gamma(D^+ \to K^- \pi^+ \pi^+)}$ [37], the PDG [10] value of the absolute branching fraction of the decay $D^+ \to K^- \pi^+ \pi^+$, and the FOCUS measurement of the D^+ lifetime [42].

$$\Gamma(D^+ \to \rho^0 \mu^+ \nu) = \frac{\Gamma(D^+ \to \rho^0 \mu^+ \nu)}{\Gamma(D^+ \to \overline{K}^{*0} \mu^+ \nu)} \frac{\Gamma(D^+ \to \overline{K}^{*0} \mu^+ \nu)}{\Gamma(D^+ \to K^- \pi^+ \pi^+)} \frac{BR(D^+ \to K^- \pi^+ \pi^+)}{\tau_{D^+}}$$

(V.9)

where $\frac{\Gamma(D^+ \to \overline{K}^{*0} \mu^+ \nu)}{\Gamma(D^+ \to K^- \pi^+ \pi^+)} = 0.602 \pm 0.023$, $BR(D^+ \to K^- \pi^+ \pi^+) = (0.922 \pm 0.21)\%$, and $\tau_{D^+} = (1039.4 \pm 4.3)10^{-15}s$. Using the above values along with our result we obtained

$$\Gamma(D^+ \to \rho^0 \mu^+ \nu) = (0.22 \pm 0.03 \pm 0.02 \pm 0.01) \times 10^{10} \text{ s}^{-1}$$

where the last error is a combination of the uncertainties on the quantities not measured in this work.

In Table V.7 we compare the results obtained in this thesis with the predictions made using the different theoretical approaches. These results are shown graphically in Figure V.11. In this figure, we have also plotted the weighted average of the muonic and electronic mode world averages from the latest PDG [1]. In Figure V.12 a comparison with the predicted partial decay is presented. Although the statistical error is too large to discriminate against most models, the data indicates that the QCD Sum Rule predictions for $D^+ \to \rho^0 \ell^+ \nu$ [43, 44] are too low.

Table V.7: Theoretical predictions for the branching ratio and partial decay width. Most of the theoretical predictions are calculated for $D^0 \rightarrow \rho^- \ell^+ \nu$. To compare these predictions with our result, we have used the isospin conjugate relation $\Gamma(D^+ \rightarrow \rho^0 \ell^+ \nu) = 1/2\ \Gamma(D^0 \rightarrow \rho^- \ell^+ \nu)$.

Reference	ℓ	$\dfrac{\mathrm{BR}(D^+ \rightarrow \rho^0 \ell^+ \nu)}{\mathrm{BR}(D^+ \rightarrow \overline{K}^{*0} \ell^+ \nu)}$	$\Gamma(D^+ \rightarrow \rho^0 \ell^+ \nu)(10^{10}\ s^{-1})$
Ball [43] (SR)	e		0.06 ± 0.02
APE [45] (LQCD)	ℓ	0.043 ± 0.018	0.3 ± 0.1
Jaus [46] (QM)	ℓ	0.030	0.16
ISGW2 [47] (QM)	e	0.023	0.12
Yang–Hwang [44] (SR)	e	0.018 ± 0.005	$0.07^{+0.04}_{-0.02}$
O'Donnell–Turan [48] (LF)	μ	0.025	
Melikhov [49] (QM)	ℓ	$0.027, 0.024$	$0.15, 0.13$
Ligeti–Stewart–Wise [50]	ℓ	0.044	
Kondratyuk-Tchein [51] (LF)	ℓ	$0.035, 0.033, 0.033, 0.032$	$0.19, 0.20, 0.18, 0.19$
Melikhov–Stech [52] (QM)	ℓ	0.035	0.21
Wang–Wu–Zhong [24] (LC)	ℓ	0.035 ± 0.011	0.17 ± 0.04
Fajfer–Kamenik [53]	ℓ	0.045	0.25
This result	μ	0.041 ± 0.007	0.22 ± 0.04
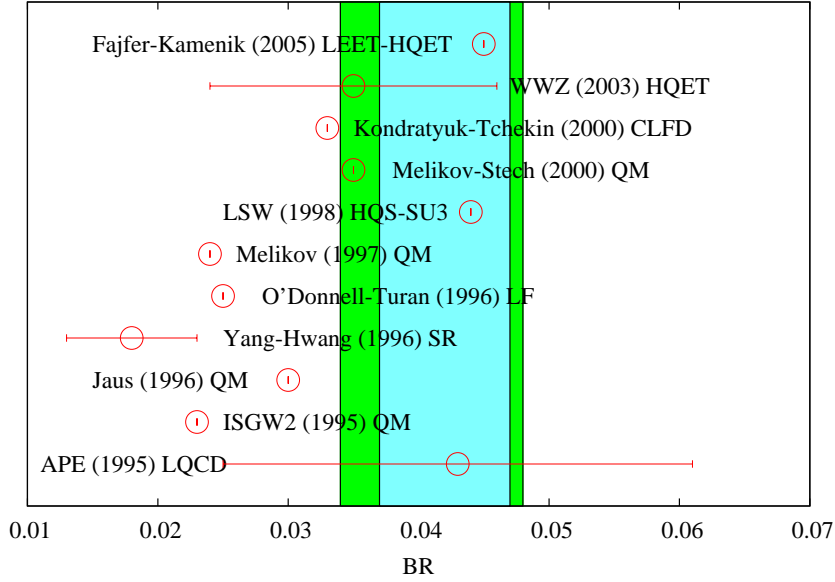
Figure V.11: Summary of BR($D^+ \rightarrow \rho^0 \ell^+ \nu$)/BR($D^+ \rightarrow \overline{K}^{*0} \ell^+ \nu$). The green stripe represents the results obtained in this work, while the blue stripe represents the result of combining the world average for the electronic and muonic modes.
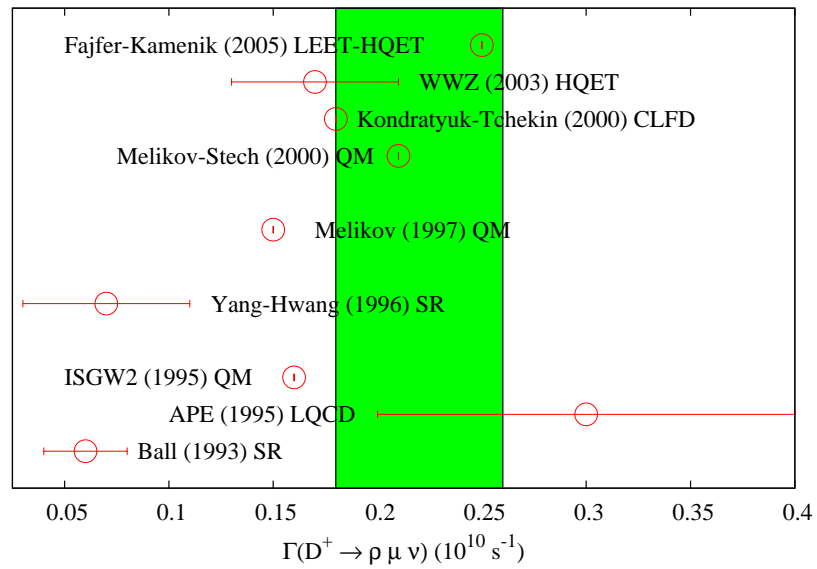
Figure V.12: Summary of $\Gamma(D^+ \to \rho^0 \ell^+ \nu)$ predictions compared to the results obtained in this work (green stripe).

CHAPTER VI

KINEMATIC VARIABLES

The $D^+ \rightarrow \rho^0 \mu^+ \nu$ form factors have never been measured before. There are two main reasons for this, the lack of statistics so far observed due to being a Cabibbo suppressed decay, and the presence of irreducible backgrounds under the signal area. Using the FOCUS data we studied the feasibility of doing such a measurement for the first time. In this chapter we describe this effort.

As mentioned in Section I.4.3 the decay of a D meson into a vector meson ($D \rightarrow V \ell \nu$) decaying into two pseudo–scalar mesons is described by four kinematic variables: q^2, the square of the $\ell \nu$ mass, and three angles, θ_V, the angle between the D meson and one of the pseudo–scalar mesons in the parent vector rest frame, θ_ℓ, the angle between the D meson and the charged lepton in the $\ell \nu$ rest frame, and χ, the angle between the two decay planes. Using these definitions the differential decay rate can be written in terms of three helicity basis form factors, H_0, and $H_\pm$ (see (I.29)). By studying the angular dependence the form factors can be measured. [1]

The first step is then, the determination of these kinematic variables. This is not trivial since the missing neutrino makes it impossible to fully reconstruct the momentum of the D meson. Nonetheless, the D momentum can be reconstructed up to a two–fold ambiguity as described below.

Using four–vector notation, the semileptonic decay of a D meson can be written as

$$\tilde{D} = \tilde{c} + \tilde{\nu}.$$

---

[1]Typically, experiments report the ratio of form factors $r_v \equiv \frac{V(0)}{A_1(0)}$, $r_2 \equiv \frac{A_2(0)}{A_1(0)}$, and $r_3 \equiv \frac{A_3(0)}{A_1(0)}$.

Squaring both sides yields

$$M_D^2 = m_c^2 + 2E_c E_\nu - 2\mathbf{p}_c \cdot \mathbf{p}_\nu.$$

Along the D line of flight, $\hat{p}_D$, the momentum of the D can be decomposed as the sum of the neutrino momentum, $\mathbf{p}_\nu$ and the momentum of the charged particles, $\mathbf{p}_c = \mathbf{p}_{h^+} + \mathbf{p}_{h^-} + \mathbf{p}_\mu$. The magnitude of the D momentum can then be calculated in a boosted frame where the momentum of the charged system is perpendicular to $\hat{p}_D$. In this frame

$$\mathbf{p}'_{c_\perp} = -\mathbf{p}'_{\nu_\perp}$$

and

$$\mathbf{p}'_{\nu_\parallel} = \mathbf{p}'_D$$

where the primed variables denote the boosted frame. The energy of the neutrino becomes

$$E'_\nu = \frac{M_D^2 - m_c^2 - 2|\mathbf{p}'_{c_\perp}|^2}{2E'_c}. \tag{VI.1}$$

The squared of longitudinal component of the neutrino momentum is

$$|\mathbf{p}'^2_{\nu_\parallel}| = E'^2_\nu - |\mathbf{p}'_{c_\perp}|^2. \tag{VI.2}$$

This implies a two–fold ambiguity reflecting the fact that we only know the magnitude of $\mathbf{p}'_D$, but not its direction. Solving for $\mathbf{p}'_D$ in (VI.2) and boosting back to the laboratory frame yields a high momentum and a low momentum solution. These two solutions should be equally valid.

In cases where we need $\mathbf{p}_D$, such as when boosting the momentum of the ρ^0 and the D^+ to the ρ^0 frame in order to calculate $\cos\theta_v$, we used the solution that yields the lower momentum and assume that $\hat{p}_D$ has the same direction as the length vector, $\mathbf{L}$,

pointing from the primary to the secondary vertex. Studies using Monte Carlo generated charmed semileptonic decays indicate that this solution matches better the generated D momentum as shown in Figure VI.1. This can be better appreciated when we compare the D momentum reconstruction resolution, defined as the difference the generated and reconstructed momentum, shown in Figure VI.2.
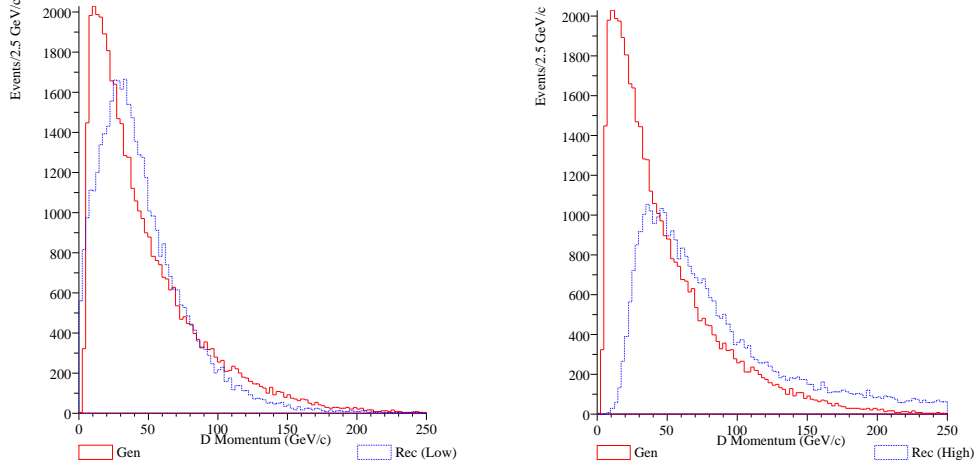
(a) Generated D momentum vs reconstructed low momentum solution

(b) Generated D momentum vs reconstructed high momentum solution

Figure VI.1: High and low reconstructed D momentum solutions compared to the generated momentum.

We are now in position to boost the necessary vectors to the different C.M. frames and calculate the kinematic variables. These variables are shown in Figure VI.3 for a Monte Carlo generated sample and Figure VI.4 for real $D^+ \to \rho^0 \mu^+ \nu$ data. The cuts applied to get these distributions are the same cuts used to measure the relative branching fraction $\frac{\Gamma(D^+ \to \rho^0 \mu^+ \nu)}{\Gamma(D^+ \to \overline{K}^{*0} \mu^+ \nu)}$. Looking at the $\cos \theta_V$ distribution, it is clear that the background present in the data must be reduced significantly in order to extract any meaningful physics out of it.

The results of the $M(\pi^+ \pi^-)$ fit indicate that the major background contributions arise from muon misidentification and combinatorial. Combinatorial background can be reduced by requiring tighter cuts on the secondary vertex confidence level, while the muon misidentification can be further reduced by requiring harder cuts on the muon identification
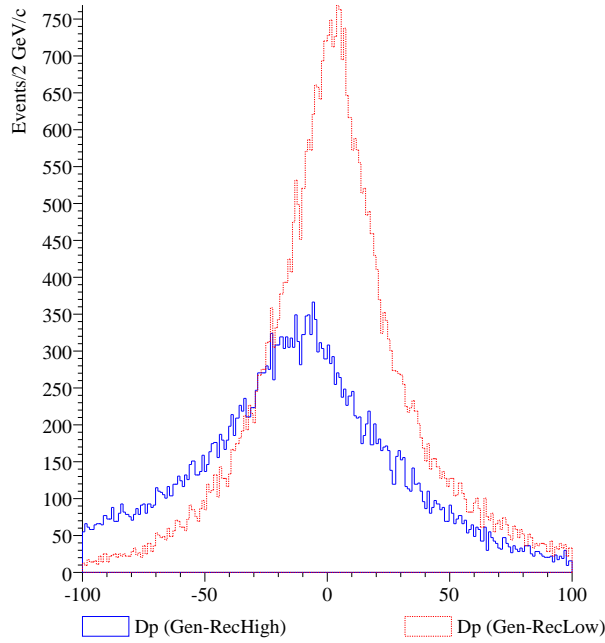
Figure VI.2: D momentum resolution, measured as the difference between the generated momentum and the reconstructed momentum for a charmed semileptonic decay. The blue histogram represents the resolution for the high momentum solution, while the red histogram represent the resolution for the low momentum solution. Both solutions are calculated per event.

confidence level and muon momentum. Therefore, we required that the secondary vertex form a good vertex with a confidence level exceeding 25%. Furthermore, we required that the muon track had a confidence level greater than 25% and momentum greater than 35 GeV/c.

A first step in trying to reduce the background is to cut hard around the ρ^0 peak, $0.62 < M(\pi^+\pi^-) < 0.92$MeV. This cut eliminates all contribution from $D^+ \rightarrow \overline{K}^0\mu^+\nu$, as well as the high multiplicity decay modes from the D_s^+. The main semileptonic contributions are then $D_s^+ \rightarrow \eta\prime(\rho^0\gamma)\mu^+\nu$, $D_s^+ \rightarrow \phi(\rho^0\pi^0)\mu^+\nu$, and $\overline{K}^{*0}$. We know that we can further reduce the $\overline{K}^{*0}$ contamination by cutting harder on the pionicity of the pion with opposite charge as the muon; we made this requirement greater than 7 units of log likelihood. The other two semileptonic contributions are harder to reduce since they include a ρ^0 and will peak under the signal.
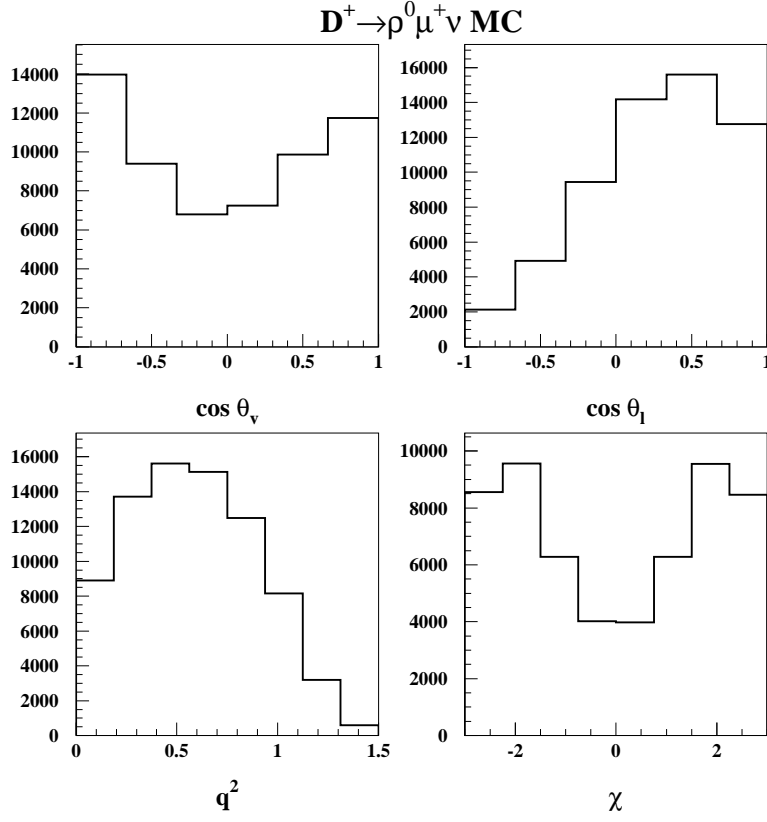
Figure VI.3: Kinematic variable distributions for $D^+ \to \rho^0 \mu^+ \nu$ Monte Carlo generated events. The cuts applied to obtained these distributions are the standard cuts used in the determination of $\frac{\Gamma(D^+ \to \rho^0 \mu^+ \nu)}{\Gamma(D^+ \to \overline{K}^{*0} \mu^+ \nu)}$.

These cuts are very effective in reducing both the combinatorial and muon misidentification backgrounds at the expense of a drastically reduction of the available statistics as shown in Figure VI.5.

The 52 ± 12 events returned by the fit represents, statistically, a sample of $\sim 16 \pm 4$ pure $D^+ \to \rho^0 \mu^+ \nu$ events [2]. The question we can ask is: How well can we measure the form factor ratios $R_v \equiv \frac{V(0)}{A_1(0)}$ and $R_2 \equiv \frac{A_2(0)}{A_1(0)}$ given the low number of observed events. The question can be answered by looking at how well, given the q^2 resolution in FOCUS, other low statistics $D \to V \ell \nu$ form factors have been measured.

---

[2]The branching fraction obtained with this cut set is in very good agreement with the results presented in this thesis.
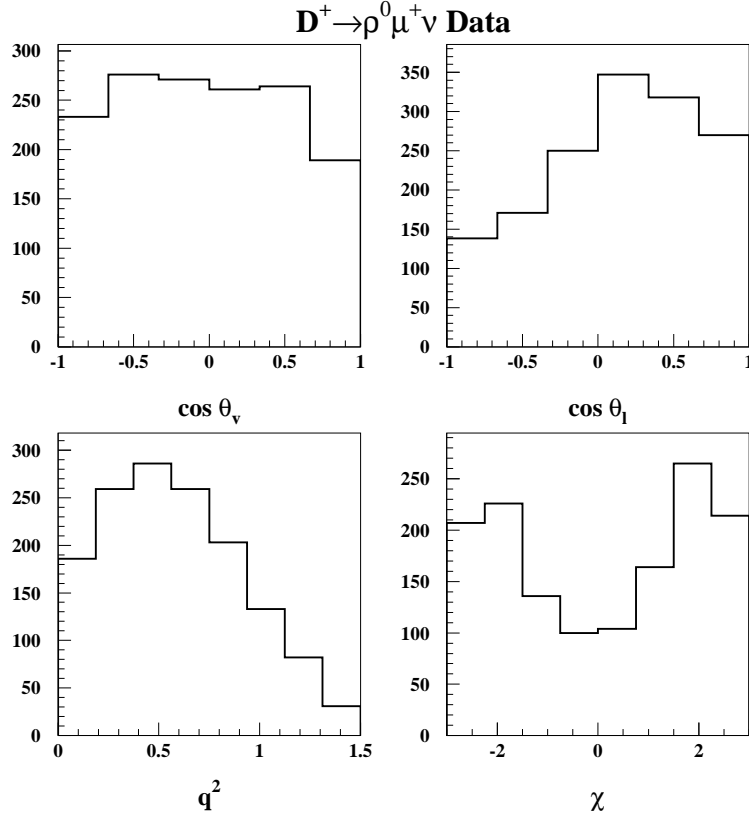
Figure VI.4: Kinematic variable distributions for real $D^+ \rightarrow \rho^0 \mu^+ \nu$ events. The cuts applied to obtained these distributions are the standard cuts used in the determination of $\frac{\Gamma(D^+ \rightarrow \rho^0 \mu^+ \nu)}{\Gamma(D^+ \rightarrow \overline{K}^{*0} \mu^+ \nu)}$.

FOCUS has measured the form factor ratios R_v and R_2 for the decay modes $D^+ \rightarrow$ $\overline{K}^{*0} \mu^+ \nu$ [54], $D_s^+ \rightarrow \phi \mu^+ \nu$ [55], and $D^0 \rightarrow \overline{K}^{*-} \mu^+ \nu$ [56]. Of these, the form factor measurement for $D^0 \rightarrow \overline{K}^{*-} \mu^+ \nu$ was done with 175 ± 17 events, equivalent to $\sim 100 \pm 10$ perfect events. The measurement yielded $R_v = 1.706 \pm 0.677 \pm 0.342$ and $R_2 = 0.912 \pm 0.370 \pm 0.104$ where the second error is the statistical uncertainty. From these statistical errors and the fact that the our statistical error would be a factor of $\sqrt{N}$ larger, where $N \sim 6$, we conclude that such a measurement would not yield a significant result.

Nonetheless, we can compare the kinematic variable distributions obtained from the data with the distributions obtained from our Monte Carlo simulated events. As mentioned before, our $D^+ \rightarrow \rho^0 \mu^+ \nu$ Monte Carlo events were generated using the same form factor

Table VI.1: Contributions to the $M(\pi^+\pi^-)$ fit histogram with tight cuts used to extract the kinematic variables.

Signal	Total Yield	Events Under Signal Area
$D^+ \to \rho^0 \mu^+ \nu$	52 ± 12	49
$\overline{K}^{*0}, K/\pi$ Mis-id	6	5
$D^+ \to \overline{K}^0 \mu^+ \nu$	5 ± 3	0
D_s^+ modes total	45 ± 11	21
$D^+ \to \omega \mu^+ \nu$	15 ± 4	2
Muon Mis-Id	~ 0	~ 0
Combinatorial	~ 0	~ 0
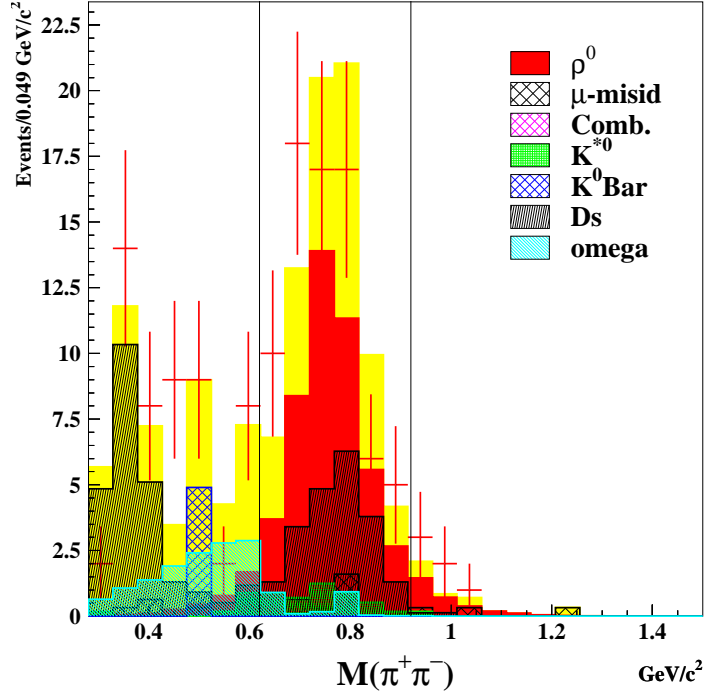
Figure VI.5: $M(\pi^+\pi^-)$ fit using tight cuts. The vertical lines represent the mass window cut used in the kinematic distributions. The resulting branching fraction ratio obtained with these cuts is consistent with our quoted result.

ratios describing the $D^+ \to \overline{K}^{*0} \mu^+ \nu$ decay mode, but with the vector and axial masses changed to reflect the $c \to d$ transition. The three kinematic variables that determine the R_v and R_2 form factors, $\cos\theta_v$, $\cos\theta_\ell$, and q^2 are shown in Figure VI.6. No deviation from the assumed form factors can be seen in our data.

(a) $\cos\theta_v$
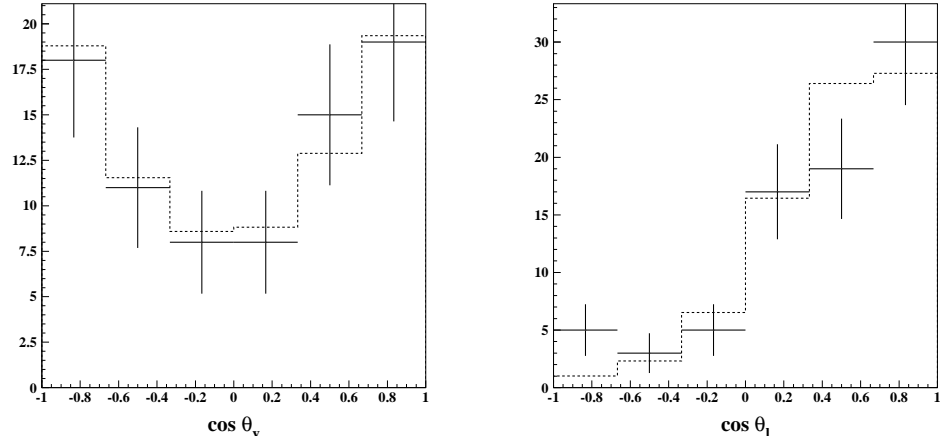
(b) $\cos\theta_\ell$
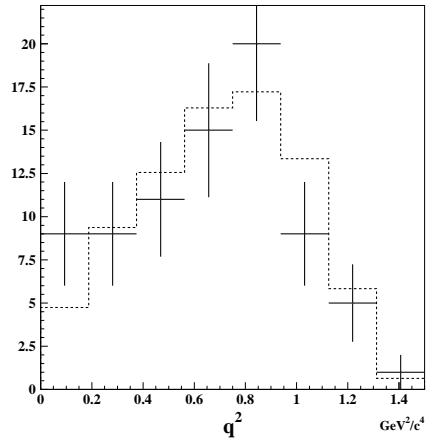
(c) q^2

Figure VI.6: Comparison of the $D^+ \rightarrow \rho^0\mu^+\nu$ kinematic variables for data (solid histogram) and MC generated events (dashed). The Monte Carlo distributions were normalized to the same number of events as the data. The MC events assumed the $D^+ \rightarrow \rho^0\mu^+\nu$ form factors to be similar to the $D^+ \rightarrow \overline{K}^{*0}\mu^+\nu$ form factors.

CHAPTER VII

SUMMARY AND CONCLUSIONS

In this thesis we presented the measurement of the branching fraction ratio of the Cabibbo suppressed semileptonic decay mode $D^+ \rightarrow \rho^0 \mu^+ \nu$ with respect to the Cabibbo favored mode $D^+ \rightarrow \overline{K}^{*0} \mu^+ \nu$ using data collected by the FOCUS collaboration. We used a binned maximum log–likelihood fit that included all known semileptonic backgrounds as well as combinatorial and muon misidentification backgrounds to extract the yields for both the signal and normalization modes. We reconstructed 320 ± 44 $D^+ \rightarrow \rho^0 \mu^+ \nu$ events and 11372 ± 161 $D^+ \rightarrow K^- \pi^+ \mu^+ \nu$ events. Taking into account the non–resonant contribution to the $D^+ \rightarrow K^- \pi^+ \mu^+ \nu$ yield due to a s–wave interference first measured by FOCUS the branching fraction ratio is:

$$\frac{\Gamma(D^+ \rightarrow \rho^0 \mu^+ \nu)}{\Gamma(D^+ \rightarrow \overline{K}^{*0} \mu^+ \nu)} = 0.0412 \pm 0.0057 \pm 0.0040 \qquad \text{(VII.1)}$$

where the first error is statistical and the second error is the systematic uncertainty. This represents a substantial improvement over the previous world average. More importantly, the new world average for $\frac{\Gamma(D^+ \rightarrow \rho^0 \mu^+ \nu)}{\Gamma(D^+ \rightarrow \overline{K}^{*0} \mu^+ \nu)}$ along with the improved measurements in the electronic mode can be used to discriminate among different theoretical approaches that aim to understand the hadronic current involved in the charm to light quark decay process. The average of the electronic and muonic modes indicate that predictions for the partial decay width $\Gamma(D^+ \rightarrow \rho^0 \ell^+ \nu)$ and the ratio $\frac{\Gamma(D^+ \rightarrow \rho^0 \ell^+ \nu)}{\Gamma(D^+ \rightarrow \overline{K}^{*0} \ell^+ \nu)}$ based on Sum Rules are too low [43, 44].

Using the same data used to extract $\frac{\Gamma(D^+ \rightarrow \rho^0 \mu^+ \nu)}{\Gamma(D^+ \rightarrow \overline{K}^{*0} \mu^+ \nu)}$ we studied the feasibility of measuring the form factors for the $D^+ \rightarrow \rho^0 \mu^+ \nu$ decay. We found that the need to further reduce the combinatorial and muon misidentification backgrounds left us with a

much smaller sample of 52 ± 12 $D^+ \rightarrow \rho^0 \mu^+ \nu$ events; not enough to make a statistically significant measurement of the form factors.

REFERENCES

[1] C. Amsler et al. (Particle Data Group), "Review of Particle Physics," *Phys. Lett.* **B667** (2008) 1+.

[2] G. Hao, C.-F. Qiao, and A.-L. Zhang, "0^{+-} Trigluon Glueball and its Implication for a Recent BES Observation," *Phys. Lett.* **B642** (2006) 53–61, `arXiv:hep-ph/0512214`.

[3] N. Kochelev and D.-P. Min, "X(1835) as the Lowest Mass Pseudoscalar Glueball and Proton Spin Problem," *Phys. Lett.* **B633** (2006) 283–288, `arXiv:hep-ph/0508288`.

[4] V. V. Anisovich and A. V. Sarantsev, "Observation of Tensor Glueball in the Reactions $p\overline{p} \to \pi\pi, \eta\eta, \eta\eta'$," *JETP Lett.* **81** (2005) 417–423, `arXiv:hep-ph/0504106`.

[5] W. N. Cottingham and D. A. Greenwood, *An Introduction to the Standard Model of Particle Physics*. Cambridge University Press, 1998.

[6] S. L. Glashow, "Partial Symmetries of Weak Interactions," *Nucl. Phys.* **22** (1961) 579–588.

[7] S. Weinberg, "A Model of Leptons," *Phys. Rev. Lett.* **19** (1967) 1264–1266.

[8] U. Amaldi, W. de Boer, and H. Furstenau, "Comparison of Grand Unified Theories with Electroweak and Strong Coupling Constants Measured at LEP," *Phys. Lett.* **B260** (1991) 447–455.

[9] W. de Boer and C. Sander, "Global Electroweak Fits and Gauge Coupling Unification," *Phys. Lett.* **B585** (2004) 276–286, `arXiv:hep-ph/0307049`.

[10] **Particle Data Group** Collaboration, W. M. Yao *et al.*, "Review of Particle Physics," *J. Phys.* **G33** (2006) 1+.

[11] N. Cabibbo, "Unitary Symmetry and Leptonic Decays," *Phys. Rev. Lett.* **10** (1963) 531–532.

[12] C. G. Boyd, B. Grinstein, and R. F. Lebed, "Precision Corrections to Dispersive Bounds on Form Factors," *Phys. Rev.* **D56** (1997) 6895–6911, `arXiv:hep-ph/9705252`.

[13] M. Gell-Mann, "A Schematic Model of Baryons and Mesons," *Phys. Lett.* **8** (1964) 214–215.

[14] S. L. Glashow, J. Iliopoulos, and L. Maiani, "Weak Interactions with Lepton-Hadron Symmetry," *Phys. Rev.* **D2** (1970) 1285–1292.

[15] **E–598** Collaboration, J. J. Aubert *et al.*, "Experimental Observation of a Heavy Particle J," *Phys. Rev. Lett.* **33** (1974) 1404–1406.

[16] J. E. Augustin *et al.*, "Discovery of a Narrow Resonance in $e + e-$ Annihilation," *Phys. Rev. Lett.* **33** (1974) no. 23, 1406–1408.

[17] M. Wirbel, B. Stech, and M. Bauer, "Exclusive Semileptonic Decays of Heavy Mesons," *Z. Phys. C* **29** (1985) 637.

[18] J. D. Richman and P. R. Burchat, "Leptonic and Semileptonic Decays of Charm and Bottom Hadrons," *Rev. Mod. Phys.* **67** (1995) 893–976, `arXiv:hep-ph/9508250`.

[19] **FOCUS** Collaboration, J. M. Link *et al.*, "Measurements of the q^2 Dependence of the $D^0 \to K^- \mu^+ \nu$ and $D^0 \to \pi^- \mu^+ \nu$ Form Factors," *Phys. Lett.* **B607** (2005) 233–242, `arXiv:hep-ex/0410037`.

[20] **Fermilab Lattice** Collaboration, C. Aubin *et al.*, "Semileptonic Decays of D Mesons in Three-Flavor Lattice QCD," *Phys. Rev. Lett.* **94** (2005) 011601, `arXiv:hep-ph/0408306`.

[21] **FOCUS** Collaboration, J. M. Link *et al.*, "Evidence for New Interference Phenomena in the Decay $D^+ \to K^- \pi^+ \mu^+ \nu$," *Phys. Lett.* **B535** (2002) 43–51, `arXiv:hep-ex/0203031`.

[22] **FOCUS** Collaboration, J. M. Link *et al.*, "Hadronic Mass Spectrum Analysis of $D^+ \to K^- \pi^+ \mu^+ \nu$ Decay and Measurement of the $\overline{K}^{*0}$ (892) Mass and Width," *Phys. Lett.* **B621** (2005) 72–80, `arXiv:hep-ex/0503043`.

[23] M. R. Shepherd et al., "Model Independent Measurement of Form Factors in the Decay $D^+ \to K^- \pi^+ e^+ \nu$," *Phys. Rev. D* **74** (2006) 052001.

[24] W. Y. Wang, Y. L. Wu, and M. Zhong, "Heavy to Light Meson Exclusive Semileptonic Decays in Effective Field Theory of Heavy Quarks," *Phys. Rev. D* **67** (2003) no. 1, 014024.

[25] **E–687** Collaboration, P. L. Frabetti *et al.*, "Description and Performance of the Fermilab E687 Spectrometer," *Nucl. Instrum. Meth.* **A320** (1992) 519–547.

[26] J. M. Link *et al.*, "The Target Silicon Detector for the FOCUS Spectrometer," *Nucl. Instrum. Meth.* **A516** (2004) 364–376, `arXiv:hep-ex/0204023`.

[27] Richard Fernow, *Introduction to Experimental Particle Physics*. Cambridge University Press, 1986.

[28] S. Bianco *et al.*, "The Upgraded Outer EM Calorimeter of FOCUS at Fermilab ," `arXiv:hep-ex/9912066`.

[29] **FOCUS** Collaboration, V. Arena *et al.*, "Description and Performance of the FOCUS (E831) Hadron Calorimeter," *Nucl. Instrum. Meth.* **A434** (1999) 271–278.

[30] T. Sjostrand *et al.*, "High-energy-physics event generation with PYTHIA 6.1," *Comput. Phys. Commun.* **135** (2001) 238–259, `arXiv:hep-ph/0010017`.

[31] **FOCUS** Collaboration, J. M. Link *et al.*, "Čerenkov Particle Identification in FOCUS," *Nucl. Instrum. Meth.* **A484** (2002) 270–286, `arXiv:hep-ex/0108011`.

[32] E. W. Vaandering, *Mass and Width Measurements of the Σ_c Baryons*. PhD thesis, University of Colorado, 2000. FERMILAB-THESIS-1999-27.

[33] R. Brun, O. Couet, C. E. Vandoni, and P. Zanarini, "PAW: A General Purpose Portable Software Tool for Data Analysis and Presentation," *Comput. Phys. Commun.* **57** (1989) 432–437.

[34] **CLEO** Collaboration, G. S. Huang *et al.*, "Absolute Branching Fraction Measurements of Exclusive D^+ Semileptonic Decays," *Phys. Rev. Lett.* **95** (2005) 181801, `arXiv:hep-ex/0506053`.

[35] F. James and M. Roos, "Minuit: A System for Function Minimization and Analysis of the Parameter Errors and Correlations," *Comput. Phys. Commun.* **10** (1975) 343–367.

[36] L. Agostino, *Pseudoscalar Semileptonic Decays of the D^0 Meson*. PhD thesis, University of Colorado, 2004. FERMILAB-THESIS-2004-59.

[37] **FOCUS** Collaboration, J. M. Link *et al.*, "New Measurement of the $\frac{\Gamma(D^+ \to \overline{K}^{*0}\mu^+\nu)}{\Gamma(D^+ \to K^-\pi^+\pi^+)}$ and $\frac{\Gamma(D_s^+ \to \phi\mu^+\nu)}{\Gamma(D_S^+ \to \phi\pi^+)}$ Branching Ratios," *Phys. Lett.* **B541** (2002) 243–250, `arXiv:hep-ex/0206056`.

[38] R. Gardner, J. E. Wiss, "Estimating Systematics Errors," 1994. FOCUS Internal Communication.

[39] **E–653** Collaboration, K. Kodama *et al.*, "Observation of $D^+ \to \rho(770)^0\mu^+\nu$," *Phys. Lett.* **B316** (1993) 455–461, `arXiv:hep-ph/9308344`.

[40] **E–687** Collaboration, P. L. Frabetti *et al.*, "Observation of the Vector Meson Cabibbo Suppressed Decay $D^+ \to \rho^0\mu^+\nu$," *Phys. Lett.* **B391** (1997) 235–242.

[41] **E–791** Collaboration, E. M. Aitala *et al.*, "Measurement of the Branching Ratio $\frac{\mathrm{B}(D^+ \to \rho^0 l^+\nu_l)}{\mathrm{B}(D^+ \to \overline{K}^{*0} l^+\nu_l)}$," *Phys. Lett.* **B397** (1997) 325–332, `arXiv:hep-ex/9611002`.

[42] **FOCUS** Collaboration, J. M. Link *et al.*, "New Measurement of the D^0 and D^+ Lifetimes," *Phys. Lett.* **B537** (2002) 192–200, `arXiv:hep-ex/0203037`.

[43] P. Ball, "The Semileptonic Decays $D \to \pi(\rho)e\nu$ and $B \to \pi(\rho)e\nu$ from QCD Sum Rules," *Phys. Rev.* **D48** (1993) 3190–3203, `arXiv:hep-ph/9305267`.

[44] K.-C. Yang and W. Y. P. Hwang, "The QCD Sum Rule Approach for the Semileptonic Decay of the D or B Meson into a Light Meson and Leptons," *Z. Phys.* **C73** (1997) 275–292.

[45] **APE** Collaboration, C. R. Allton *et al.*, "Lattice Calculation of D and B Meson Semileptonic Decays, Using the Clover Action at $\beta = 6.0$ on APE," *Phys. Lett.* **B345** (1995) 513–523, `arXiv:hep-lat/9411011`.

[46] W. Jaus, "Semileptonic, Radiative and Pionic decays of B, B* and D, D* Mesons," *Phys. Rev.* **D53** (1996) 1349–1365.

[47] D. Scora and N. Isgur, "Semileptonic Meson Decays in the Quark Model: An Update," *Phys. Rev.* **D52** (1995) 2783–2812, `arXiv:hep-ph/9503486`.

[48] P. J. O'Donnell and G. Turan, "Charm and Bottom Semileptonic Decays," *Phys. Rev.* **D56** (1997) 295–302, `arXiv:hep-ph/9604208`.

[49] D. Melikhov, "Exclusive Semileptonic Decays of Heavy Mesons in the Quark Model," *Phys. Lett.* **B394** (1997) 385–394, `arXiv:hep-ph/9611364`.

[50] Z. Ligeti, I. W. Stewart, and M. B. Wise, "Comment on V_{ub} from Exclusive Semileptonic B and D Decays," *Phys. Lett.* **B420** (1998) 359–366, `arXiv:hep-ph/9711248`.

[51] L. A. Kondratyuk and D. V. Tchekin, "Transition Form Factors and Probabilities of the Semileptonic Decays of B and D Mesons within Covariant Light-Front Dynamics," *Phys. Atom. Nucl.* **64** (2001) 727–752.

[52] Melikhov, D. and Stech, B., "Weak Form Factors for Heavy Meson Decays: An Update," *Phys. Rev.* **D62** (2000) 014006, `arXiv:hep-ph/0001113`.

[53] S. Fajfer and J. F. Kamenik, "Charm Meson Resonances and $D \to V$ Semileptonic Form Factors," *Phys. Rev.* **D72** (2005) 034029, `arXiv:hep-ph/0506051`.

[54] **FOCUS** Collaboration, J. M. Link *et al.*, "New Measurements of the $D^+ \to \overline{K}^{*0}\mu^+\nu$ Form Factor Ratios," *Phys. Lett.* **B544** (2002) 89–96, `arXiv:hep-ex/0207049`.

[55] **FOCUS** Collaboration, J. M. Link *et al.*, "New measurements of the $D_s^+ \to \phi\mu^+\nu$ Form Factor Ratios," *Phys. Lett.* **B586** (2004) 183–190, `arXiv:hep-ex/0401001`.

[56] **FOCUS** Collaboration, J. M. Link *et al.*, "Analysis of the Semileptonic Decay $D^0 \to \overline{K}^0\pi^-\mu^+\nu$," *Phys. Lett.* **B607** (2005) 67–77, `arXiv:hep-ex/0410067`.